NORTHWESTERN UNIVERSITY

Insights into Complex Reaction Processes Governing Hydrocarbon Conversion through Microkinetic Modeling

A DISSERTATION

SUBMITTED TO THE GRADUATE SCHOOL
IN PARTIAL FULFILLMENT OF THE REQUIREMENTS

for the degree

DOCTOR OF PHILOSOPHY

Field of Chemical Engineering

By

Grant Marsden

EVANSTON, ILLINOIS

June 2023

Abstract

Shale gas is a critical energy resource that is comprised primarily of light gases that are expensive to transport. Because these gases are geographically spread-out and there is insufficient capacity to transport them to centralized processing facilities, they must often be flared, leading to great sources of resource waste and direct pollution. To ensure efficient use of these valuable resources, there has been significant drive to develop new methods to fine-tune product selectivity for fuel production by advancing fundamental knowledge on zeolite catalysts and oligomerization mechanisms. This doctoral work has aimed to build and apply computational frameworks to capture complex effects within reaction processes for fuel conversion chemistry.

Despite the industrial importance of zeolite catalysts, there remains great uncertainty around key functional properties, such as the impact of the proximity of active sites within a zeolite. In this thesis, a framework was developed to capture this effect through microkinetic modeling, a unifying approach that combines knowledge from quantum mechanics at the atomic scale with process scale reactor equations. Using a model system of methanol dehydration in a zeolite catalyst known as chabazite, density functional theory calculations were utilized to evaluate the energies of chemical states along the reaction pathway in the presence of both isolated and paired active sites. These energies were then incorporated into a microkinetic model, the results of which were compared to experimental data, which enabled analysis of reaction flux, speciation, and the degree to which each elementary reaction step controlled the overall product formation rate. This led to the insight that paired active sites are able to enhance methanol dehydration by stabilizing a methanol trimer species that was also reactive.

Expanding this framework involved further increasing both topological and chemical complexity. To advance chemical complexity, the thermal oligomerization of ethylene was analyzed as a key reaction for the energy transition. This reaction has more than a century of study, yet lacked up to this point significant study using quantum chemical calculations, leading to a lack of mechanistic understanding. A

microkinetic model that incorporated density functional theory calculations, adjusted within bounds of uncertainty, was developed, unraveling the drivers of initiation for this reaction, how the primary initiation mode shifts with conversion, and revealing the origin of odd-numbered carbon species in the product distribution from the β-scission of radical species that were formed from intramolecular hydrogen shift reactions.

To expand the topological complexity of this modeling framework, methanol dehydration over orthorhombic MFI, a zeolite with 12 crystallographically unique T-sites, was studied. Along with proximity to other T-sites, the location of a T-site within the structure of a zeolite is a major factor for determining catalytic activity. The microkinetic model developed in Chapter 2 was expanded to account for systems of N distinct sites and was used to capture the effects of each independent T-site of MFI on methanol dehydration to dimethyl ether. Flux, surface speciation, and degree of rate control analyses were applied to this model to identify a new critical species, methanol tetramer, which differed from the results of methanol dehydration on chabazite. Altogether, this work creates a platform to predictively model the impact of industrially relevant catalytic properties on the process scale from atomic scale knowledge, enabling the rational design of next-generation catalytic materials.

Acknowledgement

Thank you to Professor Linda Broadbelt for your continued support and guidance. You have my utmost respect. Thank you to my committee members, Professor Rajamani Gounder, Professor Randall Q. Snurr, and Professor Justin Notestein, for your insight, advice, and review. Thank you to the National Science Foundation for financial support through Cooperative Agreement no. EEC-1647722, the Engineering Research Center for Innovative and Strategic Transformation of Alkane Resources. Additionally, thank you to all of the CISTAR staff that have helped me along the way. Thank you to my collaborators and co-authors, including but not limited to Pavlo Kostetskyy, Ryoh-Suke Sekiya, Alexander Hoffman, Songhyun Lee, Professor David Hibbitts, Matthew A. Conrad, Alexander Shaw, Professor Jeffrey T. Miller, Professor Sergio Vernuccio, Elizabeth Bickel, and Jerry Crum. Thank you to Broadbelt group members past and present as well as my Northwestern graduate cohort for all of your support.

List of Abbreviations

CHA: Chabazite
DME: Dimethyl Ether
MTO: Methanol-to-Olefins
DFT: Density Functional Theory
BA: Brønsted Acidic
SDA: Structure-directing Agents
6-MR: Six-membered Ring
MeOH: Methanol
T-site: Tetrahedral Site
DPE: Deprotonation Energy
VASP: Vienna Ab Initio Software Package
CCI: Computational Catalysis Interface
PAW: Projector Augmented Wave Method
PBE: Perdew, Burke and Ernzerhof
GGA: Generalized Gradient Approximation
SCF: Self-Consistent Field
IZA: International Zeolite Association
NNN: Next-nearest Neighbor
NNNN: Next-next-nearest Neighbor
ZPVE: Zero-point Vibrational Energy
PFR: Plug Flow Reactor
AIMD: Ab Initio Molecular Dynamics
DRC: Degree of Rate Control
MAS NMR: Magic Angle Spinning Nuclear Magnetic Resonance
FID: Flame Ionization Detector
GC: Gas Chromatograph
RF: Response Factors

This work is dedicated to Kimlynn, James, and Granger Marsden for their consistent and continued support.

Table of Contents

List of Figures

List of Tables

Chapter 1: Introduction

1.1 Overview

Since the early 2000s, shale gas production has surged within the United States to become one of the most important contributors to the domestic energy economy.[1-5] In 2022 alone, nearly 28 trillion cubic feet of shale gas was produced in the United States, up double from only eight years prior, and projected only to grow over the next 50 years.[6, 7] Proper utilization and development of these shale gas resources would have a number of benefits, including the reduction of the United States' dependence on importing foreign energy, high contribution to domestic GDP through diversifying energy exports, and a significant reduction in greenhouse gas emissions through the displacement of coal as a fuel source.[8-11] Continued benefits are reliant on proper development of shale gas resources, the key challenge of which is the high concentration of light hydrocarbons (LHCs) present in these resource streams.[12]

Only an average of 2% of natural gas is readily available as liquid components, with the remaining fraction being in the form of gaseous light compounds such as methane, ethane, and propane, as shown in Figure 1.1.[13] The gaseous nature of these compounds comes with an enormous increase in the cost of transporting and exporting natural gas, forcing their separation and oftentimes the necessity to flare them,[14-16] as the current infrastructure cannot handle the large quantities of LHCs being produced.[17, 18] Current methods of upgrading these compounds requires transporting them to a large, centralized processing facility. Geography poses a challenge, as shale resources are often in remote areas and are spread out across the country, requiring a massive network of pipelines that are not as of yet equipped to handle the excess of produced LHCs.[17]

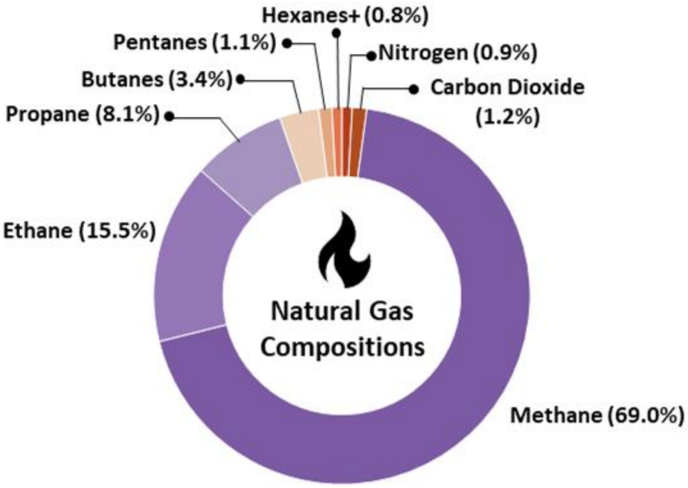

Figure 1.1: Average natural gas makeup, aggregated from five United States shale fields – Bakken, Marcellus, Utica, Niobrara, and Eagle Ford in mol %.[13]

Thus, the central idea contextualizing this dissertation is that the need for transporting LHC-rich gas streams to centralized processing facilities can be alleviated by the creation of local, mobile processing plants. Through conversion of light alkanes to liquid products and valuable polymer precursors directly at a wellhead, valorization of negative-cost feedstock is possible. Produced liquid fuels can then be easily stored, transported, and exported.[19] Creating such a system involves an inverse approach to typical chemical process development. Rather than scaling up processes to a plant scale, the development of highly intensified scaled-down processes is crucial. Activation of the LHCs through dehydrogenation and oligomerization of the activated LHCs to form higher molecular weight products are key steps. The need for deep understanding around this oligomerization is the driving force behind the research presented in this dissertation, as it is one of the fundamental keys that could unlock paired economic and environmental benefits from what is currently a major waste stream.

1.2. Outline of Research

Chapter 2 is a peer-reviewed article, reproduced from work published in ACS Materials Au. This chapter details the development of a microkinetic model capable of capturing the catalytic effects of proximal acid sites within a zeolite framework, using a well-studied reaction of the dehydration of methanol to dimethyl ether as a test reaction to develop the methodology. Electronic structure calculations and microkinetic modeling are paired with experimental data to probe the effects of acid site proximity in a zeolite known as chabazite on methanol dehydration rates. This framework was used to identify key contributors to the increase of methanol dehydration rate with increasing paired site concentration in chabazite; namely, next-nearest neighbor paired sites promote the formation of methanol trimer clusters with beneficial reaction pathways rather than inhibiting clusters of larger sizes.

Chapter 3 expands the microkinetic modeling methodology of the previous chapter beyond methanol dehydration to larger reaction networks, focusing on the thermal oligomerization of ethylene, a reaction with a long history but a previous lack of underlying mechanistic understanding. A density functional theory-parameterized microkinetic model is applied to investigate initiation and the formation of odd-numbered carbon products. Flux analysis is used to determine the primary driver of initiation as the hydrogen abstraction by a 1,4-butyl diradical, produced directly from the reaction of two ethylene molecules. Within the modeled truncated reaction network, odd-numbered carbon species are seen to arise from β-scission of C_8 radical species.

Chapter 4 returns to the simpler reaction network of methanol dehydration while applying the modeling framework to MFI, a more crystallographically complex zeolite framework than chabazite. Unlike chabazite, which contains only a single crystallographically unique tetrahedral site (T-site), the orthorhombic form of MFI has 12 unique T-sites. Microkinetic modeling is paired with density functional theory and experimental data to capture the effects of T-site location, using the same structure developed for evaluating proximal acid site effects. Analyses of flux, surface speciation, and degree of rate control identify methanol tetramers as key intermediates for methanol dehydration chemistry over MFI, and the techniques additionally identify T4, T6, T7, and T12 as critical T-sites that promote this chemistry.

Finally, Chapter 5 summarizes the research presented in this dissertation. Additionally, recommendations for future directions of the research are presented, including direct next steps to continue developing this robust framework capable of modeling both location and proximity effects of acid sites within zeolites, with an aim towards modeling oligomerization chemistry. These developments are key to converting one of the largest direct waste streams in the United States into a source of value, simultaneously providing environmental benefits by more efficiently using extracted fuel resources.

Chapter 2: Quantifying Effects of Active Site Proximity on Rates of Methanol Dehydration to Dimethyl Ether over CHA Zeolites through Microkinetic Modeling

Material in this chapter is reproduced from the following peer-reviewed article: Marsden, G.; Kostetskyy, P.; Sekiya, R.S.; Hoffman, A.; Lee, S.; Gounder, R.; Hibbitts, D.; Broadbelt, L.J. Quantifying Effects of Active Site Proximity on Rates of Methanol Dehydration to Dimethyl Ether over CHA Zeolites through Microkinetic Modeling. *ACS Materials Au* **2022**, *2* (2), 163-175.[20]

2.1. Abstract

Porous solid acid materials such as zeolites have been widely used as catalysts and sorbents for numerous industrial processes such as petrochemical conversion, biomass upgrading, gas separations, and aqueous toxin sorption. Recent advances in synthetic methods have allowed for control of active site distribution at the nanoscale, resulting in highly tunable materials with unique physicochemical and catalytic properties. Control of the spatial proximity of Brønsted acid sites within the zeolite framework can result in materials with properties that are distinct from materials synthesized through conventional crystallization methods or available from commercial sources. Recent experimental evidence has shown that turnover rates (per acid site) of different acid-catalyzed reactions increase with the fraction of proximal acid sites in chabazite (CHA) zeolites. The catalytic conversion of oxygenates for production of biomass-based fuels and chemicals is an important area of research that has attracted significant attention, and the dehydration of methanol to dimethyl ether (DME) is a well-studied chemical reaction as part of the methanol-to-olefins (MTO) chemistry that can be catalyzed by solid acids. Previously published experimental data have shown that DME formation rates (per acid site) increase systematically with the fraction of proximal acid sites in the six-membered ring of CHA. In this chapter, the effect of acid site proximity in CHA on methanol dehydration rates is probed using electronic structure calculations and microkinetic modeling to identify the primary causes of this chemistry and their relationship to the local structure of the catalyst at the nanoscale. A density functional theory (DFT)-parametrized microkinetic model of methanol dehydration to DME, catalyzed by acidic CHA zeolite, was developed with direct comparison to experimental data. Effects of proximal acid sites on reaction rates were captured quantitatively for a range of operating conditions and catalyst compositions, with a particular focus on total paired acid site concentration and reactant clustering to form higher nuclearity complexes at the active site. Next-nearest neighbor paired acid sites were identified as promoting the formation of methanol trimer clusters rather than inhibiting tetramer or pentamer clusters, resulting in large increases in rate for dimethyl ether production due to the lower energy barriers present in the concerted methanol trimer reaction pathway.

The model framework developed in this study can be extended to other zeolite materials and reaction chemistries toward the goal of rational design and development of next-generation catalytic materials and chemical processes.

2.2. Introduction

Zeolites are a class of crystalline aluminosilicates with ordered micropore structures that remain stable over a range of experimental conditions and behave as catalysts for a variety of chemistries[21, 22]. Since the inception of the field, significant effort has been dedicated toward tailoring the zeolite structure, pore topology, composition and active site identity to optimize their catalytic performance[23]. Brønsted acidic (BA) zeolites are important catalysts for a range of industrial applications, frequently used for dehydration, condensation, oligomerization, catalytic cracking, and hydrocracking[24, 25].

Recent developments in experimental synthesis methods have allowed for control of framework Al^{3+} distribution and arrangement through the use of structure-directing agents (SDAs) during hydrothermal crystallization[26-34]. Gounder and co-workers[30, 31, 35] have reported synthetic methods to systematically control the distribution of isolated and paired framework aluminum atoms in the six-membered rings (6-MR) of SSZ-13 (CHA framework) through the use of organic and inorganic SDAs of varying charge density. Other routes to influence Al distribution in CHA have also been reported, such as using non-conventional inorganic cations like strontium and altering crystallization times and conditions[36, 37]. These synthetic advances allow controlling of the concentration and distribution of BA sites within the pore systems of zeolites, with the unique ability to tune the spatial proximity of BA sites at the nanoscale. Although framework Al-O-Al arrangements are prohibited according to Löwenstein's rule[38], Al substitution in second-nearest-neighbor positions and at greater relative distances can occur. This control of acid site proximity can enable tuning the catalytic activity in known chemistries[30, 31, 39-42] or enabling hitherto inaccessible chemical pathways by alternate mechanisms, in which two acid sites are involved in the adsorption, activation, and stabilization of reactants, intermediates, and transition states. Recent work on methanol (MeOH) dehydration to dimethyl ether (DME) over the CHA framework has shown that the potential energy landscapes of two competing mechanisms at one BA site can be altered to a significant degree in the presence of a proximate BA site, leading to increases in turnover rates (per H^+)[31, 42-44].

The CHA framework is characterized by a single crystallographically unique lattice tetrahedral-site (T-site) and a three-dimensional small-pore structure that imposes spatial constraints limiting the diameter of a sphere that can diffuse along its channels to 3.7 Å[45]. While the location of acid sites within zeolite frameworks remains an impactful focus of research[34, 46], the single unique T-site of CHA allows for the decoupling of the effects of location and proximity, enabling a study focused on acid site proximity and paired site configurations. Density functional theory (DFT) has been used to show that paired site configurations are stronger acids than isolated sites in CHA as calculated by deprotonation energy (DPE), the energy to remove a proton from a BA site to a non-interacting distance[42, 47]. The increase in acid strength is caused by the stabilization of conjugate base anions (formed upon deprotonation) by H-bonding with the other BA site when BA site pairs share a 6-MR within CHA[42, 47].

Dehydration of MeOH to DME is an industrially relevant chemical reaction that has been postulated as one of the reaction events in methanol-to-olefin (MTO) chemistry and is useful in fundamental studies as a catalytic probe of acid strength and confinement effects in solid acid catalysts[48, 49]. Importantly, at high reactant partial pressures, complexes of multiple alcohol molecules can form at the BA site and affect the corresponding reaction energetics by affecting the relative stabilities of intermediate and transition states along the reaction coordinate[40, 50]. In addition, turnover rates of DME formation (per H^+) can be increased upon the formation of paired BA site motifs in the zeolite pore structure[31]. The presence of paired acid sites results in energetically favorable configurations that decrease the activation Gibbs free energy barriers of rate-determining steps relative to the unpaired analogues[42].

In this chapter, a combination of experimental kinetic data, electronic structure calculations, and microkinetic modeling toward elucidating the chemistry of methanol dehydration over CHA zeolite catalysts that contain varying concentrations of paired BA sites is reported. The effect of the presence of paired site motifs on reaction rates was quantified using DFT and shown to agree with experiments for a range of partial pressures and fractions of paired BA sites. Rigorous analysis was performed to evaluate sensitivity to the different model parameters for a range of conditions. The findings reported in this work and the modeling framework developed can be used as a basis for analysis of different catalyst formulations, operating conditions, and even different chemistries, demonstrating the effectiveness of multi-scale modeling.

2.3. Computational Methods

2.3.1. Density Functional Theory

Fully-periodic density functional theory (DFT) calculations were performed with the Vienna ab initio software package (VASP)[51, 52] implemented in the computational catalysis interface (CCI)[53]. Planewave functions were constructed with the projector augmented wave method (PAW) and energy cutoff of 400 eV[54, 55]. The Brillouin zone was sampled at the Γ-point for all calculations. The Perdew, Burke and Ernzerhof (PBE) form of the generalized gradient approximation (GGA) functional was used for all calculations[54, 55]. Dispersion interactions were quantified by including the DFT-D3 empirical correction with Becke and Johnson damping (D3BJ)[56, 57]. Geometries were optimized in two steps with the goal of maximizing chemical accuracy with good computational efficiency. Structures were optimized in the first step with a conjugate-gradient algorithm (IBRION = 2) using a wavefunction convergence criteria keeping energy variations between self-consistent field (SCF) iterations $< 10^{-4}$ eV, and forces were computed with a fast Fourier transform grid of 1.5-times the default energy cutoff (PREC = ACCURATE in VASP). Structures were relaxed until the maximum force on any atom was < 0.05 eV/Å. The same structures were reoptimized with the same conjugate gradient algorithm with wavefunctions converged to $< 10^{-6}$ eV and maximum force on any atom to < 0.05 eV/Å and an FFT grid twice the planewave cutoff.

Gas-phase species were modeled in an $18\times18\times18$ Å^3 cubic unit cell. The CHA structure was obtained from the database of the International Zeolite Association (IZA)[45] with unit cell parameters of $a = b = 13.625$ Å, $c = 14.767$ Å, $\alpha = \beta = 90.0°$, and $\gamma = 120.0°$. Some zeolite models from the IZA restructure absent simulated annealing or unit cell optimization, but this CHA model is stable without such additional treatments[58]. One to two Al were substituted in the CHA unit cell (Si/Al = 17–35); two Al pairs were placed at positions next-nearest neighbor (NNN) and next-next-nearest neighbor (NNNN) positions in the 6-MR of CHA, similar to prior work (Figure 2.1)[42]. 29Si NMR spectra of the experimental CHA samples used in this study, reported in prior work[30], indicated that the numbers of two Al sites in NNN configurations were negligible. Adsorbates were evaluated while interacting with all four O-atoms around each Al to find the preferred configuration of guest species within the framework for a given Al arrangement. The orientation of CH_3 moieties on methanol molecules within clusters were systematically rotated in 30° increments around the O–H axis of the O to which they were bound (*i.e.*, the C–O–H-Al torsional angle, where the Al is an arbitrary reference) and nonsensical structures—where atoms were too close to the zeolite framework or other methanol molecules—were discarded. These reorientations preserve strong interactions between nearby methanol molecules and generate new structures that were subsequently optimized again using the same VASP settings as above. Similar reorientation schemes were shown to reduce calculated energies by up to 60 kJ mol^{-1} for adsorbates in zeolites[42, 59]. Similar sampling of the potential energy surface can be done using *ab initio* molecular dynamics simulations (AIMD) and metadynamics, from which the dynamic behavior of clusters can be determined and from which a subset of configurations can be optimized to test new structures. Similar approaches have been used previously to study alcohol and water clusters in zeolites[25, 60-64]; however, such extensive methods are computationally costly and do not necessarily perform better than simple optimization calculations when parameterizing microkinetic models.

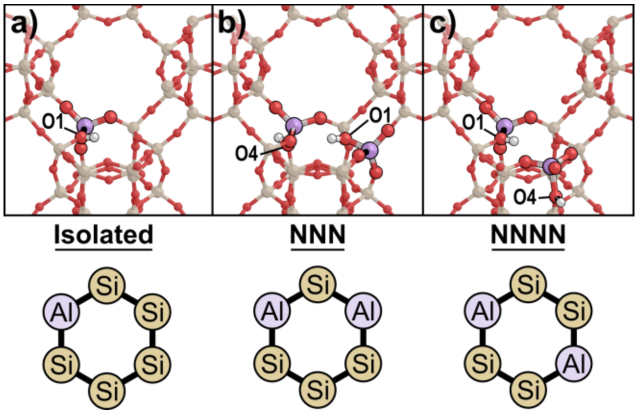

Figure 2.1: The different Al arrangements considered in DFT calculations in this work: (a) isolated sites, (b) next-nearest neighbor (NNN) configurations, and (c) next-next-nearest neighbor (NNNN) configurations. Top images in each panel show the most stable proton-form for the given Al arrangement.

Vibrational frequencies were used to determine zero-point vibrational energies (ZPVEs) and vibrational, rotational, and translational enthalpies (*H*) and free energies (*G*). Frequencies were computed using a fixed displacement method (n = 2) for all gas-phase and adsorbed species. Only guest species, protons, and AlO_4 tetrahedra were permitted to vibrate for frequency calculations in the zeolite while the remainder of the Si and O atoms were frozen in place (a partial Hessian approach). Frequencies were used to calculate *H*

$$H = E_0 + ZPVE + H_{vib} + H_{trans} + H_{rot} \tag{2.1}$$

and *G*

$$G = E_0 + ZPVE + G_{vib} + G_{trans} + G_{rot} \tag{2.2}$$

at 415 K and 1 bar CH_3OH from statistics mechanics formalisms (see Section A.3. in Appendix for details)[65]. All motions from frequencies in zeolites were modeled as vibrations, including frustrated translation and rotation (*i.e.*, their translational and rotational free energies and enthalpies were zero). Because low-frequency modes contribute disproportionately to entropy (*S*) estimations, calculated frequencies < 60 cm^{-1} were replaced with 60 cm^{-1}, similar to prior work[40, 42, 66, 67].

2.3.2. Microkinetic Modeling

To set up the microkinetic model, a set of ordinary differential equations describing the change in concentration of each gas and surface species was formulated. First, the rate of each of the 36 elementary steps on isolated sites was defined as:

$$r_{i,isolated} = A_i \exp\left(\frac{-E_{a,i}}{RT}\right) \prod_{j}^{reactants} C_j \tag{2.3}$$

Where r_i is the rate of the i^{th} elementary step, A_i is the pre-exponential factor, $E_{a,I}$ is the activation energy, and C_j is the partial pressure of a reactant gas species or the fractional coverage of a reactant surface species. Paired active sites within the model were treated as a separate class of site on which an alternative set of kinetic and thermodynamic parameters could be accommodated based on the catalysts studied experimentally (see below). The rate of each of the 36 elementary steps on paired acid sites included an additional factor to enable using the number of isolated active sites as the integration variable, with the pathways on paired sites contributing according to their fraction of the total number of active sites:

$$r_{i,paired} = \frac{\frac{n_{paired}}{n_{total}}}{1 - \frac{n_{paired}}{n_{total}}} A_i \exp\left(\frac{-E_{a,i}}{RT}\right) \prod_{j}^{reactants} C_j \tag{2.4}$$

Where n_{paired} is the number of paired acid sites, n_{total} is the number of total acid sites, and the ratio of n_{paired}/n_{total} is known. From these rates, 33 ordinary differential equations covering the different gas and surface species were constructed of the form:

$$\frac{dC_i}{dn_{isolated}} = \sum_j \nu_{i,j} r_j \tag{2.5}$$

Where $\nu_{i,j}$ is the stoichiometric number of species i in elementary step j, and $n_{isolated}$ is the number of isolated active sites in the system. Here, the integration variable is the number of isolated active sites in the system, determined as:

$$n_{isolated} = n_{total}\left(1 - \frac{n_{paired}}{n_{total}}\right) \tag{2.6}$$

This set of ordinary differential equations was paired with two algebraic equations for surface species balances and combined with the design equation of a plug flow reactor (PFR) to reflect the experimental conditions. The total rate of DME formation was calculated at the outlet, where differential conversion ($<$ 2%) was confirmed. The experimental reactor[31] was loaded with 0.005 to 0.025 g of catalyst with a silicon to aluminum ratio of 14-16, leading to a range of possible number of active sites from $3.8 \cdot 10^{18}$ to $2.3 \cdot 10^{19}$. Thus, simulations were run with a total of 10^{19} active sites. Additionally, to match with experimental gaseous flow rates, the total molar flow rate of the inlet was set to 0.615 mol/s. Simulations were performed at a temperature of 415 K to match with the average experimental temperature. The methanol pressure was varied over a range from 35 Pa to 52,092 Pa at specific values dictated by the experimental studies[31].

Surface coverage of isolated and paired sites was evaluated at the outlet of the reactor, determined by the proper isolated site basis. Net rates of individual reaction pathways were determined by evaluating the net rate of each final independent reaction of each branch of the mechanism before feeding into final DME desorption. For example, the net contribution of the trimer pathway to DME production was considered to be the net rate of the *iso,meoh,des,trim* step. To account for uncertainty inherent within the DFT calculations due to the level of theory used in calculations of entropy and electronic structure, DFT activation energies for sensitive parameters were tuned within the bounds of ± 6 kJ/mol. In the case where a reaction was assumed to be unactivated, the pre-exponential factor was instead tuned within the bounds of one order of magnitude. The impact of each parameter on overall DME formation rate for each paired percentage was determined through lowering and raising activation energies or pre-exponential factors within the previously mentioned bounds. The most impactful parameters were marked to be tuned, being selective to avoid introducing issues surrounding degrees of freedom. For the case of completely isolated sites, the marked isolated parameters were optimized through nonlinear least squares regression within the discussed bounds using the experimental data as objective points. Once a set of tuned isolated parameters was collected, these parameters were then locked, and the cases of different percentages of paired sites were analyzed equivalently. The regression package used was unable to analyze the multiple cases simultaneously, so three independent runs were performed for the three paired site percentage cases; the weighted average of these runs was taken to evaluate a single and consistent final set of parameters.

2.4. Results and Discussion

2.4.1. Reaction Mechanism

Reaction mechanisms for Brønsted acid-catalyzed methanol dehydration to DME have been proposed by Iglesia and coworkers[48, 68]. The authors proposed two competing pathways after an initial step of the adsorption of one methanol species on a BA site. Formation of dimethyl ether can proceed through a sequential (or dissociative) pathway, in which a surface methoxy group is formed through rearrangement and dehydration of the methanol monomer. This dehydration is followed by the adsorption of another methanol molecule near a surface methoxy species, which react to form dimethyl ether (DME) that desorbs into the fluid phase. Alternatively, the bound surface methanol species can follow a concerted (or associative) pathway initiated by the coordination of additional methanol molecules, forming an adsorbed dimer, that can rearrange and dehydrate. Recent work[40, 69] has shown that these concerted bimolecular transition states can also form from larger methanol clusters, including trimers and tetramers, which can readily form at methanol pressures (10 kPa) relevant to experimental studies. While larger clusters were examined (up to 12 methanol molecules), the differential adsorption free energies calculated in that prior work suggest that larger complexes are less favorable. Thus, in this work, pentamers are assumed to be non-reactive in the scheme adopted here, functioning as an inhibiting state. Methanol clusters of 2-4 methanol molecules can rearrange and dehydrate, via an S_N2-like transition state, to form bound dimethyl ether with spectator water and methanol molecules, which ultimately uncoordinate to form a final bound dimethyl ether species that can then unbind to form gas-phase dimethyl ether, thus completing the catalytic cycle. All reactions were assumed reversible and assumed to be accessible to both isolated and paired active sites. As shown in previous studies[42], the presence of spectator methanol species resulted in increased energy barriers for the (rate-determining) elementary steps in the sequential pathway, with reported free energy barriers of 134 kJ/mol, 155 kJ/mol and 143 kJ/mol in the presence of one, two, and three spectator species, respectively. Contrary to the concerted pathway, the sequential reaction barriers in the presence of spectator species were significantly less accessible, not exhibiting the promoting behavior observed in concerted reactions. Therefore, the additional elementary steps corresponding to sequential reactions in the presence of spectator methanol molecules were excluded from the reaction network in the interest of decreasing model stiffness.

Based on the mechanism described in Schemes 2.1 and 2.2 as well as the DFT results, a microkinetic model was developed to calculate DME formation rates at experimental conditions for a range of site combinations. Paired sites are modeled here with an independent set of rate constants from isolated sites, but through an identical network of chemical reactions. Thus, paired sites are not treated using a two-site kinetic model, but the effects of pairing are captured by differences between $\underline{k}_{\mathrm{iso}}$ and k_{pair} rate constants. In microkinetic modeling, no assumptions about the rate-determining step(s) are made, and instead the rates of a complete set of plausible elementary steps are formulated according to mass action kinetics. The results of the model solution are then analyzed to identify major pathways that carry the flux, surface species coverage, and product distribution. As implemented here, the results of the microkinetic model were queried to probe the prevalence of the concerted and sequential pathways for a wide range of operating conditions at each site type, and within the possible routes comprising the concerted pathway which methanol cluster size gave the highest contribution to the overall rate. In addition, the relative rates of individual steps on isolated and paired sites could be directly quantified.

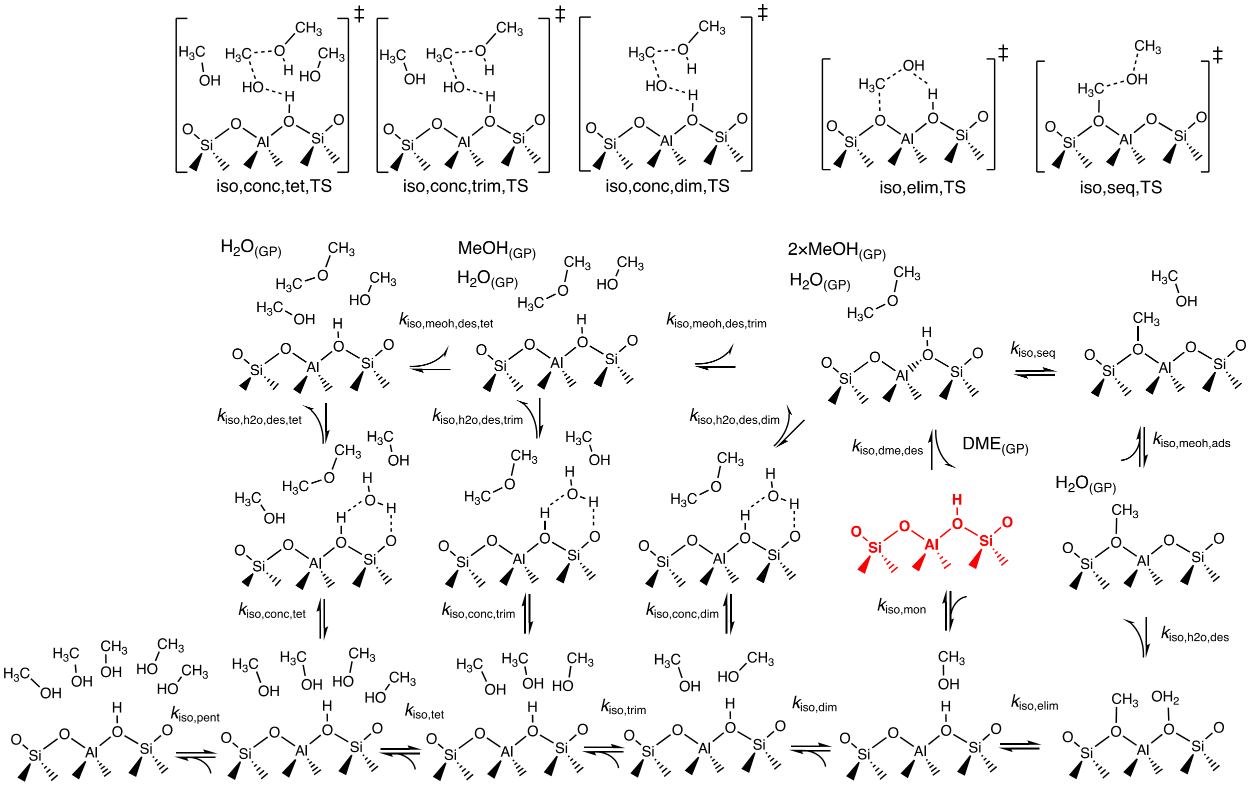

Scheme 2.1: Mechanism for methanol dehydration as shown on isolated sites. Beginning with methanol adsorption ($k_{iso,mon}$), the reaction can advance through elimination to form a methoxy species ($k_{iso,elim}$) or through the adsorption of additional methanol species to form methanol dimers, trimers, tetramers, and inhibiting pentamers ($k_{iso,dim}$, $k_{iso,trim}$, $k_{iso,tet}$ and $k_{iso,pent}$, respectively) toward the concerted pathway ($k_{iso,conc}$). The reaction sequence is initiated by reactant adsorption on unoccupied Brønsted acid site, depicted in red. Individual rate constants are specified for each elementary step and adsorption/desorption events are identified with curved reaction arrows. Gas-phase species formed upon desorption are denoted with (GP). Graphical representations of relevant transition states for the concerted and sequential pathways are shown as figure insets.

Scheme 2.2: Elementary steps of modeled methanol dehydration pathways. An asterisk (*) indicates a surface site, whereas a dagger (†) represents a species bound to the oxygen framework of the zeolite.

Elementary Step	**Rate constant**
MeOH + * ↔ MeOH*	k_{mon}
MeOH* + MeOH ↔ 2MeOH*	k_{dim}
2MeOH* ↔ DME-H_2O*	$k_{conc,dim}$
DME-H_2O* ↔ DME* + H_2O	$k_{h2o,des,dim}$
DME* ↔ DME + *	$k_{dme,dim}$
2MeOH* + MeOH ↔ 3MeOH*	k_{trim}
3MeOH* ↔ MeOH-DME-H_2O*	$k_{conc,trim}$
MeOH-DME-H_2O* ↔ MeOH-DME* + H_2O	$k_{h2o,des,trim}$
MeOH-DME* ↔ DME* + MeOH	$k_{meoh,des,trim}$
3MeOH* + MeOH ↔ 4MeOH*	k_{tet}
4MeOH* ↔ 2MeOH-DME-H_2O*	$k_{conc,tet}$
2MeOH-DME-H_2O* ↔ 2MeOH-DME* + H_2O	$k_{h2o,des,tet}$
2MeOH-DME* ↔ MeOH-DME* + MeOH	$k_{meoh,des,tet}$
4MeOH* + MeOH ↔ 5MeOH*	k_{pent}

$MeOH^* \leftrightarrow H_2O\text{-}CH_3^\dagger$ *(Rearranging H from zeolite site)*	k_{elim}
$H_2O\text{-}CH_3^\dagger \leftrightarrow CH_3^\dagger + H_2O$	$k_{h2o,des}$
$CH_3^\dagger + MeOH \leftrightarrow MeOH\text{-}CH_3^\dagger$	$k_{meoh,ads}$
$MeOH\text{-}CH_3^\dagger \leftrightarrow DME^*$ *(Reforming the H from zeolite site)*	k_{seq}

2.4.2. Density Functional Theory Calculations

Polar molecules can form clusters around Brønsted acid sites or polar defects within zeolite frameworks[50, 63, 70, 71]. During MeOH dehydration, protonated clusters of methanol form around AlO_4^- at high pressures, which inhibit MeOH dehydration at high pressures because some methanol must desorb prior to reactions occurring[40]; the same inhibitory regime occurs when the proximity of Al in the framework is systematically altered[31]. Samples with higher fractions of paired Al also have higher rate constants for MeOH dehydration to DME (first-order, zero-order, and inhibitory) at 415 K from 0.5–60 kPa. The presence of inhibition and the higher rate constants on paired sites at all evaluated pressures indicate that clusters still form on paired sites and the benefit conferred by pairing persists in the presence of these clusters; however, the structure of larger clusters (>2 ML, defined as MeOH per H^+) remains unexplored. Here, first the clustering of methanol molecules on NNN and NNNN Al pairs in the 6-MR of CHA was explored.

In a prior study of methanol clustering at isolated BA sites in CHA, it was found that methanol clusters preferred to form protonated chains which interacted with the conjugate base of the deprotonated BA sites at both the ends of the chain. Based on results here on isolated BA sites, the focus is on methanol coverages of ≤ 6 ML. Because two sites are now present within the 6-MR, more complex structures can be formed and were examined in this work. For example, clusters can be present as a single branched chain (with a +2 charge) or can form two cationic chains that potentially have different lengths; these branched or independent chains can also interact with one or both conjugate bases of the BA sites simultaneously. These structural motifs were captured in this work, leading to structural optimizations of 145-1315 methanol chain arrangements (Table A8, Appendix) for each coverage and Al arrangement. While *ab initio* molecular dynamics (AIMD) simulations may permit for a large sampling of the potential energy surface and shed light on the dynamics of these clusters, such a large number of configurational tests should identify preferred configurations at lower computational cost. The focus here was on the most stable identified structures as these are expected to be dominant at the low temperatures relevant to methanol dehydration.

Prior work[42] examining methanol dehydration on site pairs in CHA examined methanol coverages ≤ 2 MeOH / H^+; thus, the discussion here focused on larger clusters in this work. Generally, calculated energies indicate that two separate protonated clusters are preferred on NNN and NNNN pairs rather than one large cluster solvating the protons from both sites (Section A.4. in the Appendix). One methanol chain sits above the shared 6-MR and forms H-bonds to the conjugate bases of both BA sites in the most stable configuration at most coverages $\geq$1 ML and in all coverages from 1-4.5 ML. The ability for cations to interact simultaneously with two anionic conjugate base structures was also observed for transition state structures and causes higher MeOH dehydration rate constants for paired Al in CHA[31, 42]. The continued preference for these similar interactions between sites above the 6-MR suggests that they are also the source of higher rate constants in the inhibitory regime of MeOH dehydration on CHA. The chain above the shared 6-MR is comprised of 2 MeOH molecules for most structures at coverages from 2-4 ML on both NNN and NNNN site-pairs; the remaining 2-6 MeOH are then present as a second chain. This indicates that the two cationic chains interacting with the BA site pair are likely to be different sizes. For larger MeOH coverages, more than two chains can form. For example, the most stable configuration on the NNNN pair at 4 ML forms two distinct MeOH dimers above the 6-MR and a 6-MeOH chain in a nearby cage, the latter of which contains a cyclic network of H-bonded MeOH molecules similar to those observed in earlier studies of isolated BA sites (Figure 2.2b) Similar rings of methanol molecules within clusters form favorably at higher coverages on the NNNN site (Figure 2.2c-f), indicating that internal H-bonded rings are likely forming in the inhibitory regime of MeOH dehydration. These independent chains may alter the dynamics of MeOH desorption from chains to form transition states with the preferred molecularity; these desorptions cause inhibition in the kinetic data which persist on paired sites.

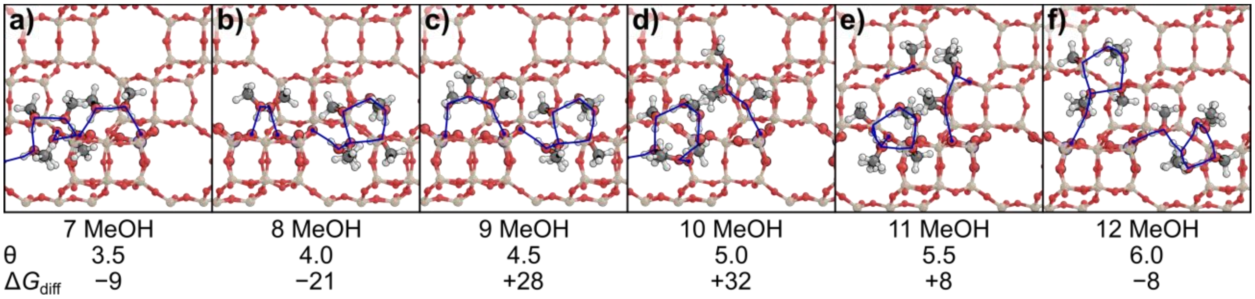

Figure 2.2: The structures for the most favorable configuration found for clusters of 7-12 MeOH on the NNNN pair. MeOH coverages per H^+ (θ) and differential binding free energies (ΔG_{diff}) in kJ mol^{-1} at 415 K are shown beneath each associated structure. Blue lines represent H-bonding networks that adsorbed MeOH form.

Average methanol binding energies remain similar between isolated and paired sites for coverages up to 6 ML (Figure 2.3). Here, the behavior of a "non-interacting pair" is approximated, which is intended to simulate the behavior of two isolated sites to compare to paired sites more directly. The energy of the non-interacting pair is calculated from the sum of energies from a pair of isolated sites at given MeOH coverages ($E_{iso,i}$) with the energy of a Si-form (E_{Si}) subtracted from that total to yield comparable energies to the single unit cell calculations with paired site configurations:

$$E_{nonint,i+j} = E_{iso,i} + E_{iso,j} - E_{Si} \tag{2.7}$$

where i and j are the number of methanol molecules around the two sites, with a corresponding total coverage of $\frac{i+j}{2}$. E_{nonint} values for a given coverage were calculated with all possible combinations of i and j, and binding energies are calculated from the lowest energy at a given coverage. Notably, the number of Si, Al, and O atoms accounted for in E_{nonint} are equivalent to those calculated directly on paired site models (*i.e.*, the energies can be directly compared), with 34 framework Si, 2 Al, and 72 O atoms. The preferred combinations at a given coverage were almost always comprised of two isolated sites with the same number of MeOH (e.g., for θ = 3 MeOH per H^+, $i = j = 3$). The only exception to this trend was when θ = 6, where the lowest non-interacting energy occurred when one site had 5 MeOH and the other had 7 MeOH. Because these energies are typically derived from two isolated sites with identical MeOH coverages, the average non-interacting binging energies overlap perfectly with binding energies at isolated sites (Figure 2.3). Binding energies on paired sites are stronger (more negative) at 0.5 ML, indicating that a methanol monomer binds more strongly to a BA site when a second BA site with a bare proton is nearby. This occurs because a H-bond forms between the two BA sites upon adsorption of MeOH (a weak base), as previously discussed[42]. Binding 1 MeOH per H^+ (at 1 ML), results in a weaker average binding free energy for both NNN and NNNN pairs compared to the non-interacting pair because that H-bond between the two BA sites is broken. As dimers and larger chains form, the average binding free energies of the MeOH interacting with NNN and NNNN pairs are similar to those for isolated sites up to 4 ML, above which they are significantly weaker (less negative) indicating that there are steric limits which impact the formation of larger clusters for Al pairs.

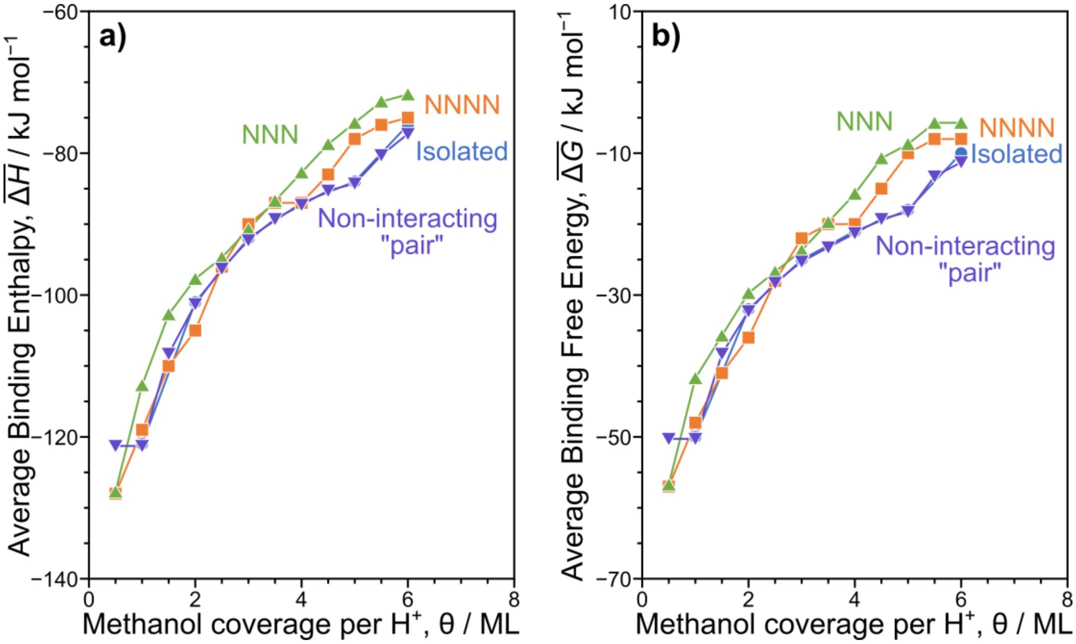

Figure 2.3: Average (a) binding enthalpies and (b) binding free energies for methanol coverages (θ) of 0.5–6 per H^+ on isolated sites (blue, ●), NNN site-pairs (green, ▲), NNNN site-pairs (orange, ■), and a non-interacting "pair" of isolated sites (purple, ▼).

2.4.3. Microkinetic Modeling

The continued presence of H-bonding interactions between paired sites with larger clusters present and the larger rate constants on paired sites compared to isolated sites in the inhibitory regime of MeOH dehydration above 20 kPa indicate that reductions in barriers from isolated to paired sites should be similar regardless of MeOH coverage, including with larger clusters present. As such, the microkinetic model in this work was parameterized by using as input the potential energy landscapes of the sequential and concerted pathways over the isolated and paired acid sites. Reaction rate coefficients were formulated in Arrhenius form (Equation 2.8), with a pre-exponential factor (A) and activation energy (E_a) specified for each reaction. The calculated enthalpies and free energies (and corresponding entropies) of reactant, intermediate, and product states along the reaction coordinate of concerted and sequential pathways were used to estimate the kinetic parameters and pre-exponential factors for each elementary step, ensuring thermodynamic consistency. The effect of methanol clustering over both paired and isolated active sites was accounted for explicitly, up to 5 methanol molecules per active site. Di Iorio et al.[40] have examined the two competing pathways through a combination of experiments and electronic structure calculations, with a focus on the presence of spectator species, expected to be a part of higher-order clusters around acid sites at larger partial pressures of methanol.

$$k(T) = Ae^{\left(\frac{-E_a}{RT}\right)} \tag{2.8}$$

In this work, the analysis of DME formation in the presence of spectator species was extended to involve the paired acid site configurations as distinct catalytic sites. Generally, the ground states of reactants were found to be less stable on paired sites when compared to analogous structures over isolated active sites, especially with increasing methanol cluster size. The values of these differences in ground state stabilities were on the order of 5–- 15 kJ/mol. In addition, the relative energies of the product states were found to be more stable relative to their analogues over isolated sites (22–- 28 kJ/mol). This could be rationalized by favorable hydrogen bond networks formed in the presence of paired acid sites, relative to the case of isolated-only sites. The effect of methanol clustering on paired acid site configurations can be exemplified in terms of activation free energies of the concerted pathway, with the values of 127.0 kJ/mol, 110.0 kJ/mol and 131.5 kJ/mol corresponding to transition states with zero, one and two spectator methanol molecules, respectively. For comparison, when examining the most stable isolated active site structure from conformational analysis, the activation free energies with zero, one and two spectator species were calculated to be 137.0 kJ/mol, 120.5 kJ/mol and 146.0 kJ/mol, respectively. Desorption events were assumed to be activated, with the enthalpy of desorption used as the activation energy. The complete set of adsorption enthalpies, activation free energies and associated first-order rate constants for the concerted and sequential pathways, as summarized in Scheme 2.1, is reported in Table A1 of the Appendix.

The experimental methanol dehydration rate values reported previously by Di Iorio et al.[31] on H-CHA zeolites were scaled down by a factor of 3.6-times to account for updated product response factors in the gas chromatograph flame ionization detector in the experimental setup used (additional details in Section A.2. in the Appendix). The parameters derived from DFT (reported in Table A1 of the Appendix) were used to simulate initial DME formation rate as a function of pressure (0.04-52.09 kPa CH_3OH) for CHA samples ranging from entirely isolated sites to 44% paired acid sites. The experimental Co^{2+} titration method is unable to distinguish between NNN and NNNN sites in the 6-MR of CHA, so two initial simulations were run assuming either all NNN or all NNNN sites (Figure A2 and Figure A3 in the Appendix). With the parameterization of the DFT data, NNNN sites were shown to have negligible impact on DME formation, even when tuning parameters within typical DFT uncertainty (Figure A4 in the Appendix). A mixture of 7.4% NNN to 92.6% NNNN sites was then assumed to match the results for relative Al-Al site probabilities for the 6-MR in CHA from simulations performed by Di Iorio et al.[35], and NNNN sites were assumed to have negligible flux with respect to DME formation. As described in Section 2.3.2., parameters to which the model was most sensitive were adjusted, and the final set of those parameters that were varied is shown in Table 2.1.

Table 2.1: List of DFT-calculated parameters that were tuned during parameter optimization. E_a values were tuned for relevant elementary steps where possible, and for adsorption events that are unactivated in the model, A values were tuned within one order of magnitude. Rate coefficient values are reported at 415 K.

Parameter	A ($\text{s}^{-1} \mid \text{Pa s}^{-1}$)	E_a (kJ/mol)	Original k(T)	Tuned Parameter	Tuned k(T)
$k_{iso,elim}$	$8.64 \cdot 10^{12}$ s^{-1}	129.5	$4.33 \cdot 10^{-4}$ s^{-1}	E_a, 123.5 kJ/mol	$2.46 \cdot 10^{-3}$ s^{-1}
$k_{pair,elim}$	$8.64 \cdot 10^{12}$ s^{-1}	128.8	$5.30 \cdot 10^{-4}$ s^{-1}	E_a, 122.8 kJ/mol	$3.02 \cdot 10^{-3}$ s^{-1}
$k_{pair,conc,dim}$	$8.64 \cdot 10^{12}$ s^{-1}	127.0	$8.93 \cdot 10^{-4}$ s^{-1}	E_a, 121.0 kJ/mol	$5.08 \cdot 10^{-3}$ s^{-1}
$k_{iso,trim}$	$1.37 \cdot 10^{3}$ Pa s^{-1}	0	$1.37 \cdot 10^{3}$ Pa s^{-1}	A, $1.37 \cdot 10^{4}$ Pa s^{-1}	$1.37 \cdot 10^{4}$ Pa s^{-1}
$k_{pair,trim}$	$1.66 \cdot 10^{3}$ Pa s^{-1}	0	$1.66 \cdot 10^{3}$ Pa s^{-1}	A, $1.66 \cdot 10^{4}$ Pa s^{-1}	$1.66 \cdot 10^{4}$ Pa s^{-1}
$k_{iso,conc,trim}$	$8.64 \cdot 10^{12}$ s^{-1}	120.5	$5.88 \cdot 10^{-3}$ s^{-1}	E_a, 121.8 kJ/mol	$4.03 \cdot 10^{-3}$ s^{-1}
$k_{pair,conc,trim}$	$8.64 \cdot 10^{12}$ s^{-1}	111.0	$9.22 \cdot 10^{-2}$ s^{-1}	E_a, 107.0 kJ/mol	$2.94 \cdot 10^{-1}$ s^{-1}
$k_{iso,tet}$	$1.22 \cdot 10^{3}$ Pa s^{-1}	0	$1.22 \cdot 10^{3}$ Pa s^{-1}	A, $3.51 \cdot 10^{2}$ Pa s^{-1}	$3.51 \cdot 10^{2}$ Pa s^{-1}
$k_{pair,tet}$	$5.72 \cdot 10^{2}$ Pa s^{-1}	0	$5.72 \cdot 10^{2}$ Pa s^{-1}	A, $5.72 \cdot 10^{3}$ Pa s^{-1}	$5.72 \cdot 10^{3}$ Pa s^{-1}
$k_{iso,pent}$	$1.05 \cdot 10^{3}$ Pa s^{-1}	0	$1.05 \cdot 10^{3}$ Pa s^{-1}	A, $1.05 \cdot 10^{2}$ Pa s^{-1}	$1.05 \cdot 10^{2}$ Pa s^{-1}
$k_{pair,pent}$	$5.72 \cdot 10^{2}$ Pa s^{-1}	0	$5.72 \cdot 10^{2}$ Pa s^{-1}	A, $5.53 \cdot 10^{3}$ Pa s^{-1}	$5.53 \cdot 10^{3}$ Pa s^{-1}

Note that the experimental data used was at a fixed temperature (415 K), and thus, adjustments to k values through A or E_a are indistinguishable. Data at multiple temperatures would be required to explore these individual changes further, allowing the impact of varying an activation energy versus a pre-exponential factor to be distinguished. Nevertheless, all changes to the parameters were within the bounds set by adjustments permitted to theoretical values based on inherent DFT errors.

The microkinetic modeling results obtained using the tuned reaction parameters are shown in Figure 2.4, displaying good agreement with the experimental data at pressures below 0.1 kPa and above 1 kPa. A parity plot is shown in Figure 2.5 with an R^2 value of 0.84. The model captures the peak in the rate as a function of pressure due to large methanol cluster inhibition nicely at all fractions of paired sites, and the separation between the curves, with the total rate increasing with increasing fraction of paired sites, is recapitulated well.

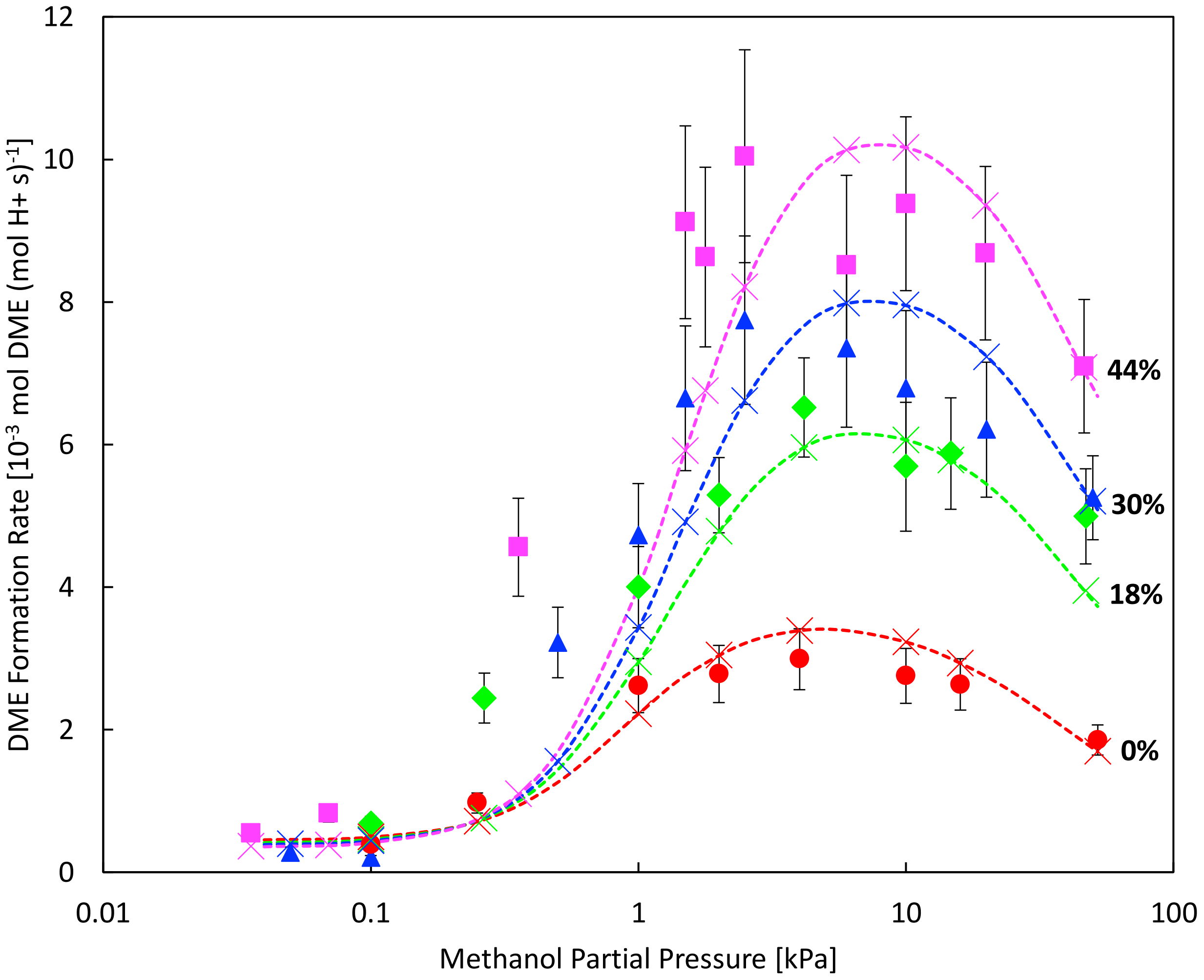

Figure 2.4: Comparison of model output and experimental values for the full range of MeOH partial pressures and paired acid site fractions for 0% paired acid sites (red, ●), 18% paired acid sites (green, ♦), 30% paired acid sites (blue, ▲), and 44% paired acid sites (pink, ■). Markers with error bars are the experimental data from Di Iorio et al.[30] adjusted as described in Section A.2. The crosses identify the output of individual microkinetic model runs at the given paired acid site percentages at methanol partial pressures matching each experimental data point. The dashed lines connecting microkinetic model outputs are presented to guide the eye.

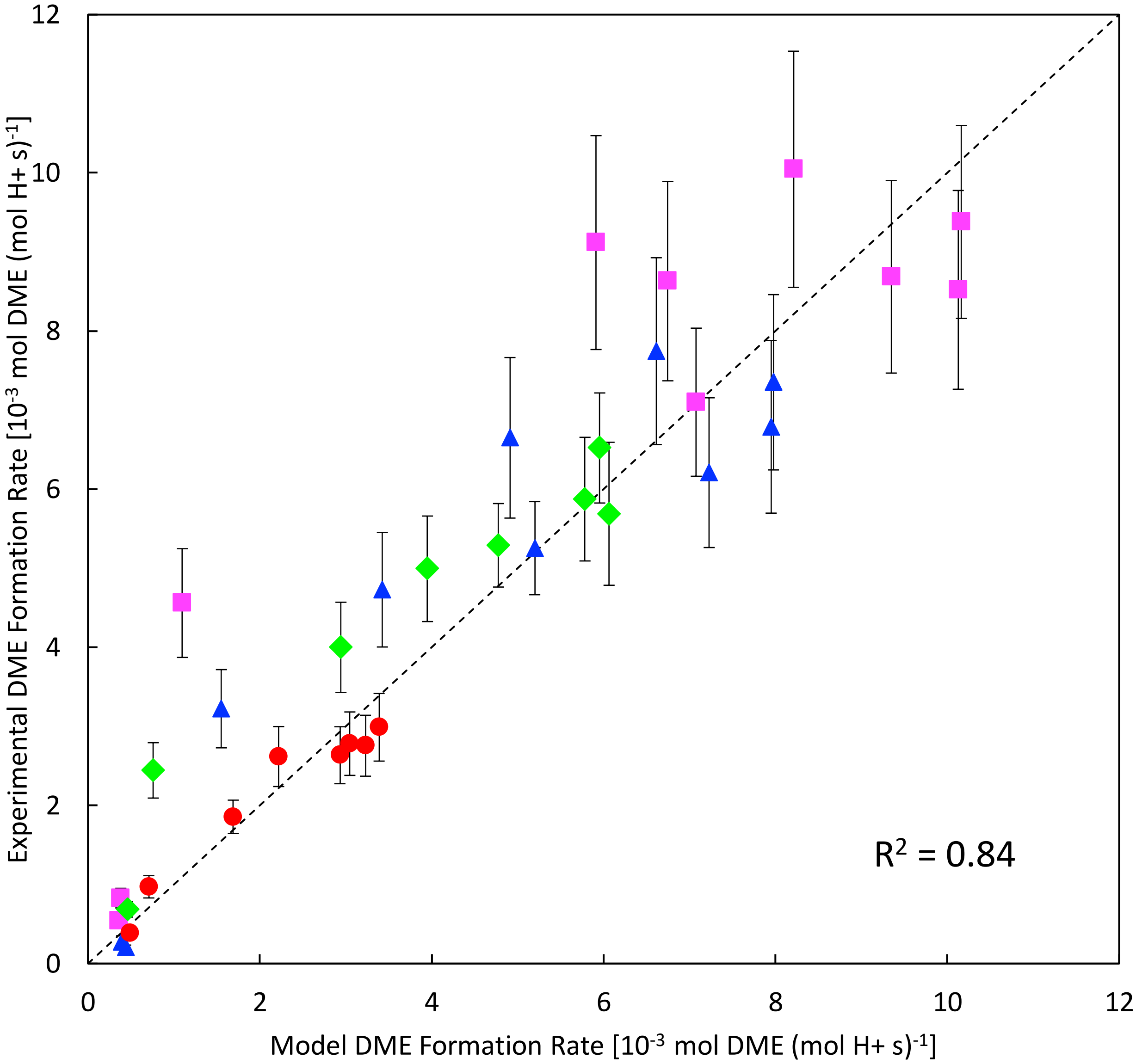

Figure 2.5: Parity plot comparing the model output and value for experimental rate law from the data of Di Iorio et al.[30] at all considered methanol partial pressure conditions for 0% paired acid sites (red, ●), 18% paired acid sites (green, ♦), 30% paired acid sites (blue, ▲), and 44% paired acid sites (pink, ■).

2.4.4. Degree of Rate Control Analysis

A quantitative analysis was performed of the DME formation rates obtained as output from the microkinetic model to understand how the change in activation free energies of elementary steps along the potential energy surface affects the overall reaction rate. Application of this type of sensitivity analysis allows for identification of the elementary step(s) that control overall reaction rates[72-75]. The metric used in the analysis of the degree of rate control for an elementary step i is the sensitivity coefficient (X_i), which is defined by Campbell[76] as Equation 2.9:

$$X_i = \frac{k_i}{r}\left(\frac{\partial \mathrm{r}}{\partial k_i}\right)_{k_{j\neq i},K_i} = \left(\frac{\partial \ln(r)}{\partial \ln(k_i)}\right)_{k_{j\neq i},K_i} = \left(\frac{\partial \ln(r)}{\partial\left(\frac{-\Delta G_i^{TS}}{RT}\right)}\right)_{k_{j\neq i},K_i} \tag{2.9}$$

where r is the net rate of formation of the product of interest, which in this case is taken to be DME. Equation 2.9 was applied to the full set of rate constants in the case of isolated-only and mixed isolated-paired site configurations for a range of reactant feed partial pressures. Figure 2.6 reports the calculated sensitivity coefficients for the cases of isolated-only and binary mixtures containing 18-44 % paired acid sites at a temperature of 415 K. Three representative feed partial pressures of MeOH were chosen – namely, 0.04, 2.5, and 50 kPa. It can be seen that different elementary steps (and corresponding mechanisms) are rate-controlling in different MeOH partial pressure regimes. For example, the water elimination/alkoxide formation ($k_{iso,elim}$ and $k_{pair,elim}$) step of the dissociative pathway is rate-controlling at low MeOH partial pressures (0.04 kPa - red), while direct DME formation from the methanol trimer state ($k_{iso,conc,trim}$ and $k_{pair,conc,trim}$), via the associative mechanism, became rate-controlling at greater pressures (2.5-50 kPa - green, blue). This is mostly consistent with prior rate estimations on isolated sites in CHA using maximum rate analysis—which assumes only one prevailing rate-determining step as a heuristic for determining a mechanism rather than determining degrees of rate control—based on DFT-calculated barriers. This analysis showed that methanol dehydration proceeds primarily via the dissociative mechanism below 0.3 kPa MeOH at 415 K and via the associative mechanism with one spectating methanol above 0.3 kPa[40]. The calculated X_i values indicate that the extent of degree of rate control for the elementary steps considered is a function of the paired site concentration. As the total fraction of paired active sites increased, the calculated X_i values increased proportionately for all elementary steps occurring over paired sites (Figure 2.6b – Figure 2.6d).

In summary, DME formation from the trimer state appears to be rate-controlling for most reactant feed partial pressures and active site configurations (Figure 2.6). This can be attributed to the unique case of trimer states along the potential energy surface of the associative pathway, in which the favorable molecular arrangement results in low reaction barriers and contributes the majority of DME flux at steady state. These trimeric transition states appear to optimize H-bonding between the species in the transition state and with the conjugate base, as illustrated by transition states found in previous work[40] on isolated sites in CHA (Figure 2.7). Only at very low reactant partial pressures does the dissociative mechanism participate in DME formation chemistry, as demonstrated by the calculated X_i values. Conversely, at high reactant partial pressures, the calculated X_i values indicate the trimer state as rate-controlling with calculated values of 0.61-0.83 for paired site fractions of 18-44%. Negligible rates and corresponding X_i values were observed for reactions preceded by tetramer formation, further highlighting the importance of the favorable molecular conformation in the dimer and trimer states. The full set of X_i values calculated for the full range of MeOH partial pressures and paired site fractions is reported in Section A.1. in the Appendix.

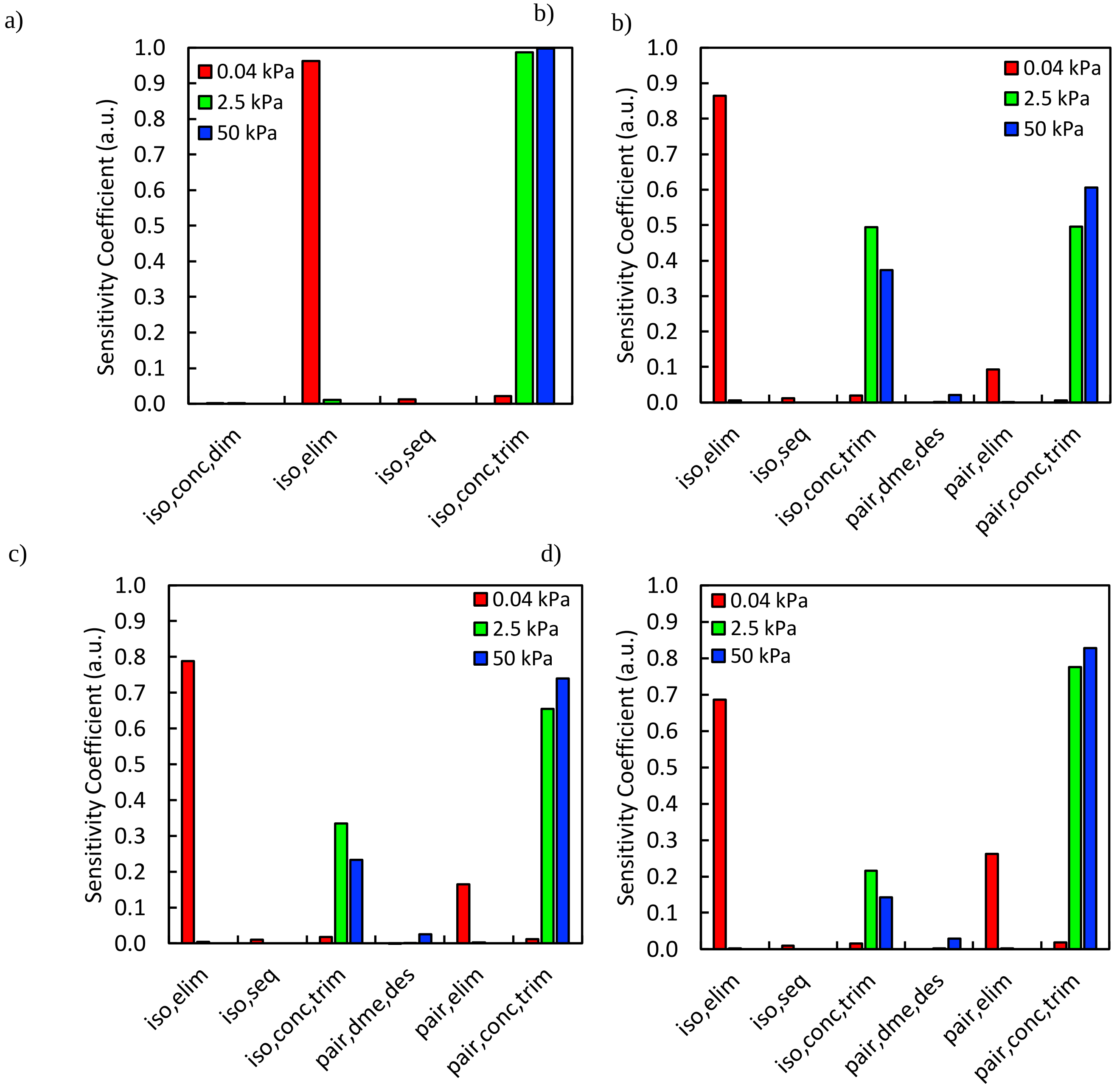

Figure 2.6: Calculated DRC sensitivity coefficients for (a) 0% paired acid sites, (b) 18% paired acid sites, (c) 30% paired acid sites, and (d) 44% paired acid sites at MeOH partial pressures of 0.04 kPa, 2.5 kPa and 50 kPa. All relevant elementary steps are reported using the same notation as in Scheme 1.1.

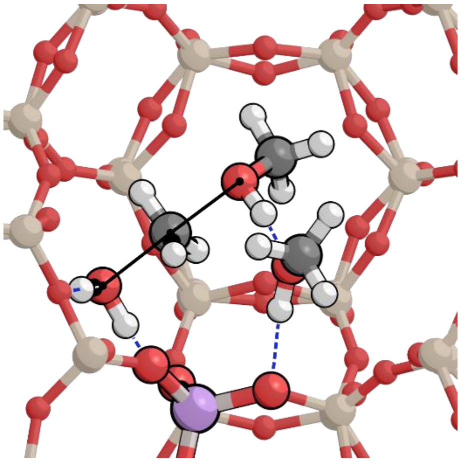

Figure 2.7: The structure of the trimeric concerted methanol dehydration transition state that likely prevails at most conditions, shown here on an isolated site (first described in previous work)[40]. Incipient and breaking bonds are shown with solid black lines, and H-bonds are shown with dashed blue lines.

2.4.5. Reaction Flux and Surface Speciation Analysis

Snapshots of the reactor design equation solutions at the correct isolated site basis along the PFR integration were taken to identify flux through reaction pathways. Flux partitions itself to the two sides (namely, the concerted and sequential pathways) of the mechanism shown in Scheme 2.1. As shown in Figure 2.8a, looking first solely at isolated sites, the sequential pathway dominates at very low methanol partial pressures. As methanol pressure increases, the concerted pathway begins to express with flux through the trimer pathway. As initial methanol pressure continues to increase, the trimer pathway dominates strongly, and the tetramer pathway is never noticeably expressed at any pressure condition. In examining the speciation on the isolated sites under the same conditions as the flux mapped in Figure 2.8a, an interesting result is seen in Figure 2.9. At a methanol pressure of 1000 Pa, bound methanol trimers have nearly equal speciation with the combination of methanol monomers and dimers. However, the trimer pathway completely dominates the mechanism at this pressure, due in part to the much lower activation energy for the *conc,trim* steps compared to the *conc,tet* and *conc,dim* steps, even prior to any tuning of the DFT values. The tetramer pathway shows no significant contribution to the overall DME flux, even at conditions where tetramers make up a significant portion of the speciation, such as 50 kPa of methanol. Notably, the primary bound species present are the bound methanol monomers, dimers, trimers, tetramers, and pentamers as well as the methoxy species indicative of the sequential pathways. All other surface species are only present in negligible amounts.

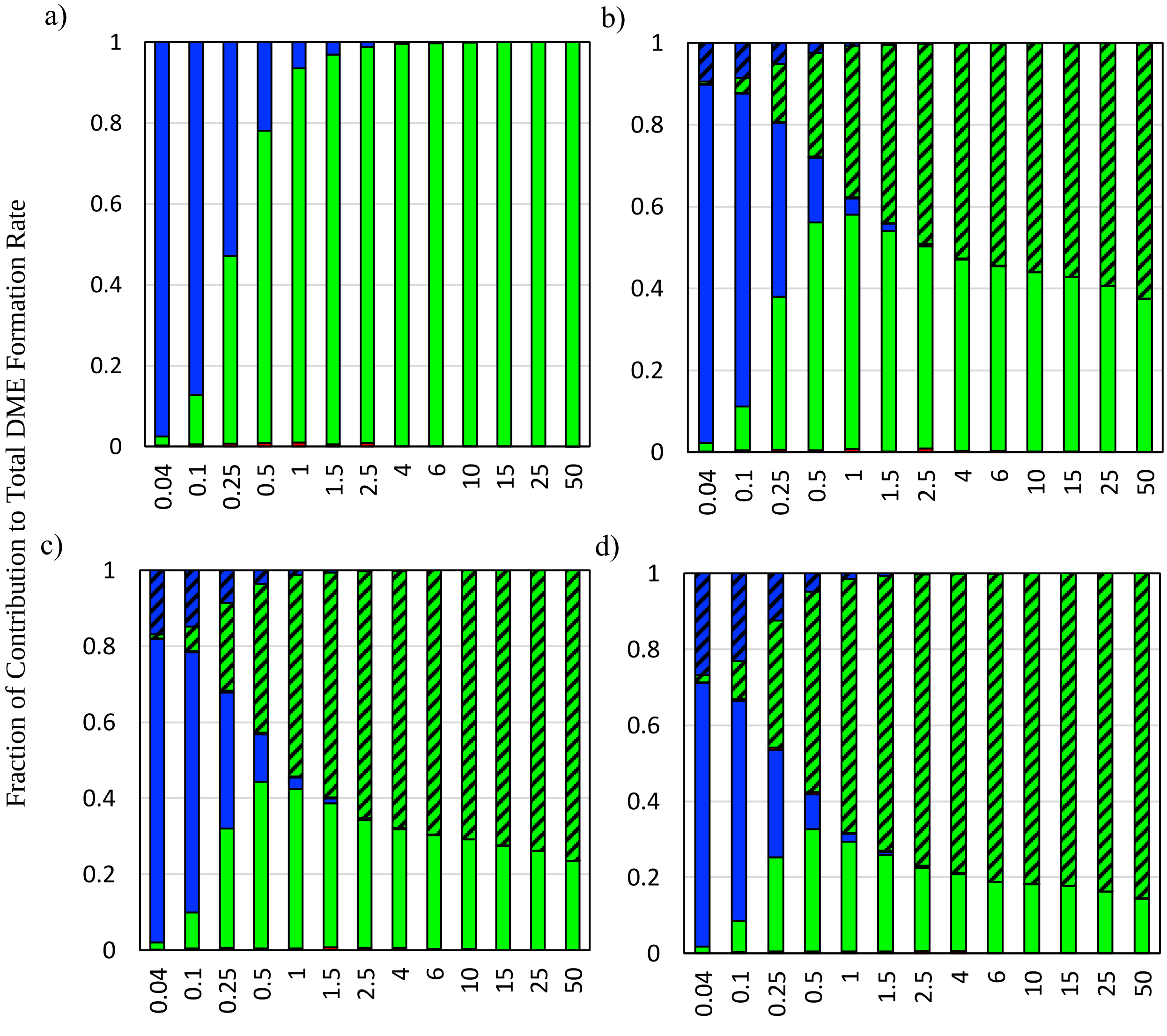

Figure 2.8: The fraction of each primary branch of the mechanism's contribution to overall DME production for (a) 0% paired acid sites, (b) 18% paired acid sites, (c) 30% paired acid sites, and (d) 44% paired acid sites. Red: Contribution from MeOH dimer pathway. Green: Contribution from MeOH trimer pathway. Blue: Contribution from sequential pathway. Unshaded bars correspond to contributions from isolated acid sites, whereas shaded bars correspond to contributions coming from paired acid sites.

Figure 2.8b-d shows the partitioning of the flux as a function of methanol partial pressure as the number of paired sites increases. Paired sites display similar flux behavior to isolated sites, though their rates are higher and thus their contribution to the total is significant. Note that four major categories of fluxes can be gleaned from these figures: sequential on isolated sites, sequential on paired sites, concerted on isolated sites (primarily through MeOH trimers) and concerted on paired sites. It is clear from the variety of contributions in Figure 2.8b-d that the total rate of DME production captured in Figure 2.8 is a complex amalgam of these routes, the contributions of which change as the reaction conditions change. At low methanol pressure, the sequential pathway dominates despite the low absolute coverage of methoxy species shown in Figure 2.9 due to the even lower coverage of the trimer species that promote the rapid concerted pathway. As methanol partial pressure increases, the dimer and trimer pathways become expressed, ultimately resulting in the paired trimer pathway dominating overall DME flux for the system at high pressure conditions.

The speciation as a function of MeOH partial pressure and fraction of paired sites is shown in Figure 2.9. In the presence of paired sites, isolated sites show no significant differences in speciation or numerical contribution to flux. Paired sites also show consistent speciation at different ratios of isolated sites to paired sites. At the pressure conditions investigated, monomers dominate at low pressure but are replaced by trimers as pressure increases. Bound dimer species are generally less prominent on paired sites compared to isolated sites. Tetramer and pentamer species also express lower percentages at high methanol partial pressure conditions on paired sites, with methanol trimers dominating the surface at methanol partial pressures ranging from 1.5 to 50 kPa. Given that the trimer pathway is identified to be responsible for the majority of flux in the isolated case and that the tetramer pathway shows little to no flux contribution despite high surface concentration, this higher trimer surface concentration partly accounts for the overall higher DME flux of paired sites in comparison to isolated sites along with the more beneficial activation energies along the trimer pathway for paired active sites.

In summary, the speciation and flux analyses identify the MeOH trimer pathway to be the dominant pathway for DME production. Trimers form more readily on paired acid sites at high MeOH partial pressures in comparison to inactive tetramers and pentamers while dominating the surface coverage, which when paired with the lower energy barriers along the trimer pathway for paired active sites rationalizes the higher DME formation turnover rates (per H^+) identified on paired acid sites.

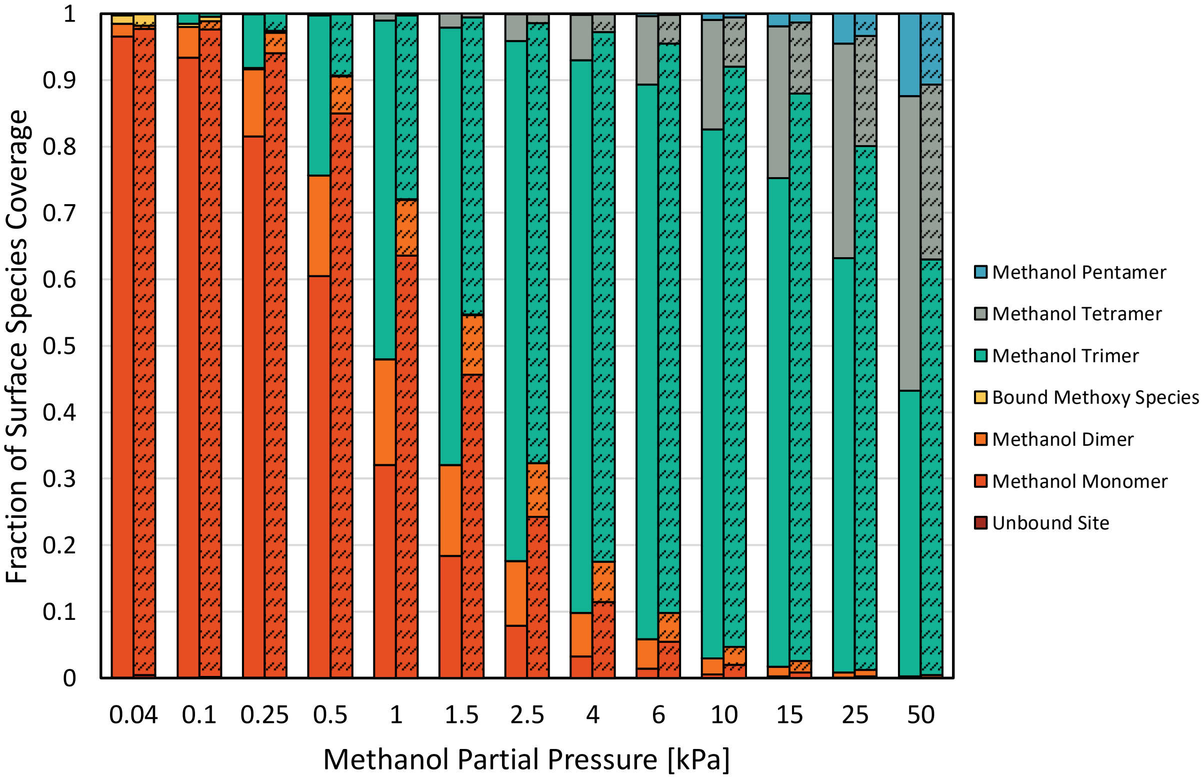

Figure 2.9: Surface species coverage at various MeOH partial pressures at the outlet of the simulated PFR. Methanol monomers dominate the speciation at lower pressures, with trimers and tetramers becoming most prevalent as methanol partial pressure rises to 50 kPa. Left: Isolated acid sites. Right (shaded): Paired acid sites.

2.5. Conclusions

In this work, a DFT-parameterized microkinetic model is presented that captures and identifies the effects of acid site proximity in CHA on methanol dehydration rates. Through flux analysis and surface species identification, two primary drivers of methanol dehydration chemistry were identified. At methanol pressures below 250 Pa, a sequential pathway through a bound methoxy intermediate dominates. Above 250 Pa of methanol pressure, the rapid formation of methanol trimer clusters causes a shift in flux through the concerted trimer pathway. NNN paired acid sites promote the formation of trimer species over inhibiting tetramer or pentamer clusters and have lower energy barriers presented in the concerted trimer pathway, resulting in the large increase in rate of dimethyl ether production for this class of sites. This modeling methodology and framework can be extended to capture the effects of paired active site chemistry on additional zeolite frameworks beyond CHA and on chemistries beyond methanol dehydration, aiding in the development of next-generation catalysts.

Chapter 3: Microkinetic Modeling of the Homogeneous Thermal Oligomerization of Ethylene to Liquid-Fuel Range Hydrocarbons

Material in this chapter is based on collaborative work from Grant Marsden, Alexander Shaw, Matthew A. Conrad, Jeffrey T. Miller, and Linda J. Broadbelt.

3.1. Abstract

The thermal oligomerization of ethylene is a key reaction for the energy transition. Despite the long history surrounding this reaction, a lack of quantum chemical simulations has led to a lack of mechanistic understanding behind this important process. In this work, a density functional theory-parameterized microkinetic model was developed to unravel the primary drivers of initiation and understand the formation of odd-numbered carbon products. Through flux analysis, the main driver of initiation was identified to be hydrogen abstraction from ethylene by a 1,4-butyl diradical produced from the reaction of two ethylene molecules. As conversion increases, the primary initiation mode was seen to switch to hydrogen abstraction by a butene diradical as 1-butene began to be produced in high quantities. Odd-numbered carbon species were seen to originate from the β-scission of hydrogen-shifted C_8 radical species. The significant quantity of linear terminal olefins in the experimental product distribution was identified to originate from the formation of vinyl radicals through hydrogen abstraction reactions involving ethylene that were then propagated via radical addition reactions to ethylene. The insights from this work can aid in the development of intensified reactor systems meant to directly valorize ethane streams from shale gas production, converting waste streams directly to usable fuel products.

3.2. Introduction

The valorization of ethane has rapidly become a key topic for the global energy economy.[77] Shale gas feedstocks are rich in excess ethane that must be disposed of, typically by flaring.[78, 79] Upgrading this ethane to ethylene and further oligomerizing this ethylene into liquid fuel-range products at the site of production provides an opportunity for utilizing what is otherwise a direct waste stream.[80] Catalytic methods of upgrading ethylene feedstocks can be effective but come with a number of drawbacks, either requiring significant surrounding architecture and capital or struggling with deactivation and lifetime.[81-87] As such, thermal processes for upgrading ethylene have long been investigated, though catalytic processes still dominate industrially due to favorable selectivities towards beneficial product distributions at more mild conditions than classical thermal upgrading.[88]

However, a recent study has shown the potential for upgrading ethylene at milder conditions, seeing significant conversion below 500 °C.[89] Interestingly, the product distribution for this reaction includes a number of odd-numbered carbon species, yet it lacks significant production of methane or ethane. There is also significant preference towards linear terminal olefins and a high concentration of 1-butene.

Despite the long history of this class of reactions and a number of proposed mechanisms,[90-102] there is a notable absence of quantum chemical simulations, leading to a lack of mechanistic understanding. There has been much speculation in this area, with proposals of diradical initiation reaching as far back as the work of Hurd et al. in 1934,[90] yet quantum chemical simulation has as of yet not been applied to resolve the key drivers of initiation. This recent experimental study provides the opportunity to resolve this near-century-old question through microkinetic modeling.

A microkinetic model designed to unravel the growth and emergence of odd-numbered carbon species in the thermal oligomerization of ethylene with an explicit density functional theory (DFT) parameterized initiation scheme is developed. The findings of this work can aid in the development of intensified reactor systems for the direct valorization of ethane streams from shale gas production to convert would-be waste into usable fuel products.

3.3. Computational Methods

3.3.1. Microkinetic Modeling

The microkinetic model was constructed based on a set of ordinary differential equations encompassing the change in concentration of gaseous species, both molecules and radicals, within the proposed mechanism. First, the equations defining the rate of each elementary step in the reaction mechanism took the form:

$$r_i = A_i \exp\left(-\frac{E_{a,i}}{RT}\right) \prod_{j}^{reactants} P_j \tag{3.1}$$

Where r_i is the rate of elementary step i, A_i is the pre-exponential factor, $E_{a,i}$ is the activation energy, R is the universal gas constant, T is the temperature, and P_j is the partial pressure of reactant j. A set of ordinary differential equations spanning the gaseous species was arranged from these rates, leading to the following:

$$\frac{dF_j}{dV} = \sum_i \nu_{i,j} r_i \tag{3.2}$$

Where $\nu_{i,j}$ is the stoichiometric number of species j in elementary step i, F_j is the molar flowrate of reactant j, and V is the volume of the system being integrated over. This set of ordinary differential equations was then paired with the design equation for a pressure-based plug flow reactor to match with experimental conditions. The key parameters of the experiment that were modeled were: a pure feed of C_2H_4, a plug-flow reactor volume of 30 cm^3, a constant temperature control of 465°C, a feed flow of 156 sccm, and two separate constant pressure conditions of 15.0 and 25.0 bar.[89]

To parameterize the model, elementary steps were assumed to be of Arrhenius form, and the activation energies were postulated to follow the Evans-Polanyi principle, defined as:

$$E_a = E_0 + \alpha \Delta H_{rxn}^0 \quad if\ \Delta H_{rxn}^0 > 0;$$

$$E_a = E_0 + (1-\alpha)\Delta H_{rxn}^0 \quad if\ \Delta H_{rxn}^0 < 0 \tag{3.3}$$

Where E_a is the activation energy, E_0 is a reference energy for a group of similar reactions, α is the transfer coefficient (defined in the endothermic direction), a measure of the similarity of a reaction's transition state to its reactant or product state with a value of 0 representing the reactant state and 1 the product state, and ΔH_{rxn}^0 is the enthalpy of reaction.[103, 104] Elementary steps were grouped by similarity according to this principle into classifications known as reaction families. Each reaction family was assumed to share the parameters E_0 and α, for use in calculating activation energy, as well as a pre-exponential factor. Calculation of the heat of formation for all species, including radical intermediates, was done through Benson's group additivity, in which sections of molecules are assigned consistent contributions to the molecule's overall heat of formation and summed.[105]

For the reactions for which rate coefficients were calculated directly from DFT, to account for uncertainty in parameters derived from density functional theory, including those aggregated for reaction families, activation energies or E_0 values were tuned within bounds of ±1.4 kcal/mol, whereas pre-exponential factors were tuned within the bounds of one order of magnitude. Optimization of parameters was done on all three test cases simultaneously, using the experimental carbon selectivity and conversion as objective points. The microkinetic model was solved using the differential-algebraic solver DDASAC,[106] selected due to success in solving stiff ordinary differential equations.

3.3.2. Density Functional Theory

Density functional theory calculations were performed using the Gaussian 16 software.[107] All geometries and energies were calculated using the M062X functional[108] in conjunction with the Def2TZVP basis set.[109] Dispersion was included in the form of Grimme's D3 correction with zero damping. Contributions to the entropy from vibrational modes below 100 cm^{-1} were corrected using the quasi-harmonic approach of Grimme,[110] as implemented in the GoodVibes software,[111] and contributions from the same low frequency modes to the enthalpy were corrected using the approach of Head-Gordon and co-workers.[112] GoodVibes was further employed to scale all vibrational frequencies by a factor of 0.97, the recommended value from Truhlar et al.[113] All thermodynamic values are reported at 1 atm of pressure and at 25 °C. All geometry minima were confirmed to have zero imaginary frequencies, while transition state structures showed exactly one negative frequency mode.

Temperature dependent rate constants for the forward and reverse direction of each elementary reaction were calculated using the Eyring equation, which takes the form:

$$k(T) = \kappa(T)\ \frac{k_B T}{h} (c^0)^{1-m} e^{\left(-\frac{\Delta G^{\neq}}{RT}\right)} \tag{3.4}$$

where k_B is the Boltzmann constant, T is the absolute temperature, h is the Plank constant, c^0 is a standard state concentration factor and m is the molecularity of the elementary reaction. The $\Delta G^{\neq}$ term is the free energy barrier of the elementary reaction in the forward or reverse direction and R is the universal gas constant. The κ(T) term is the Wigner tunneling correction factor of the form:

$$\kappa(T) = 1 + \frac{1}{24}\ \left(\frac{h|v|}{k_B T}\right)^2 \tag{3.5}$$

where $|v|$ is the magnitude of the negative frequency associated with the transition state reaction coordinate.

The Arrhenius parameters of E_a and A for both the forward and reverse reactions were obtained by plotting the natural log of the rate constant at three temperatures against the reciprocal of the temperature. The y-intercept of this plot gives the value of $ln(A)$, and the slope is equal to $-E_a/R$. The calculated A and E_a values are provided in Table 3.1 in Section 3.4.2.

3.4. Results and Discussion

3.4.1. Reaction Mechanism

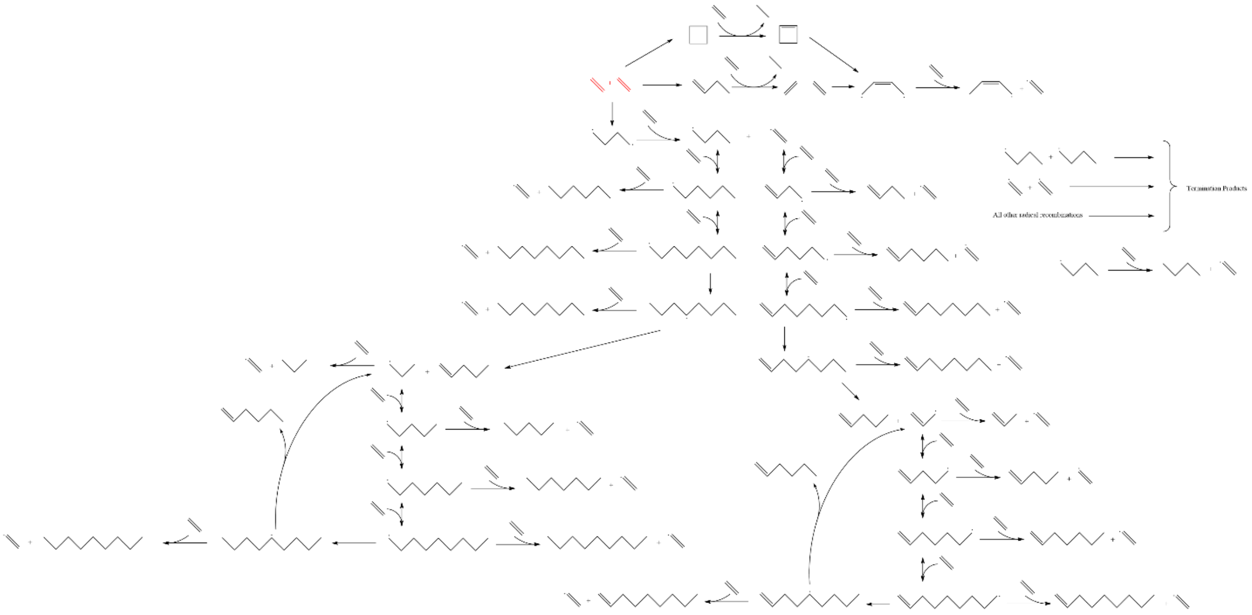

Figure 3.1: The reaction mechanism for the microkinetic model of homogeneous thermal oligomerization of ethylene.

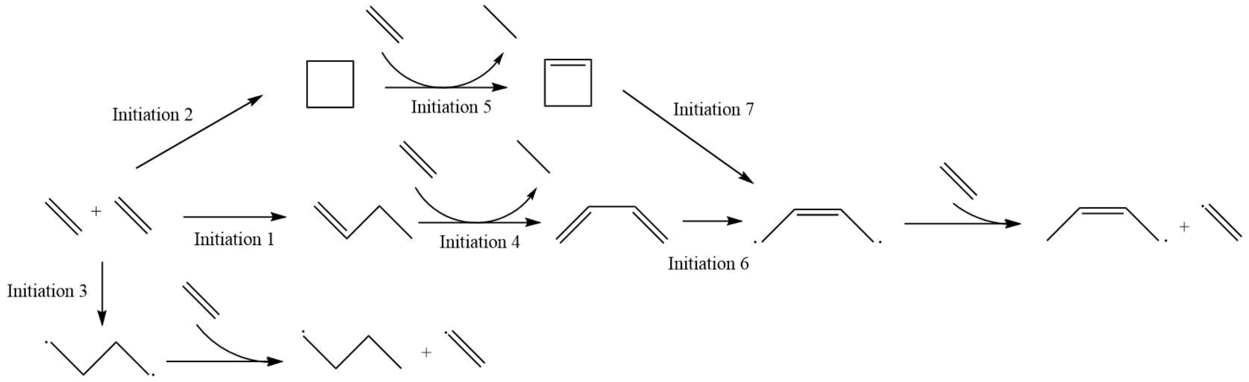

Figure 3.2: Labels for initiation steps for ease of reference.

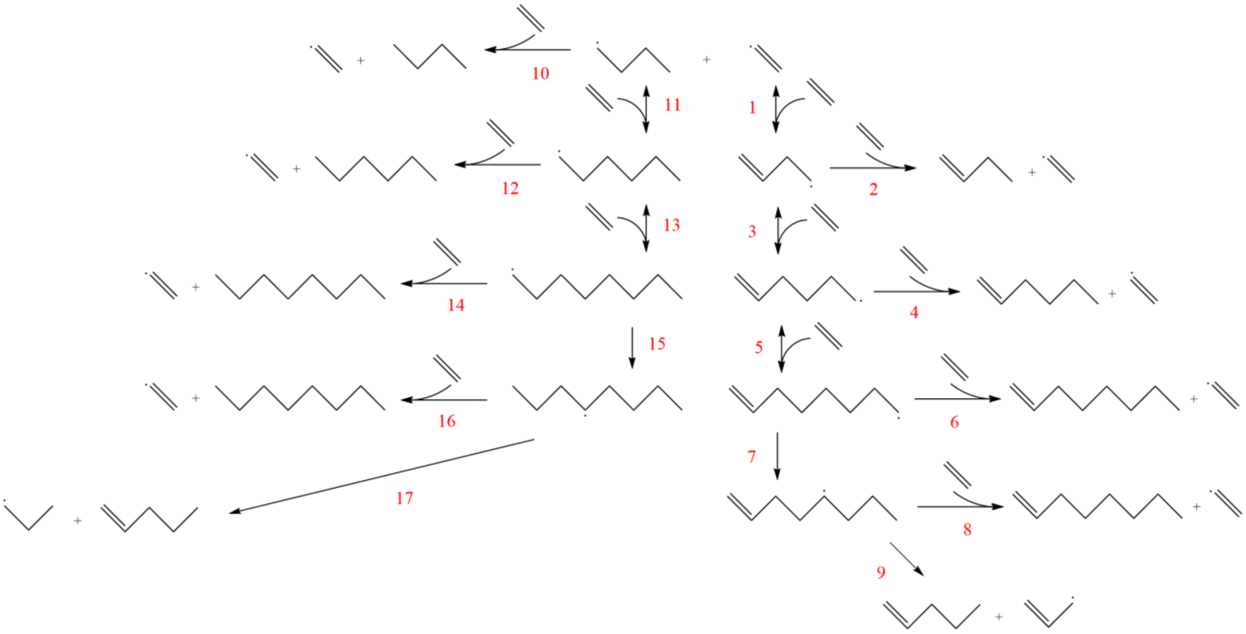

Figure 3.3: Numeric labels for even-numbered carbon species addition and hydrogen abstraction events, hydrogen shift, and β-scission of C_8 species.

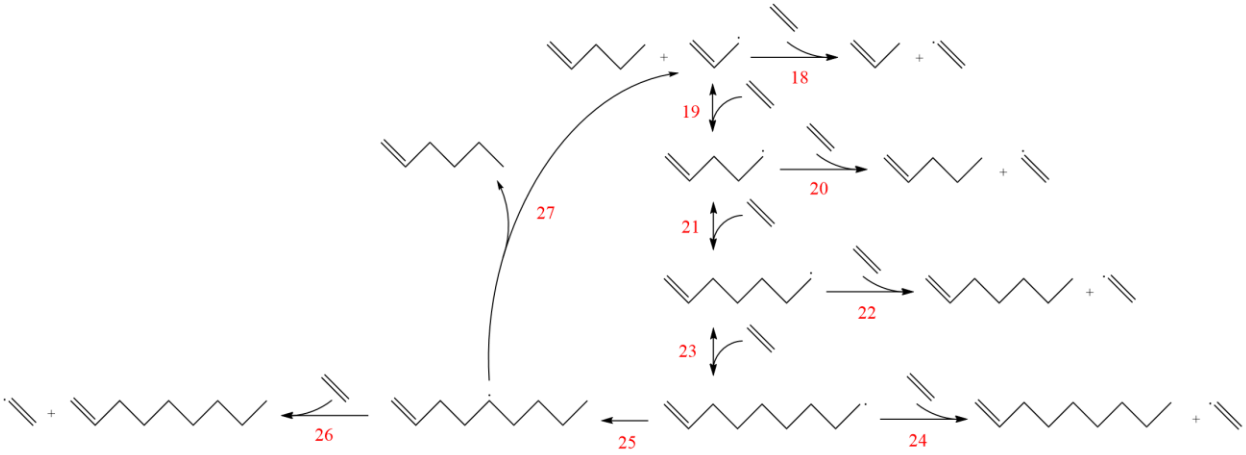

Figure 3.4: Numeric labels for odd-numbered carbon alkene species addition, hydrogen abstraction, hydrogen shift, and β-scission events.

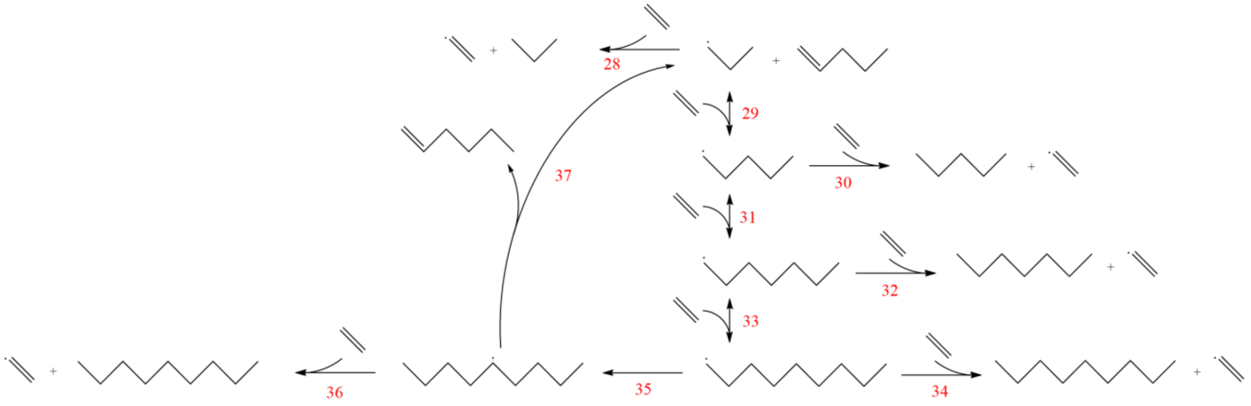

Figure 3.5: Numeric labels for odd-numbered carbon alkane species addition, hydrogen abstraction, hydrogen shift, and β-scission events.

The modeled reaction mechanism for the homogeneous thermal oligomerization of ethylene, shown in Figure 3.1, begins with two ethylene molecules following three possible bimolecular reactions: the formation of cyclobutane, the formation of 1-butene, and the formation of a C_4 diradical that undergoes hydrogen abstraction to form 1-butyl radical and the vinyl radical that is key to propagation. The 1-butene path and cyclobutane path encounter similar endpoints, with ethylene abstracting a hydrogen atom from either cyclobutane or 1-butene to form ethane and a resonance-stabilized 2-butenyl-1,4-diradical, which then abstracts hydrogen from ethylene to form 2-butene radical and vinyl radical.

Propagation is dominated by the major reaction families of hydrogen abstraction and radical addition. The primary cycle begins with addition of ethylene to vinyl radical to form 1-buten-4-yl radical in an even-chain growth scenario. Through reaction with ethylene, the dominant species at low to moderate conversion, this 1-buten-4-yl radical can then undergo abstraction, forming 1-butene and regenerating the vinyl radical, or undergo further addition to 1-hexen-6-yl radical. This pattern of abstraction and addition options continues through C_8 radical, at which point hydrogen shift reactions offer possibilities to generate odd-numbered carbon species. Both 1,4- and 1,5-intramolecular hydrogen shift reactions were incorporated into the mechanism.

After hydrogen shift, β-scission of C_8 radical forms 1-pentene and allyl radical. This begins a cycle of odd-carbon-number propagation, with hydrogen abstraction from ethylene reforming vinyl radical and creating odd numbered olefins. Ethylene addition in this cycle was modeled through 1-nonen-9-yl radical, since significant quantities of C_{10+} were not identified in experiment, at which point hydrogen shift can allow for β-scission to form 1-hexene and regenerate allyl radical.

An equivalent series of reactions was applied to the 1-butyl radical that forms with vinyl radical from 1,4-butyl abstracting hydrogen from ethylene. This results in even-numbered alkyl chain growth, modeled through 1-octyl radical, at which point either 1,4-hydrogen shift or 1,5-hydrogen shift can form an equivalent product of 4-octyl radical. This 4-octyl radical species can undergo β-scission to form pentene and 1-propyl radical, which undergoes a similar cycle to allyl radical of odd-carbon number chain growth and hydrogen abstraction up through C_9 alkyl radical. When this C_9 alkyl radical undergoes hydrogen shift, it is able to undergo β-scission to form 1-hexene and regenerate 1-propyl radical. All alkyl radical species are able to abstract hydrogen from ethene, resulting in the formation of vinyl radical, which is eligible for the propagation reactions described earlier. Termination occurs through radical recombination, and all possible permutations of recombination were modeled within the mechanism.

3.4.2 Microkinetic Modeling

The initial values for all of the kinetic parameters are shown in Table 3.1. Labels of the initiation steps for referencing with the parameter table are shown in Figure 3.2. Additional numeric labels for reaction steps are presented in Figures 3.3-3.5. Examples of reactions within each reaction family are presented in Figure 3.6.

Table 3.1: Initial values for parameters for the reactions in Figure 3.1. Reaction family parameters were taken from the literature, and the parameters for the initiation steps were derived from density functional theory calculations reported earlier.

Parameter	**A ($Pa^{-1}s^{-1}$ or s^{-1})**	**E_0 or E_a (kcal/mol)**	**A**
H-Abstraction[a,114]	$4.48 \cdot 10^{1}$	12.0	0.5
Addition[a,114]	$4.69 \cdot 10^{0}$	11.4	0.24
End-chain β-scission[b,114]	$1.29 \cdot 10^{13}$	11.4	0.76
Mid-chain β-scission[b,114]	$5.35 \cdot 10^{14}$	11.4	0.76
Recombination[a,115]	$1.63 \cdot 10^{1}$	1.47	0
1,4 H-shift[b,114]	$1.58 \cdot 10^{11}$	20.8	-
1,5 H-shift[b,114]	$1.82 \cdot 10^{10}$	13.7	-
Initiation Label 1[a,89]	$2.73 \cdot 10^{0}$	68.4	-
Initiation Label 2[a,89]	$2.05 \cdot 10^{0}$	67.4	-
Initiation Label 3[a,89]	$3.31 \cdot 10^{3}$	67.0	-
Initiation Label 4[a,89]	$1.44 \cdot 10^{-1}$	42.0	-
Initiation Label 5[a,89]	$1.42 \cdot 10^{0}$	45.1	-
Initiation Label 6[b,89]	$1.10 \cdot 10^{15}$	56.5	-
Initiation Label 7[b,89]	$1.19 \cdot 10^{16}$	48.6	-

[a] Bimolecular reaction, units $Pa^{-1}s^{-1}$. [b] Unimolecular reaction, units s^{-1}.

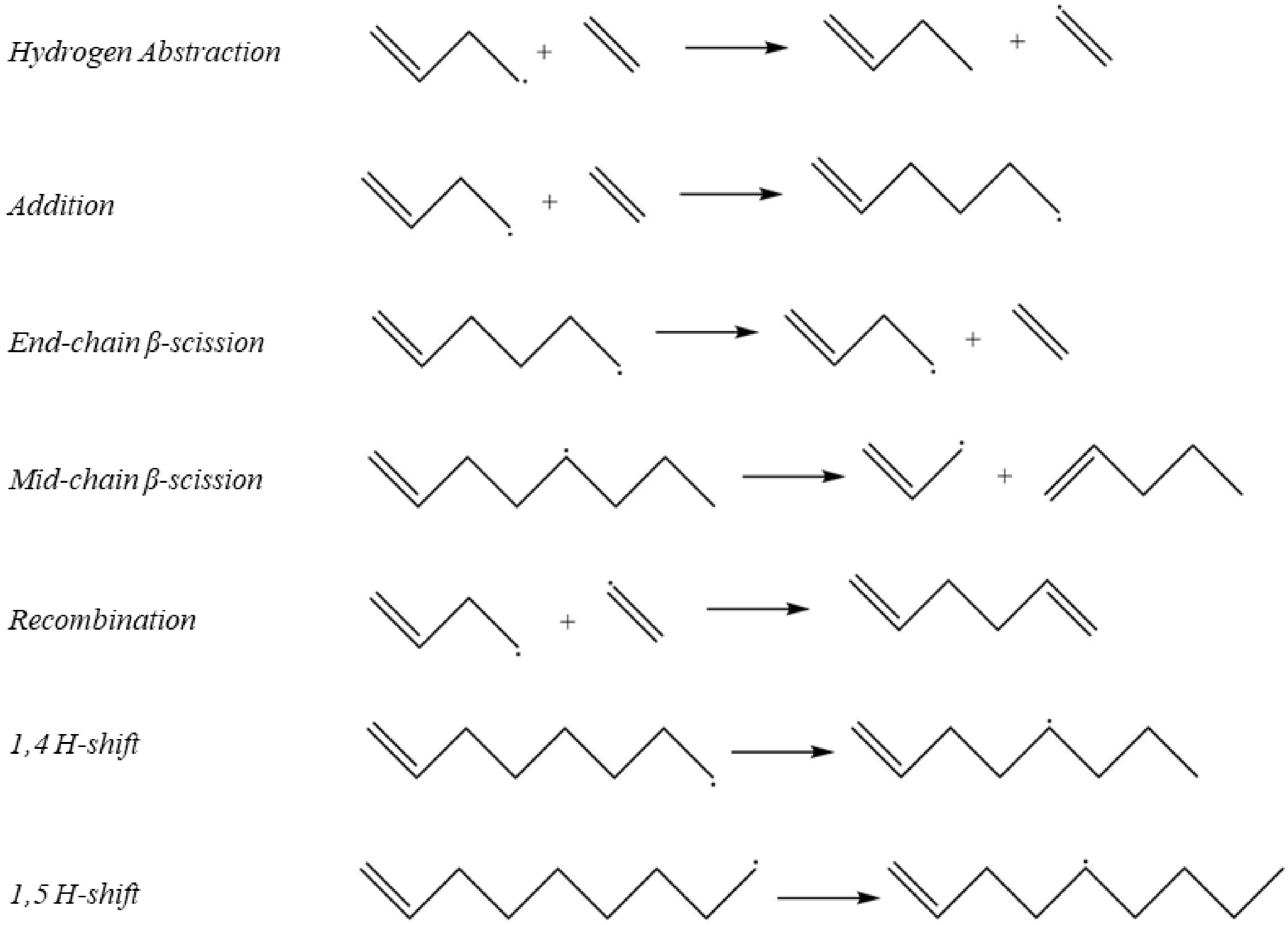

Figure 3.6: Representative examples of modeled reaction families.

As described in Section 3.3.1, parameters were tuned within the bounds of ±1.4 kcal/mol for activation energies or E_o values and ±1 order of magnitude for pre-exponential factors. The final values for the parameters are shown in Table 3.2.

Table 3.2: Final values of parameters based on optimization against experimental data. Pre-exponential factors were tuned with bounds of ±1 order of magnitude, whereas activation energies or E_o values were tuned within the bounds of ±1.4 kcal/mol.

Parameter	**Original A**	**Optimized A**	**E_0 or E_a (kcal/mol)**	**Optimized E_0 or E_a (kcal/mol)**
H-Abstraction[a]	$4.48 \cdot 10^{1}$	$4.39 \cdot 10^{2}$	12.0	11.0
Addition[a]	$4.69 \cdot 10^{0}$	$4.69 \cdot 10^{-1}$	11.4	12.8[c]
End-chain β-scission[b]	$1.29 \cdot 10^{13}$	$3.10 \cdot 10^{12}$	11.4	12.8[c]
Mid-chain β-scission[b]	$5.35 \cdot 10^{14}$	$5.35 \cdot 10^{15}$	11.4	12.8[c]
Recombination[a]	$1.63 \cdot 10^{1}$	$4.11 \cdot 10^{0}$	1.47	1.89
1,4 H-shift[b]	$1.58 \cdot 10^{11}$	$1.58 \cdot 10^{12}$	20.8	19.4
1,5 H-shift[b]	$1.82 \cdot 10^{10}$	$1.82 \cdot 10^{9}$	13.7	15.1
Initiation Label 3[a]	$3.31 \cdot 10^{3}$	$3.31 \cdot 10^{4}$	67.0	65.6
Initiation Label 4[a]	$1.44 \cdot 10^{-1}$	$1.44 \cdot 10^{0}$	42.0	40.6
Initiation Label 6[a]	$1.10 \cdot 10^{15}$	$1.10 \cdot 10^{14}$	56.5	57.9

[a] Bimolecular reaction, units $Pa^{-1}s^{-1}$. [b] Unimolecular reaction, units s^{-1}. [c] E_o values for reaction families that are the reverse of one another are equal to maintain thermodynamic consistency and are constrained accordingly during optimization.

These parameters were used in the microkinetic model developed around the mechanism shown in Figure 3.1, as described in Section 3.3.1. The outputs of the microkinetic model at 15 and 25 bar are shown in Figure 3.7.

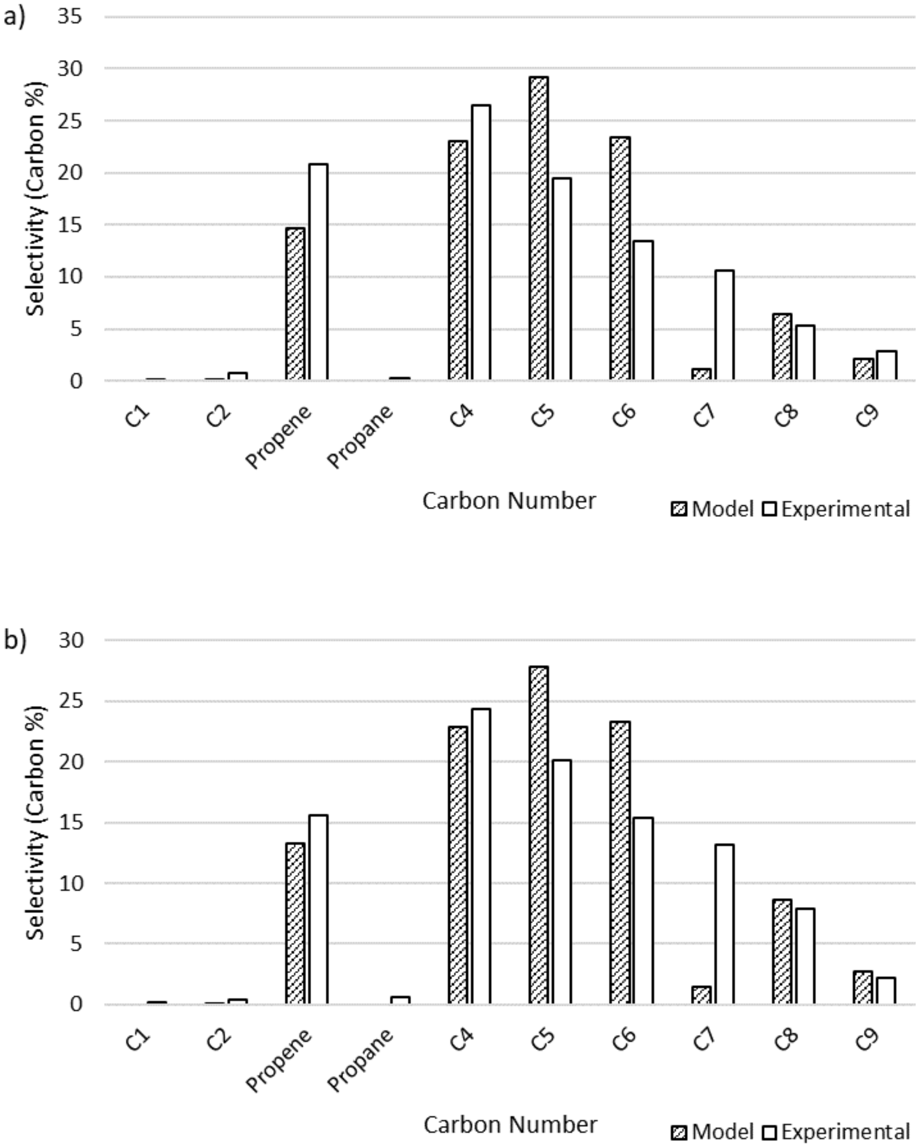

Figure 3.7: Microkinetic model output showing selectivity measured by carbon percent for different carbon number species. a) Pressure of 15 bar. Model conversion: 20.6%. Experimental conversion: 21%. b) Pressure of 25 bar. Model conversion: 63.7%. Experimental conversion: 56%.

The microkinetic model results display reasonable agreement for conversion as a function of pressure as well as formation of olefins of all carbon numbers. Notably, the formation of odd-numbered carbons is generally captured well, with significant quantities of C_3, C_5, and C_9 being observed. While there is some overshoot in the prediction of C_5 and C_6 species, a notable shortcoming of the model is in the undershoot of C_7 formation. A possible explanation of this shortcoming is in the truncation of the model at C_9, which was implemented to maintain a manageable model size and driven by the lack of experimentally observed C_{10+} species, preventing the formation of high-molecular weight carbon species that could undergo favorable β-scission to form C_7 product.

3.4.3. Reaction Flux Analysis

3.4.3.1. Ethylene Consumption

A comparison of all different reactions that consume ethylene is presented in Figure 3.8, taken at three different points along the simulated reactor: 10^{-10} cm^3 to represent differential conversion, 10^{-1} cm^3 as a conversion mid-point, and 30 cm^3 for the reactor outlet. For differential conversion at 15 bar, several trends emerge. The results are shown using a log scale, due to the large range in the order of magnitude of different reaction pathways. At differential conversion, ethylene is consumed by initiation reactions; specifically, hydrogen abstraction by 1,4-butyl diradical is seen to be many orders of magnitude faster than that by the butene diradical and is the fastest reaction recorded. Hydrogen abstraction from ethylene and addition to ethylene have roughly equivalent rates for a given radical (e.g., 1-hexenyl radical), and rates of a given reaction type involving either an alkenyl or alkyl radical are similar. However, as simulated volume increases, and thus conversion increases, alkenyl radicals begin to dominate, and thus, rates for a reaction of a given type (i.e., hydrogen abstraction or radical addition) of alkenyl radicals are much higher than those of alkyl radicals of the same carbon number. The concentration of vinyl radical increases disproportionately to the concentration of 1-butyl radical as the kinetic chain emerges and initiation effects are less significant. The net flux of butene diradical hydrogen abstraction begins to overtake that of the 1,4-butyl diradical hydrogen abstraction as the conversion of 1-butene to butadiene becomes a dominant reaction. At 25 bar, these trends are maintained, though the differential conversion point is already notably approaching the pattern seen in higher volume conditions, given that the conversion is higher at a given reactor volume when the pressure is higher.

a) 15 bar:

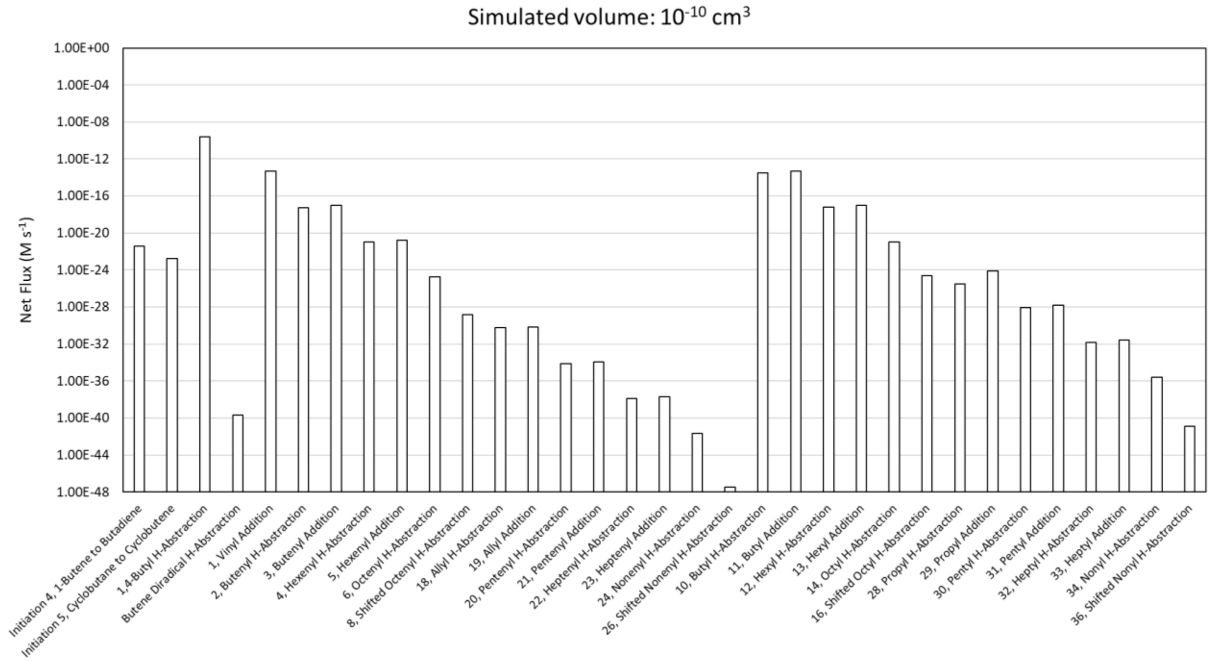

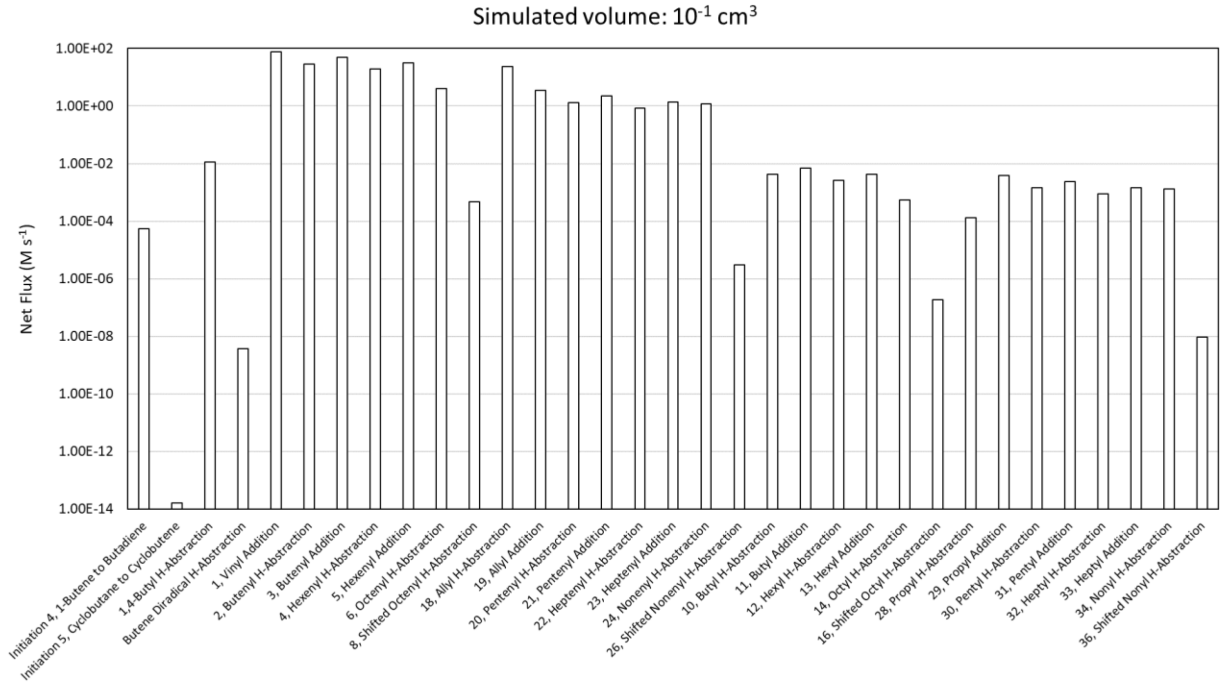

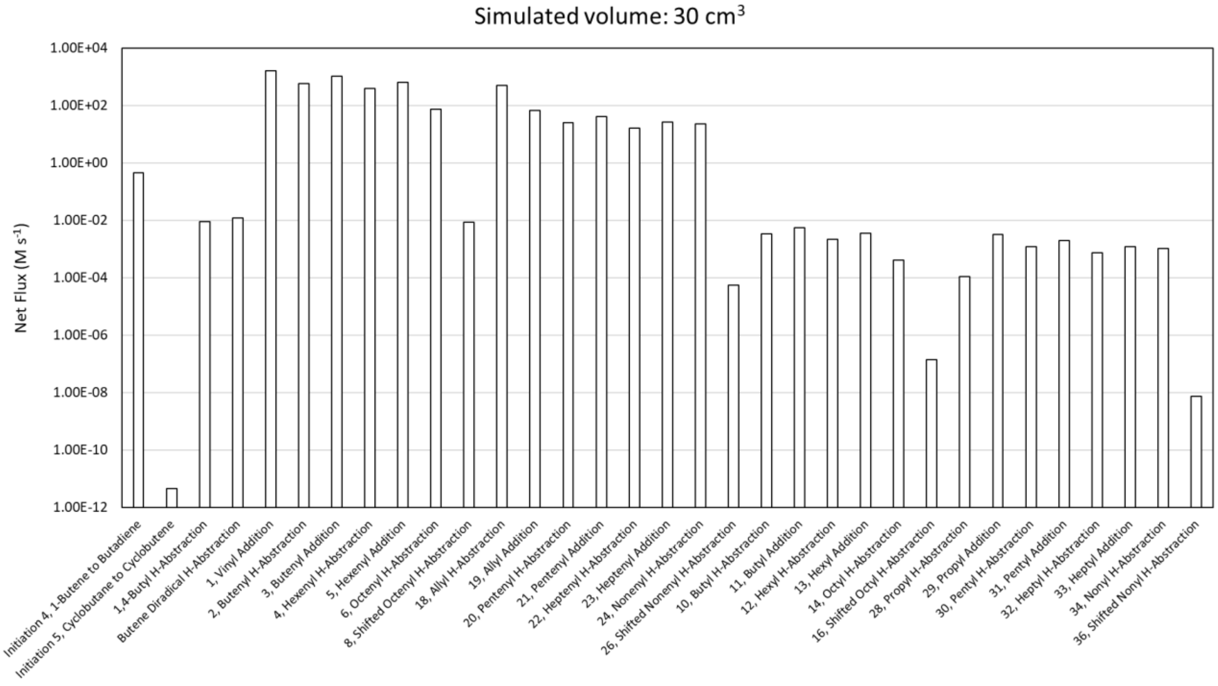
Simulated volume: 30 cm^3
Net Flux (M s^{-1})
1.00E+04
1.00E+02
1.00E+00
1.00E-02
1.00E-04
1.00E-06
1.00E-08
1.00E-10
1.00E-12
Initiation 4, 1-Butene to Butadiene
Initiation 5, Cyclobutane to Cyclobutene
1,4-Butyl H-Abstraction
Butene Diradical H-Abstraction
1, Vinyl Addition
2, Butenyl H-Abstraction
3, Butenyl Addition
4, Hexenyl H-Abstraction
5, Hexenyl Addition
6, Octenyl H-Abstraction
8, Shifted Octenyl H-Abstraction
18, Allyl H-Abstraction
19, Allyl Addition
20, Pentenyl H-Abstraction
21, Pentenyl Addition
22, Heptenyl H-Abstraction
23, Heptenyl Addition
24, Nonenyl H-Abstraction
26, Shifted Nonenyl H-Abstraction
10, Butyl H-Abstraction
11, Butyl Addition
12, Hexyl H-Abstraction
13, Hexyl Addition
14, Octyl H-Abstraction
16, Shifted Octyl H-Abstraction
28, Propyl H-Abstraction
29, Propyl Addition
30, Pentyl H-Abstraction
31, Pentyl Addition
32, Heptyl H-Abstraction
33, Heptyl Addition
34, Nonyl H-Abstraction
36, Shifted Nonyl H-Abstraction

b) 25 bar:

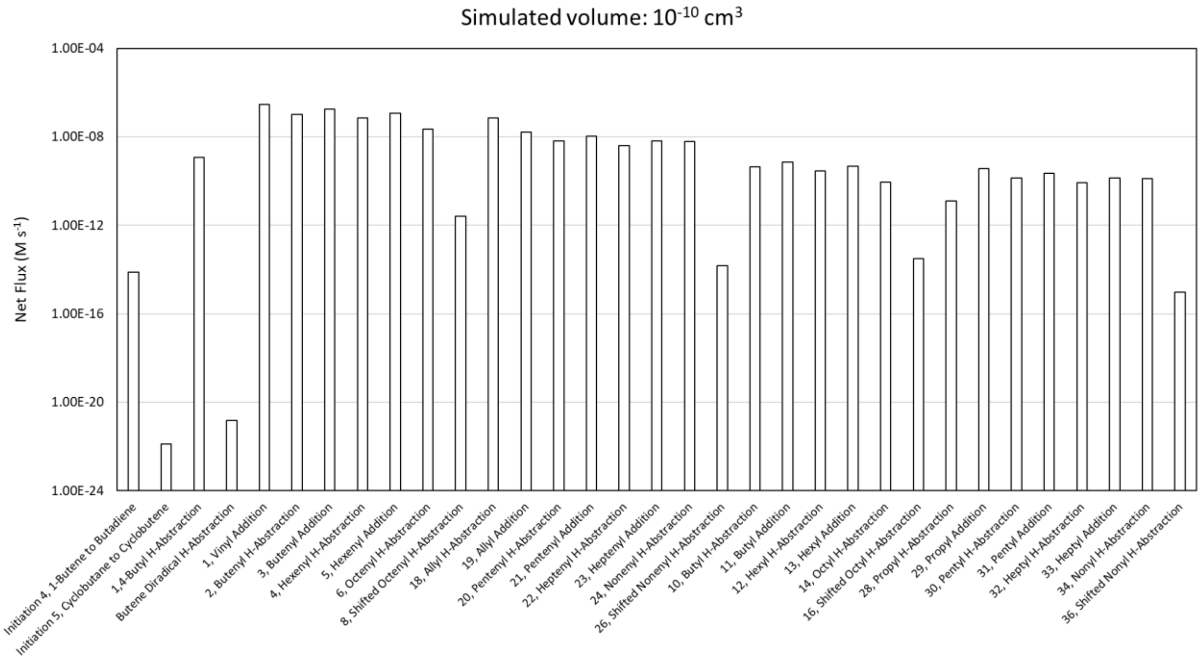
Simulated volume: 10^{-10} cm^3
Net Flux (M s^{-1})
1.00E-04
1.00E-08
1.00E-12
1.00E-16
1.00E-20
1.00E-24
Initiation 4, 1-Butene to Butadiene
Initiation 5, Cyclobutane to Cyclobutene
1,4-Butyl H-Abstraction
Butene Diradical H-Abstraction
1, Vinyl Addition
2, Butenyl H-Abstraction
3, Butenyl Addition
4, Hexenyl H-Abstraction
5, Hexenyl Addition
6, Octenyl H-Abstraction
8, Shifted Octenyl H-Abstraction
18, Allyl H-Abstraction
19, Allyl Addition
20, Pentenyl H-Abstraction
21, Pentenyl Addition
22, Heptenyl H-Abstraction
23, Heptenyl Addition
24, Nonenyl H-Abstraction
26, Shifted Nonenyl H-Abstraction
10, Butyl H-Abstraction
11, Butyl Addition
12, Hexyl H-Abstraction
13, Hexyl Addition
14, Octyl H-Abstraction
16, Shifted Octyl H-Abstraction
28, Propyl H-Abstraction
29, Propyl Addition
30, Pentyl H-Abstraction
31, Pentyl Addition
32, Heptyl H-Abstraction
33, Heptyl Addition
34, Nonyl H-Abstraction
36, Shifted Nonyl H-Abstraction

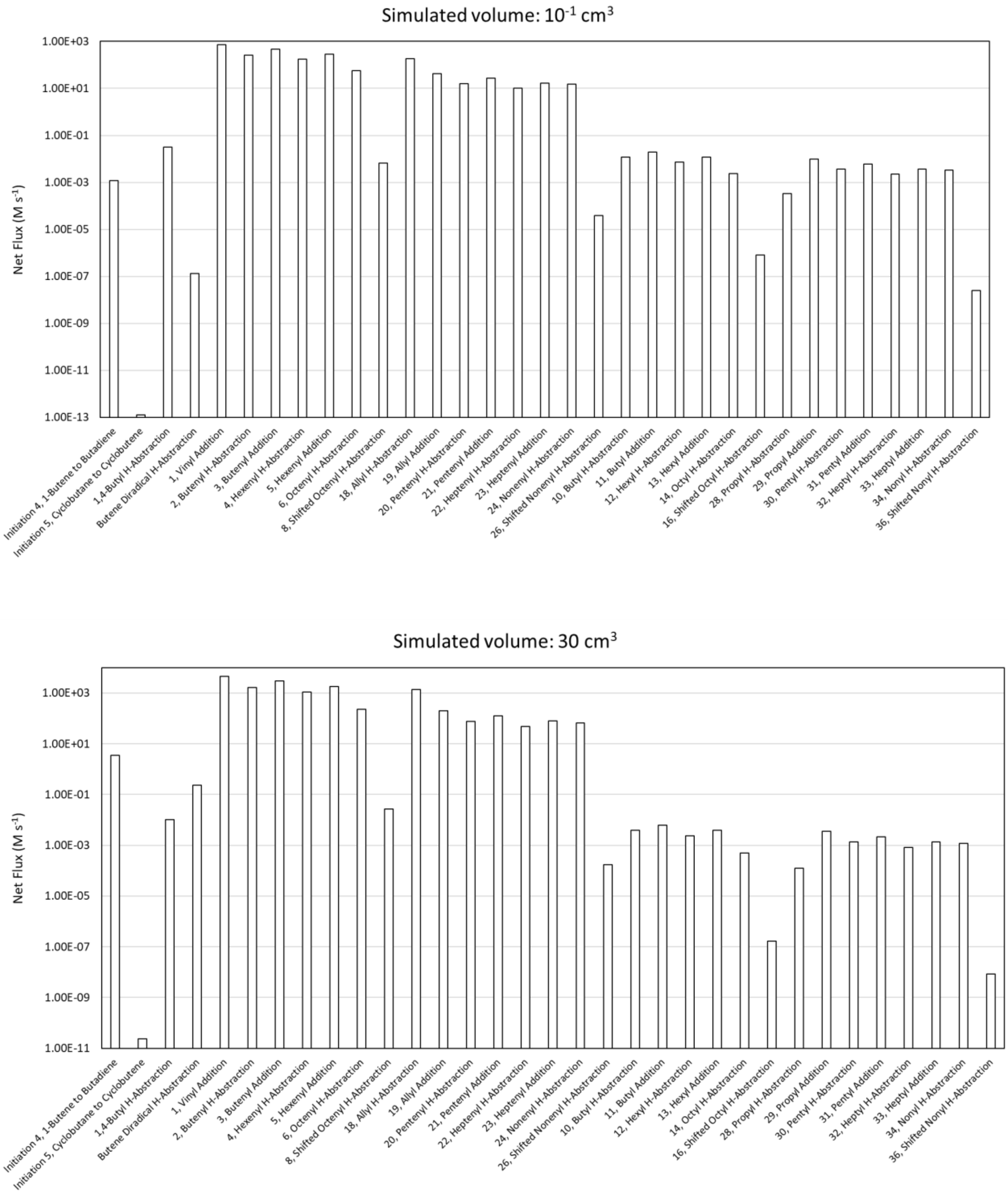

Figure 3.8: Net rates of all reactions in which ethylene is consumed. Reactions are labeled according to Figures 3.2-3.5. a) Net flux snapshots taken from a PFR simulated at 15 bar. b) Net flux snapshots taken from a PFR simulated at 25 bar.

3.4.3.2. Initiation Flux Comparison

As seen in Figure 3.2, there are distinct initiation routes that both ultimately lead to a vinyl radical. One comes from the 1,4-butyl diradical, while the other comes from the butene diradical. For the latter case, it emanates from the reaction of 1-butene with ethylene in a concerted step to form 1,3-butadiene. In the early stages of the reactor, 1-butene is formed via the initiation route shown in Figure 3.2. However, 1-butene is also the product of a propagation cycle, and thus, one would expect the preponderance of the butene diradical pathway to increase as a function of conversion. To illustrate this, additional snapshots of the rates of these two reactions as a function of reactor volume are shown in Figure 3.9. For the 15 bar case, in the latter two-thirds of the reactor, hydrogen abstraction from ethylene by butene diradical increases more significantly compared to hydrogen abstraction from ethylene by 1,4-butyl diradical as 1-butene is formed in meaningful quantities from propagation reactions. This trend is more notable in the 25 bar case, where conversion is over 50%. The rate of 1,4-butyl diradical hydrogen abstraction from ethylene exhibits a maximum followed by a decline while butene diradical hydrogen abstraction increases dramatically around 10^{-3} cm^3, with the formation of 1-butene driving a switch in the primary initiation mode seen at 10 cm^3 of simulated volume.

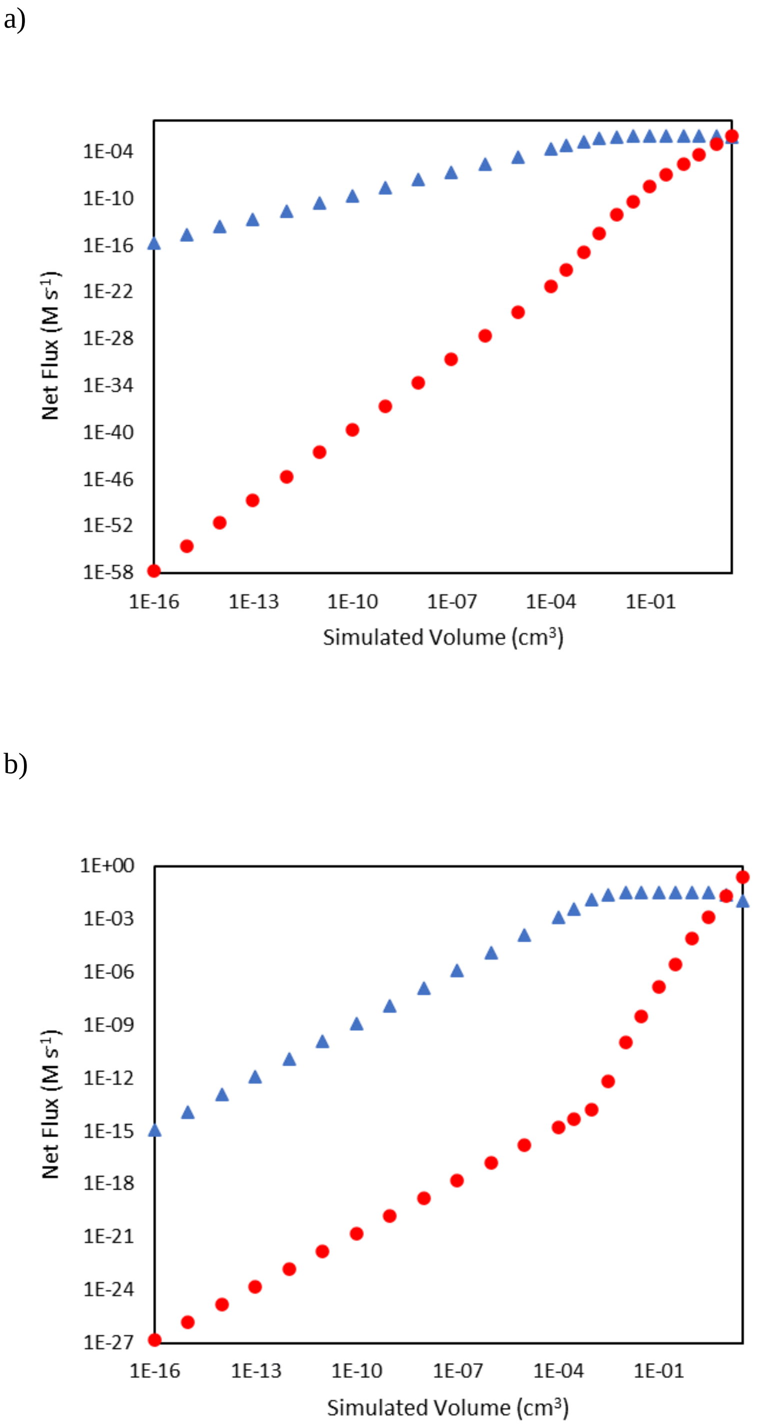

Figure 3.9: Comparison of rates of hydrogen abstraction from ethylene by 1,4-butyl diradical (blue ▲) and butene diradical (red ●) as a function of reactor volume. a) 15 bar isobaric PFR data. b) 25 bar isobaric PFR data.

3.4.3.3. Comparison of 1-Hexene Formation by β-scission

In the mechanism shown in Figure 3.1, 1-hexene can be formed as a result of β-scission of either nonyl or nonenyl, resulting in the reformation of propyl or allyl radical, respectively. Analysis of the trends in the fluxes of these two reactions gives insight into the dominance of the alkenyl radical chemistry (i.e., the right hand side of Figure 3.1) over the pathways carried by alkyl radicals (i.e., the left hand side of Figure 3.1) on the product distribution, e.g., the absence of propane as a major product in comparison to propene. Figure 3.10 shows that for the 15 bar case, nonyl β-scission dominates only at extremely low conversions and reactor volume, with a transition to nonenyl β-scission dominance above approximately 10^{-4} cm^3. Meanwhile, the 25 bar case, due to the higher conversion at low reactor volumes, has a higher rate of 1-hexene formation from nonenyl β-scission at all simulated volumes shown. The rates for both β-scission reactions taper as a function of reactor volume for both conditions as conversions rise, as increasing conversion reduces the concentration of ethylene available for the addition reactions key to forming larger radical species.

a)

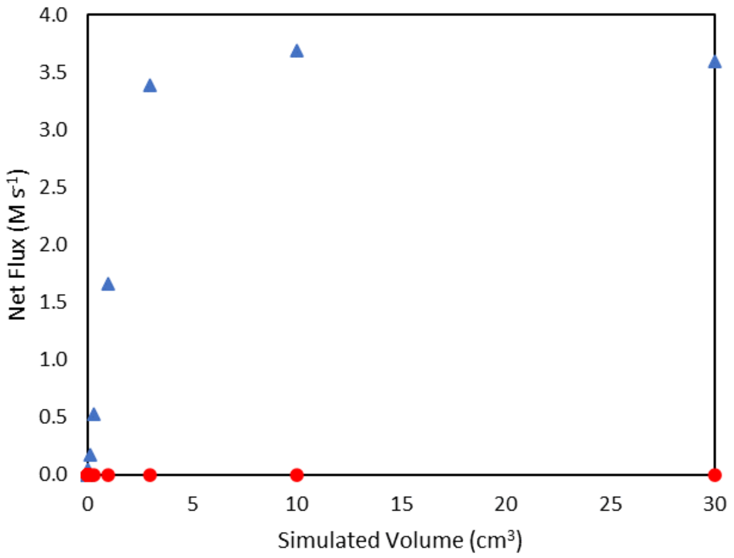

b)

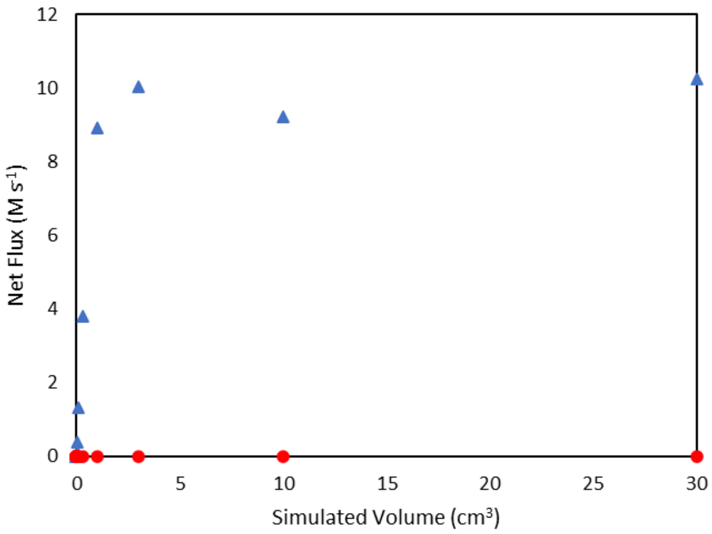

Figure 3.10: Linear comparisons of net flux of nonenyl β-scission (blue ▲) and nonyl β-scission (red ●) as a function of reactor volume. a) 15 bar isobaric PFR data. b) 25 bar isobaric PFR data.

3.4.3.4. C8 Branchpoint: Hydrogen Abstraction Versus β-scission

C_8 radical species have a major branchpoint that controls the formation of odd-numbered carbons, as seen in Figure 3.1. They can either undergo hydrogen abstraction, propagating vinyl radical while forming C_8 alkane and alkene species, or they can undergo β-scission to form a C_5 product and C_3 radicals, kicking off odd-carbon formation. Figure 3.11 demonstrates how these reactions compete as a function of reactor volume. At 15 bar, the ratio of the total net rate of hydrogen abstraction by either octenyl or octyl radicals to the net rate of the same radical reacting via β-scission starts out greater than 1, but as ethene is consumed, the ratio transitions to less than 1. At 25 bar, this same transition is not evident at the reactor volumes (and thus conversion values) tallied, as β-scission has a higher net rate over all simulated volumes. The net rates of both pathways decrease at higher volumes as higher conversion values are reached, reducing the concentration of ethylene available for necessary addition reactions to generate C_8 radicals.

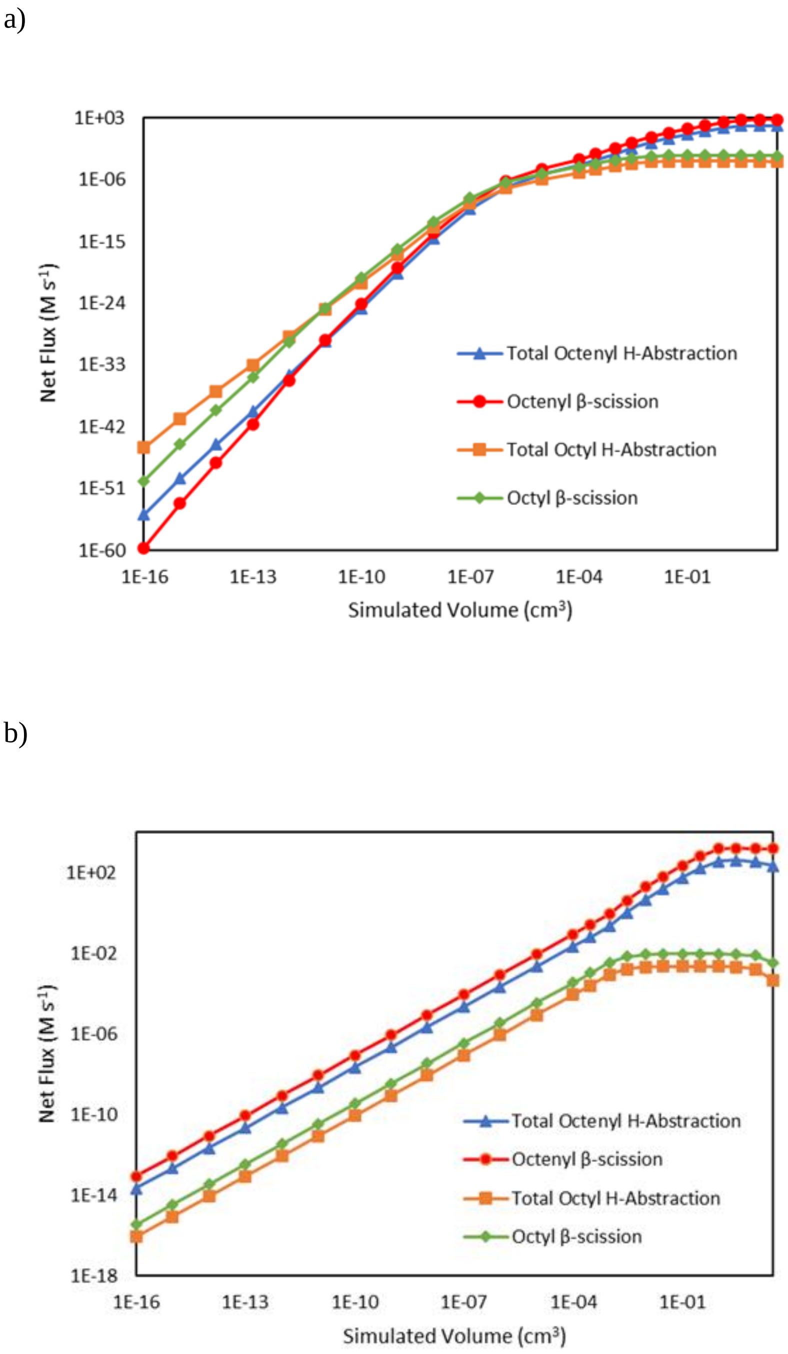

Figure 3.11: Log-log comparisons of C_8 hydrogen abstraction and β-scission reactions, including octenyl hydrogen abstraction (blue ▲), octenyl β-scission (red ●), octyl hydrogen abstraction (orange ■), and octyl β-scission (green ◆). Lines drawn on log-log plots are to guide the eye, with markers indicating simulated output points. a) 15 bar isobaric PFR data. b) 25 bar isobaric PFR data.

3.4.4. Sensitivity Analysis

Sensitivity analysis was conducted for each reaction type for which parameters were optimized as listed in Table 3.2 by solving the microkinetic model with each activation energy varied by ±1 kcal/mol from its optimized value and evaluating the impact on final results as shown in Figures 3.12 through 3.19.

Addition

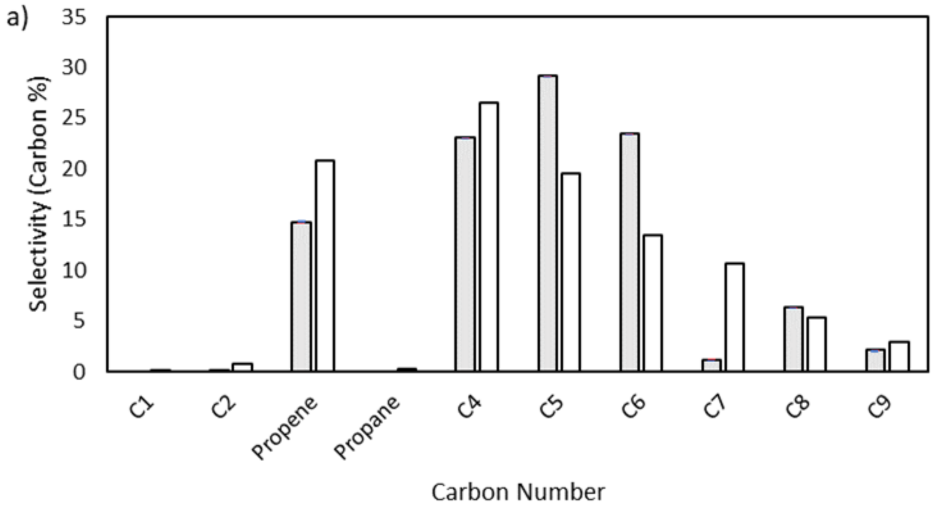
a)
Selectivity (Carbon %)
35
30
25
20
15
10
5
0
C1
C2
Propene
Propane
C4
C5
C6
C7
C8
C9
Carbon Number

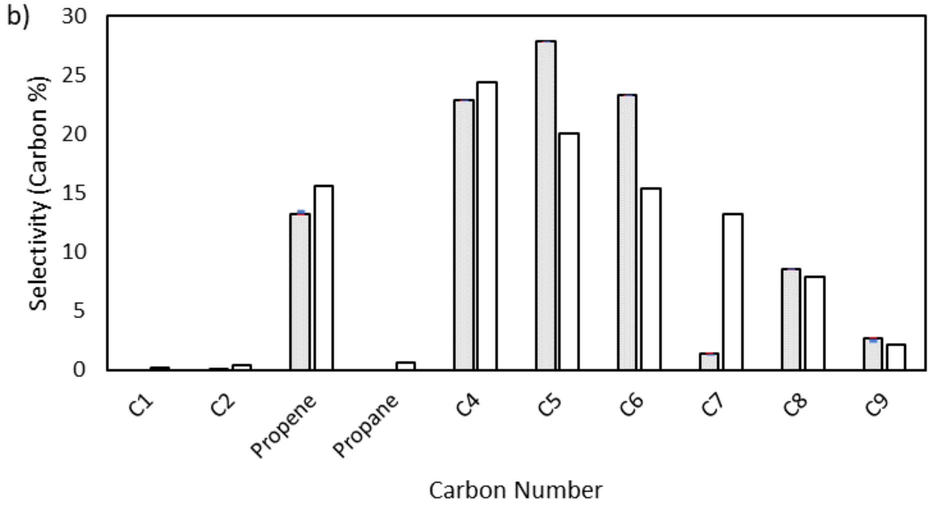
b)
Selectivity (Carbon %)
30
25
20
15
10
5
0
C1
C2
Propene
Propane
C4
C5
C6
C7
C8
C9
Carbon Number

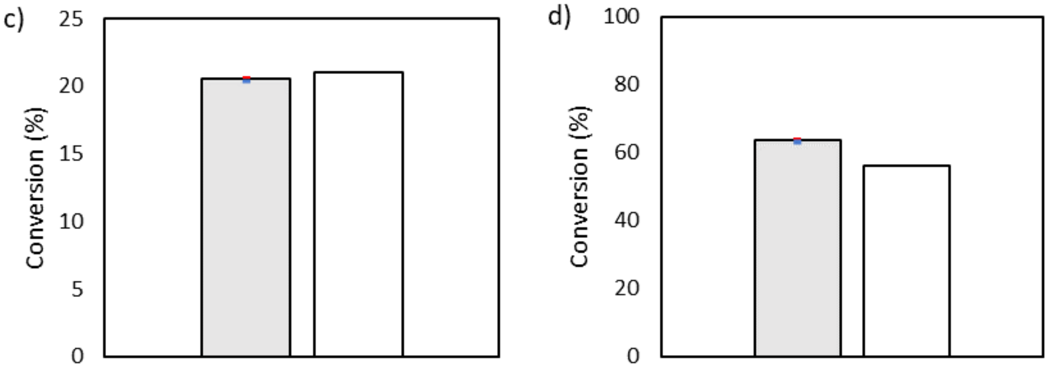

Figure 3.12: Sensitivity analysis of the impact of varying the basis activation energy of addition reactions by ±1 kcal/mol. The shaded bars are the model results based on the optimized parameters in Table 3.2, and the sensitivity to changes in the activation energy are denoted by colored error bars. The blue error bar indicates the change resulting from increasing the basis activation energy by 1 kcal/mol, whereas the red error bar indicates the change resulting from decreasing the basis activation energy by 1 kcal/mol. a) 15 bar isobaric PFR selectivity. b) 25 bar isobaric PFR selectivity. c) 15 bar isobaric PFR conversion. d) 25 bar isobaric PFR conversion.

Interestingly, the model is not sensitive to changes to the basis activation energy of addition, which at first may seem unexpected for a propagation reaction. As can be seen in Table 3.3, the enthalpy for reaction of addition is strongly exothermic, and as a result, the activation energy calculated through the Evans-Polanyi approach is truncated to zero within the model. Thus, changes of ±1 kcal/mol in the basis activation energy of addition may not be reflected in changes of ±1 kcal/mol for the activation energy of a specific addition reaction within the microkinetic model.

Table 3.3: Heats of reaction used for the Evans-Polanyi approach within the microkinetic model.

Reaction Label	**ΔH_{rxn} (kcal/mol)**
1,4 Butyl H-Abstraction	25.0
Butene Diradical H-Abstraction	28.0
1, Vinyl Addition	-25.7
2, Butenyl H-Abstraction	1.8
3, Butenyl Addition	-21.6
4, Hexenyl H-Abstraction	1.6
5, Hexenyl Addition	-21.8
8, Shifted Octenyl H-Abstraction	4.7
18, Allyl H-Abstraction	16.5
19, Allyl Addition	-6.6
26, Shifted Nonenyl H-Abstraction	4.7
28, Propyl H-Abstraction	10.0
β-scission reactions	7.6
Other addition reactions	-21.8
Other hydrogen abstraction reactions	1.6

Hydrogen Abstraction

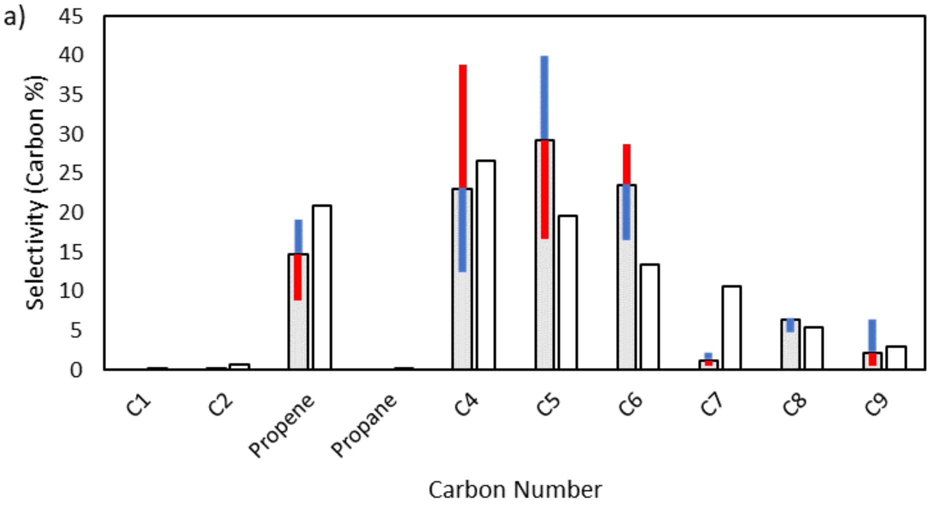

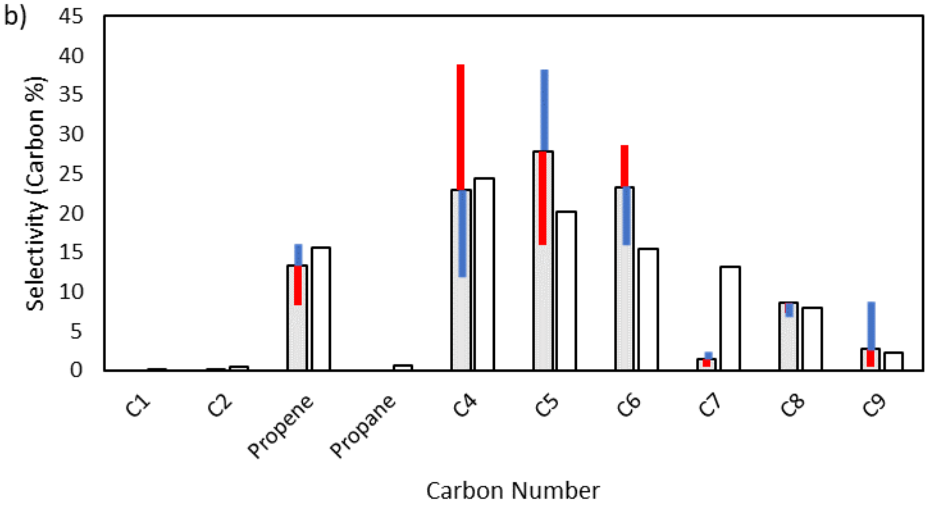

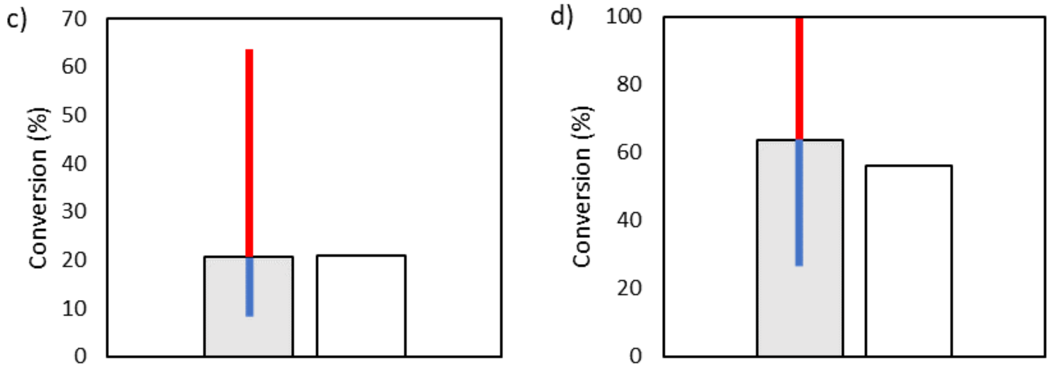

Figure 3.13: Sensitivity analysis of the impact of varying the basis activation energy of hydrogen abstraction reactions by ±1 kcal/mol. The shaded bars are the model results based on the optimized parameters in Table 3.2, and the sensitivity to changes in the activation energy are denoted by colored error bars. The blue error bar indicates the change resulting from increasing the basis activation energy by 1 kcal/mol, whereas the red error bar indicates the change resulting from decreasing the basis activation energy by 1 kcal/mol. a) 15 bar isobaric PFR selectivity. b) 25 bar isobaric PFR selectivity. c) 15 bar isobaric PFR conversion. d) 25 bar isobaric PFR conversion.

Given its key role in the propagation cycle that leads to a long kinetic chain, both the conversion and the product distribution are highly sensitive to the activation energy for hydrogen abstraction, with only a -1 kcal/mol change resulting in nearly full conversion for the 25 bar case. Hydrogen abstraction is not only one of the primary propagation steps, but it is a key reaction in the initiation cascade that leads to the creation of vinyl radical. Additionally, hydrogen abstraction competes directly with β-scission to form odd-numbered carbon species, providing control over the product selectivity profile as well.

Recombination

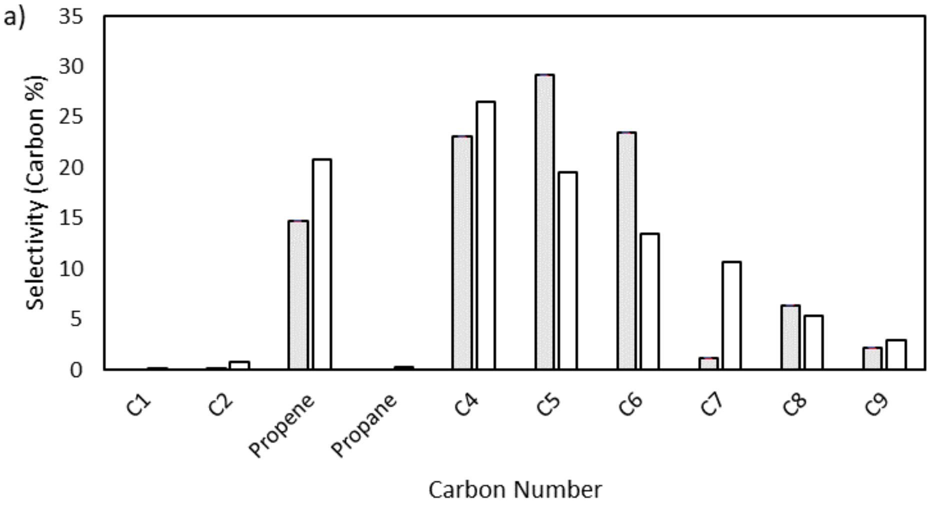

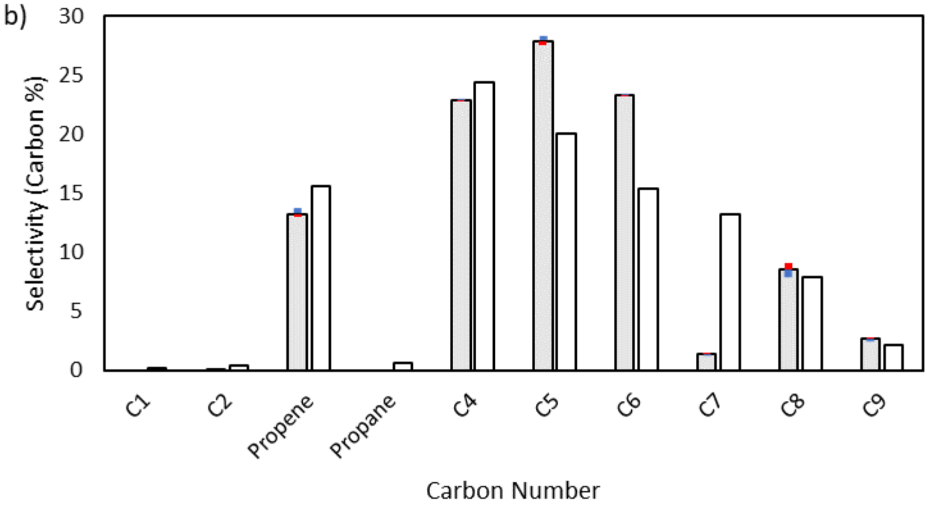

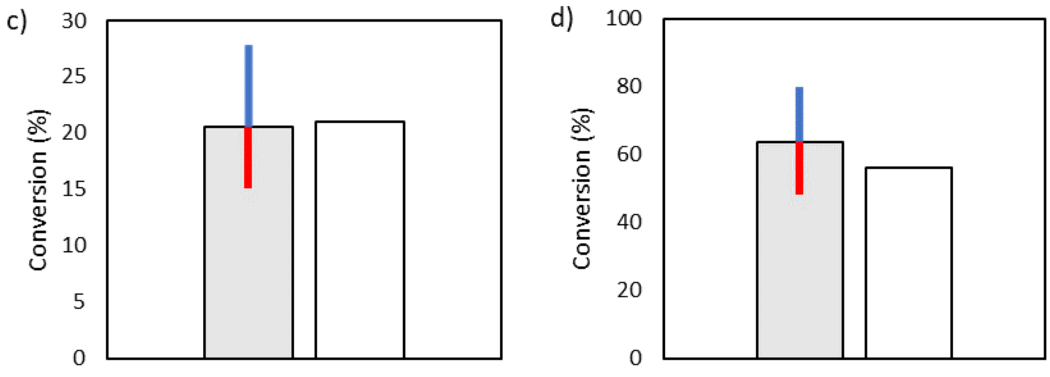

Figure 3.14: Sensitivity analysis of the impact of varying the basis activation energy of recombination reactions by ±1 kcal/mol. The shaded bars are the model results based on the optimized parameters in Table 3.2, and the sensitivity to changes in the activation energy are denoted by colored error bars. The blue error bar indicates the change resulting from increasing the basis activation energy by 1 kcal/mol, whereas the red error bar indicates the change resulting from decreasing the basis activation energy by 1 kcal/mol. a) 15 bar isobaric PFR selectivity. b) 25 bar isobaric PFR selectivity. c) 15 bar isobaric PFR conversion. d) 25 bar isobaric PFR conversion.

As anticipated, changing the activation energy for recombination does not have major influence on the product distribution, but as a key determinant of the length of the kinetic chain, it does have a measurable influence over conversion, as it effectively controls the lifetime of radicals that are produced. Longer radical lifetimes as the activation energy for recombination is increased, thereby decreasing the rate coefficient, results in a longer kinetic chain with a higher rate of propagation, thereby increasing conversion.

1,4 Hydrogen Shift

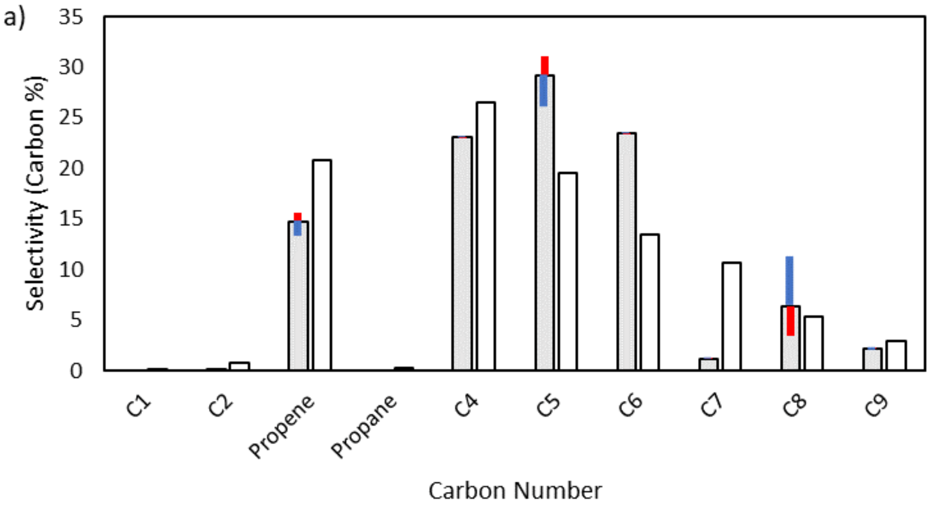

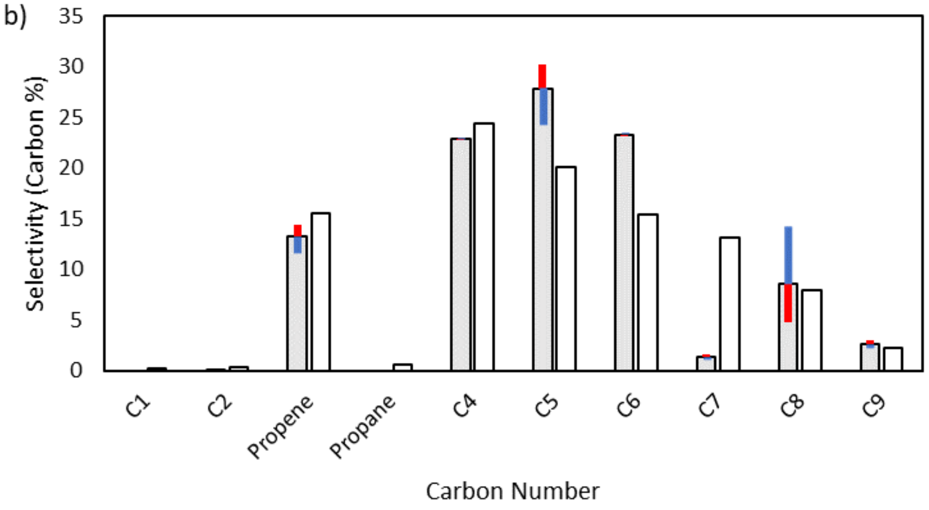

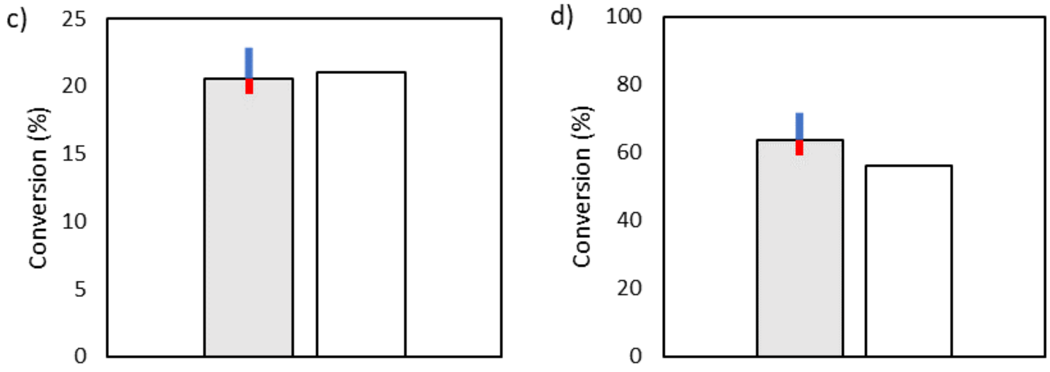

Figure 3.15: Sensitivity analysis of the impact of varying the activation energy of 1,4 hydrogen shift reactions by ±1 kcal/mol. The shaded bars are the model results based on the optimized parameters in Table 3.2, and the sensitivity to changes in the activation energy are denoted by colored error bars. The blue error bar indicates the change resulting from increasing the basis activation energy by 1 kcal/mol, whereas the red error bar indicates the change resulting from decreasing the basis activation energy by 1 kcal/mol. a) 15 bar isobaric PFR selectivity. b) 25 bar isobaric PFR selectivity. c) 15 bar isobaric PFR conversion. d) 25 bar isobaric PFR conversion.

Both octyl and octenyl radicals can participate in 1,4-hydrogen shift reactions and are one of the key enablers of the production of odd-numbered carbon species. As such, they have little influence over C_4 and C_6, but they have a significant effect on the fate of C_8 radical species as well as odd-numbered carbon species.

1,5 Hydrogen Shift

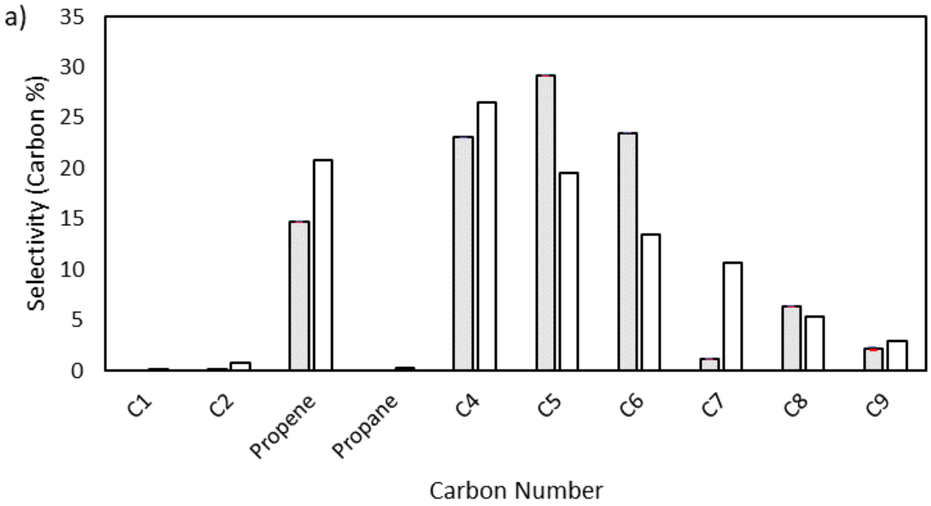

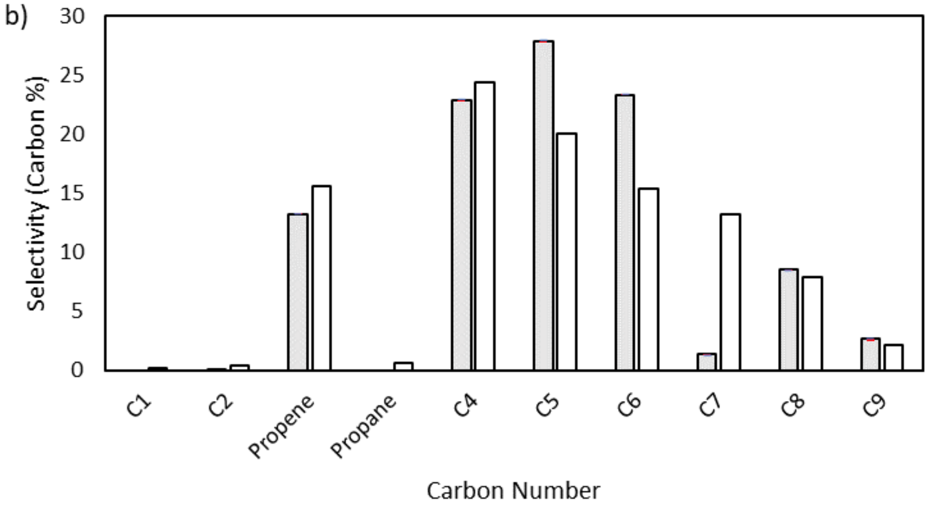

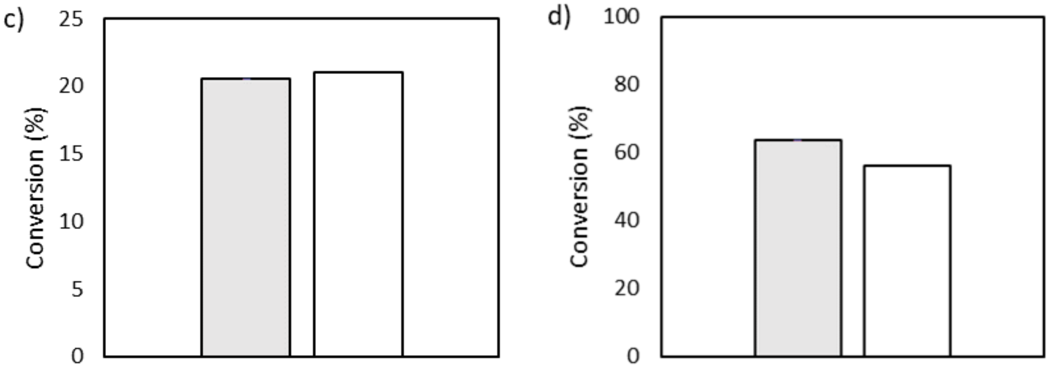

Figure 3.16: Sensitivity analysis of the impact of varying the activation energy of 1,5 hydrogen shift reactions by ±1 kcal/mol. The shaded bars are the model results based on the optimized parameters in Table 3.2, and the sensitivity to changes in the activation energy are denoted by colored error bars. The blue error bar indicates the change resulting from increasing the basis activation energy by 1 kcal/mol, whereas the red error bar indicates the change resulting from decreasing the basis activation energy by 1 kcal/mol. a) 15 bar isobaric PFR selectivity. b) 25 bar isobaric PFR selectivity. c) 15 bar isobaric PFR conversion. d) 25 bar isobaric PFR conversion.

The sensitivity of the model results to the activation energy for 1,5-hydrogen shift is less pronounced than that to the activation energy of 1,4-hydrogen shift. As formulated in the model, 1,5-hydrogen shift reactions only allow for nonenyl, nonyl, and octyl radicals as reactants, thereby impacting the subsequent β-scission reactions of the radicals that are formed as products of 1,5-hydrogen shift. However, 1,5-hydrogen shift was not implemented for octenyl radical, as it was assumed to lead to a species that resulted in futile reaction pathways. Specifically, the formation of the 1-octenyl-4-radical would result in a diene for β-scission in one direction, and dienes were not observed in the product distribution. Note that no radicals that were generated were allowed to lead to dienes through propagation steps, although butadiene was a species in one of the initiation pathways. In the other direction, vinyl radical would be formed, and given its relative stability, the heat of reaction, and thus the E_a value for this reaction channel, would be high, leading to low rates. Thus, it was simply excluded from this compact model. In adjusting the activation energy for 1,5-hydrogen shift, there is a small effect on the C_9 selectivity, but overall, 1,4-hydrogen shift, despite its less favorable kinetics than 1,5-hydrogen shift, guides the formation of odd-number carbon species through the octenyl β-scission pathway in this truncated reaction network.

Initiation Label 3

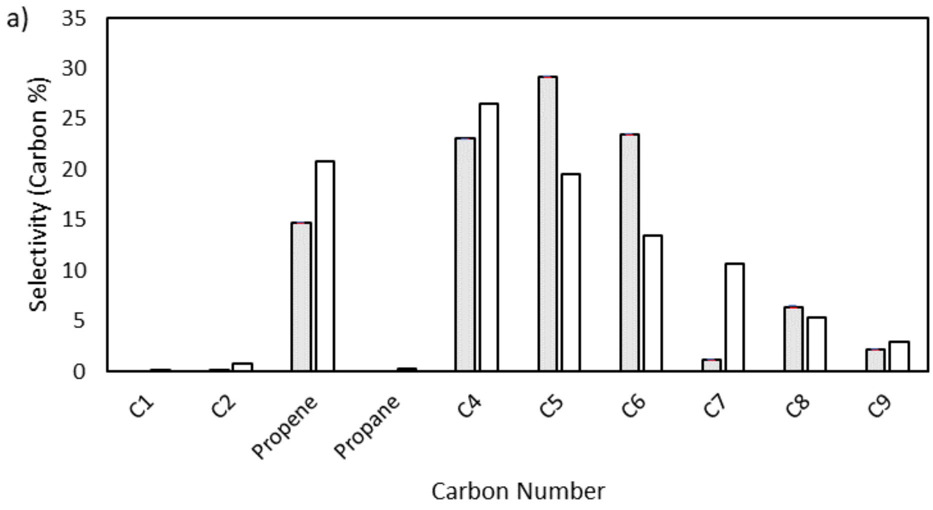

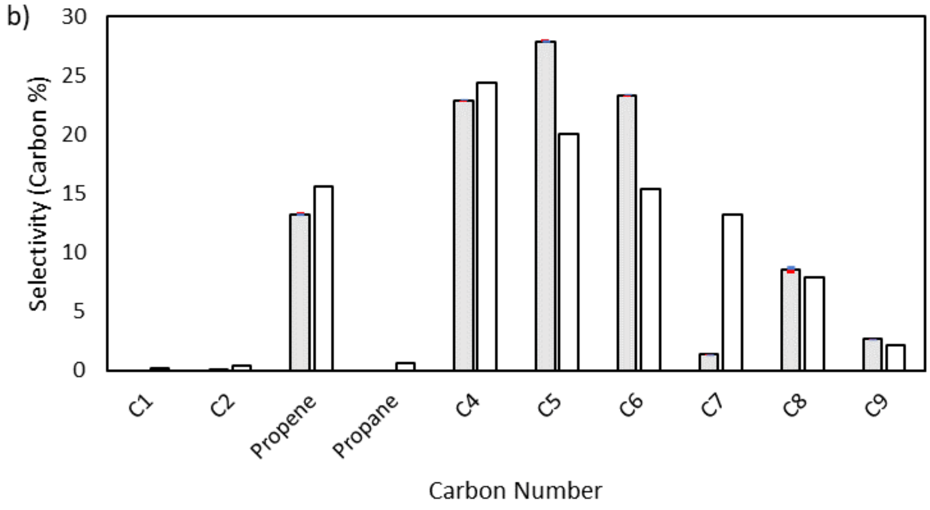

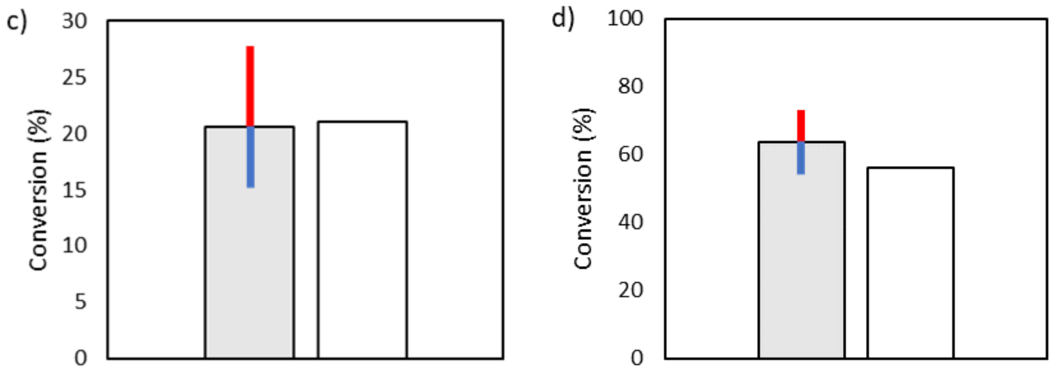

Figure 3.17: Sensitivity analysis of the impact of varying the activation energy of the *Initiation Label 3* reaction, the direct formation of 1,4-butyl diradical from two ethylene molecules, by ±1 kcal/mol. The shaded bars are the model results based on the optimized parameters in Table 3.2, and the sensitivity to changes in the activation energy are denoted by colored error bars. The blue error bar indicates the change resulting from increasing the basis activation energy by 1 kcal/mol, whereas the red error bar indicates the change resulting from decreasing the basis activation energy by 1 kcal/mol. a) 15 bar isobaric PFR selectivity. b) 25 bar isobaric PFR selectivity. c) 15 bar isobaric PFR conversion. d) 25 bar isobaric PFR conversion.

Initiation Label 4

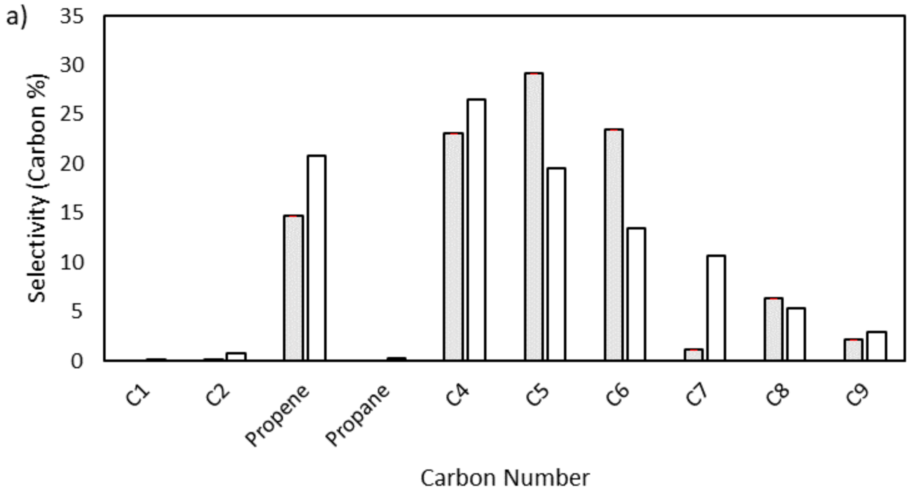

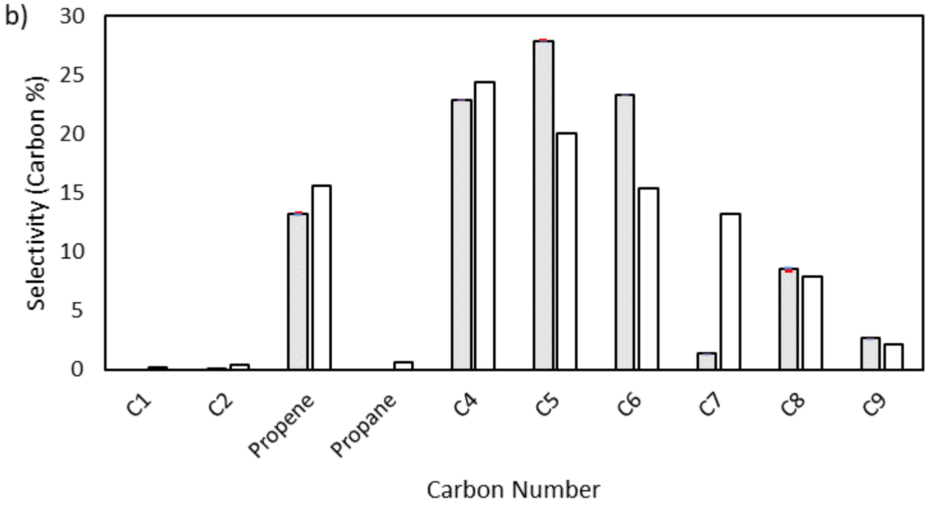

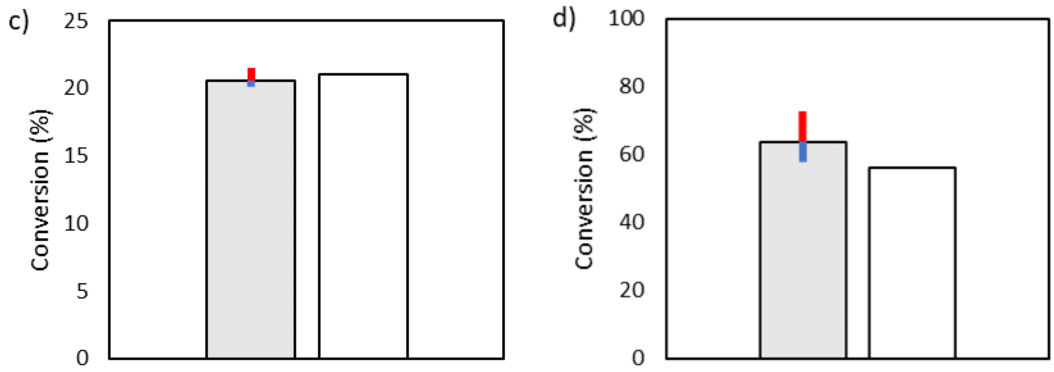

Figure 3.18: Sensitivity analysis of the impact of varying the activation energy of the *Initiation Label 4* reaction, the conversion of 1-butene to butadiene, by ±1 kcal/mol. The shaded bars are the model results based on the optimized parameters in Table 3.2, and the sensitivity to changes in the activation energy are denoted by colored error bars. The blue error bar indicates the change resulting from increasing the basis activation energy by 1 kcal/mol, whereas the red error bar indicates the change resulting from decreasing the basis activation energy by 1 kcal/mol. a) 15 bar isobaric PFR selectivity. b) 25 bar isobaric PFR selectivity. c) 15 bar isobaric PFR conversion. d) 25 bar isobaric PFR conversion.

Initiation Label 6

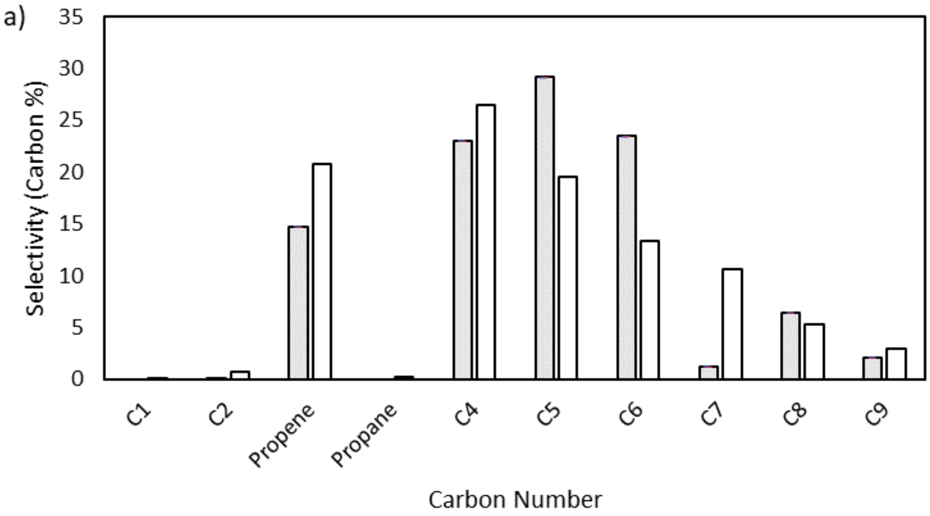

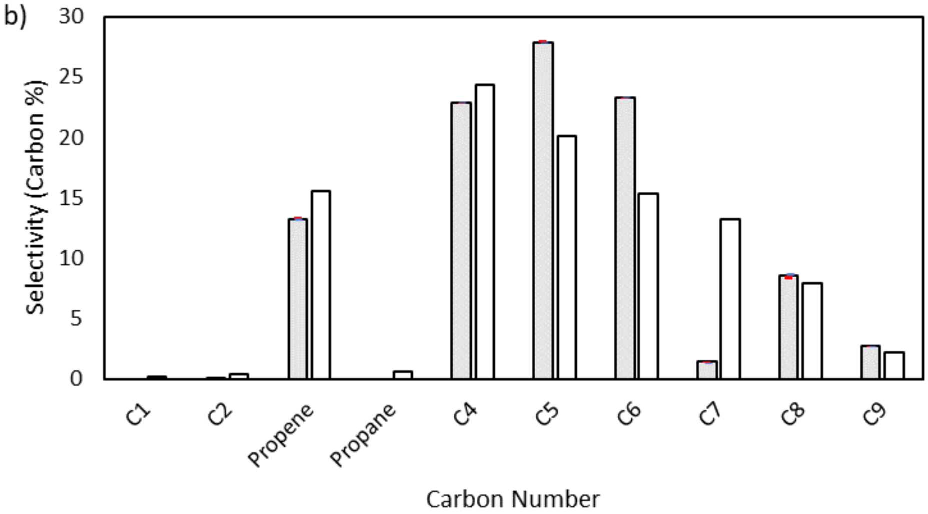

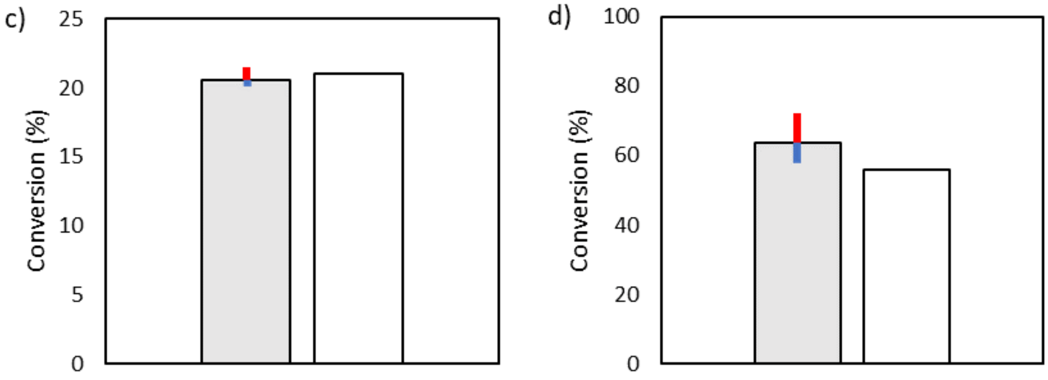

Figure 3.19: Sensitivity analysis of the impact of varying the activation energy of the *Initiation Label 6* reaction, the conversion of butadiene to a resonance-stabilized diradical, by ±1 kcal/mol. The shaded bars are the model results based on the optimized parameters in Table 3.2, and the sensitivity to changes in the activation energy are denoted by colored error bars. The blue error bar indicates the change resulting from increasing the basis activation energy by 1 kcal/mol, whereas the red error bar indicates the change resulting from decreasing the basis activation energy by 1 kcal/mol. a) 15 bar isobaric PFR selectivity. b) 25 bar isobaric PFR selectivity. c) 15 bar isobaric PFR conversion. d) 25 bar isobaric PFR conversion.

While the initiation reactions do not affect the product distribution, they have significant control over conversion, as expected due to the generation of the vinyl and butyl radicals key to consuming ethylene. From textbook Rice-Herzfeld kinetics, the rate of consumption of the substrate is increased as the rate coefficient for initiation is increased, which is what is observed here; as the activation energy for any of the initiation reactions is decreased, thereby increasing the rate coefficient for initiation, conversion is increased. Additionally, the *Initiation Label 4* reaction drives conversion forward once significant quantities of 1-butene have produced within the system, which also impacts the formation of vinyl radical through the formation of a resonance-stabilized diradical in the *Initiation Label 6* reaction.

3.5. Conclusions

In this work, a DFT-parameterized microkinetic model of the thermal oligomerization of ethylene was developed. The odd-numbered carbon species in the product distribution were identified to originate from β-scission of C_8 mid-radicals that were created from hydrogen shift reactions. The significant production of linear terminal olefins is driven by consecutive radical addition reactions involving terminal 1-alkenyl radicals and ethylene, balanced by hydrogen abstraction from ethylene due to its high concentration to create the linear alpha olefin products and additional vinyl radicals that can grow again. Flux analysis identified that initiation occurs primarily through hydrogen abstraction by 1,4-butyl diradical at low conversion, and as conversion increases, the primary initiation mode switches to hydrogen abstraction by the butene diradical as 1-butene begins to be produced in significant quantities. The insights from this work can aid in the development of intensified reactor systems for the direct valorization of ethane streams from shale gas production, allowing large waste streams to be converted into usable fuel products.

Chapter 4: Evaluating the Impact of T-Site Location in the Conversion of Methanol to Dimethyl Ether within MFI Zeolites through Microkinetic Modeling

Material in this chapter is based on collaborative work from Grant Marsden, Pavlo Kostetskyy, Ryoh-Suke Sekiya, Alexander Hoffman, Songhyun Lee, Rajamani Gounder, David Hibbitts, and Linda J. Broadbelt.

4.1. Abstract

Within zeolites, T-site location is a major factor for determining catalytic activity. The 12 crystallographically unique T-sites of orthorhombic MFI demonstrate significant differences that are difficult to resolve experimentally. A DFT-parameterized microkinetic model is presented that is able to capture with fine resolution the effects of each independent T-site of MFI on a test reaction of methanol dehydration to dimethyl ether. Flux analysis, surface speciation analysis, and degree of rate control analysis are used to identify that methanol tetramers are the key intermediate for the production of DME over MFI. T4, T6, T7, and T12 were identified as dominant sites to catalytically promote this reaction, matching with the lower activation barriers for the tetramer mechanism on these sites. The technique developed through this work expands the existing framework for evaluating paired sites in zeolites, creating a holistic technique able to capture both location and proximity effects, enabling rational design of next-generation catalytic materials.

4.2. Introduction

Zeolites are well-ordered microporous aluminosilicates that have industrially relevant catalytic properties.[21, 22] Brønsted acidic zeolites in particular are used for reactions critical to the energy transition, such as cracking and oligomerization.[116-127] In particular, the zeolite ZSM-5, also known as MFI, has significant industrial relevance, defining a large section of the multi-billion-dollar synthetic zeolite market.[128] The orthorhombic form of this zeolite has 12 crystallographically unique locations where an acid site can exist, known as a T-site.[129] These 12 unique T-sites demonstrate significant differences in binding energy and stability,[130] and they display catalytic differences due to confinement effects and differences in the stabilization of reaction intermediates and transition states due to van der Waals interactions.[131]

A number of experimental techniques have been historically applied to attempt to resolve T-site distributions. ^{27}Al magic angle spinning nuclear magnetic resonance (MAS NMR) is able to assign resonances to different T-site locations, but it lacks fine resolution due to peak broadening from the quadrupolar interaction at the Al atom.[131, 132] X-ray absorption near edge structure and extended x-ray absorption fine structure have been used in conjunction with ^{27}Al MAS NMR, as well as density functional theory (DFT) and molecular dynamics simulations, to group together similar T-sites in Beta zeolite.[133] Standing x-ray fluorescence spectroscopy has been used to distinguish between two different T-sites within scolecite,[134] and x-ray emission spectroscopy has been paired with theoretical spectra to identify T-site occupation in ferrierite zeolite.[135] Atom probe tomography has been used to identify pathways for Al transport in steamed zeolites.[136] Finally, test reactions sensitive to confinement effects, such as cracking rate comparisons to define a constraint index,[131, 137] have been applied to measure the average size of pores around acid sites. Methanol dehydration to dimethyl ether (DME) is one other such test reaction, seen to be sensitive to confining environments and acid strength.[131, 138]

Previous work developed a method to evaluate the effect of proximity of acid sites in chabazite,[20] a zeolite with only a single crystallographically unique T-site. There is the need to expand this methodology to evaluate the effects of not just proximity, but also location, enabling fine resolution of T-site importance within any class of zeolite. Using methanol dehydration as a test reaction to develop this n-dimensional technique, a DFT-parameterized microkinetic model of methanol dehydration over all 12 independent T-sites in orthorhombic MFI is reported in this chapter. The technique presented in this work expands the platform to predictively model the impact of industrially relevant catalytic properties on the process scale from atomic scale knowledge, enabling the rational design of next-generation catalytic materials.

4.3. Microkinetic Modeling Methods

The microkinetic model was constructed by defining the rate of each elementary step in the reaction mechanism on a basis site type, taken here as the T1 site of MFI:

$$r_{i,site1} = A_i \exp\left(\frac{-E_{a,i}}{RT}\right) \prod_{j}^{reactants} C_j \tag{4.1}$$

Where $r_{i,site1}$ is the rate of the ith elementary step over the basis T1 site, A_i is the pre-exponential factor, $E_{a,i}$ is the activation energy, R is the universal gas constant, T is the reactor temperature, and C_j is either the partial pressure for gas species or fractional coverage for surface species.

To define the rates of elementary reaction steps over other sites within MFI, a scaling factor based on the distribution of site types is applied:

$$r_{i,siteX} = \frac{n_x}{n_1} A_i \exp\left(\frac{-E_{a,i}}{RT}\right) \prod_{j}^{reactants} C_j \tag{4.2}$$

Where n_x is the number of sites of type TX, and n_1 is the number of basis sites T1 present in the system. Next, the set of ordinary differential equations to cover all surface species coverages and gas-phase species is constructed, using T1 sites as a consistent basis for integration:

$$\frac{dC_j}{dn_1} = \sum_i \nu_{i,j} r_i \tag{4.3}$$

Where $\nu_{i,j}$ is the stoichiometric number for species j in elementary reaction step i. Combining this ordinary differential equation set with a surface species balance and the plug flow reactor design equation allows the microkinetic model to reflect experimental conditions. The rate of dimethyl ether (DME) formation was evaluated at the outlet of the reactor, where differential conversion (<0.1%) was confirmed to match with experimental data. Surface coverages and reaction fluxes were also evaluated at the reactor outlet. To match with the experimental reactor, simulations were run with a total of 10^{19} active sites at a temperature of 415 K with methanol pressure varied from 0.1 to 41.13 kPa at an inlet flowrate of 0.615 mol/s. Uncertainty within DFT calculations was accounted for by tuning activation energies within the bounds of ±6 kJ/mol and pre-exponential factors within the bounds of ±1 order of magnitude.

4.4. Results and Discussion

4.4.1. Reaction Mechanism

The reaction mechanism for methanol dehydration within MFI was proposed to be equivalent to that of methanol dehydration within chabazite,[20] reproduced here as Scheme 4.1:

Scheme 4.1. Modeled Mechanism for Methanol Dehydration on MFI[20]

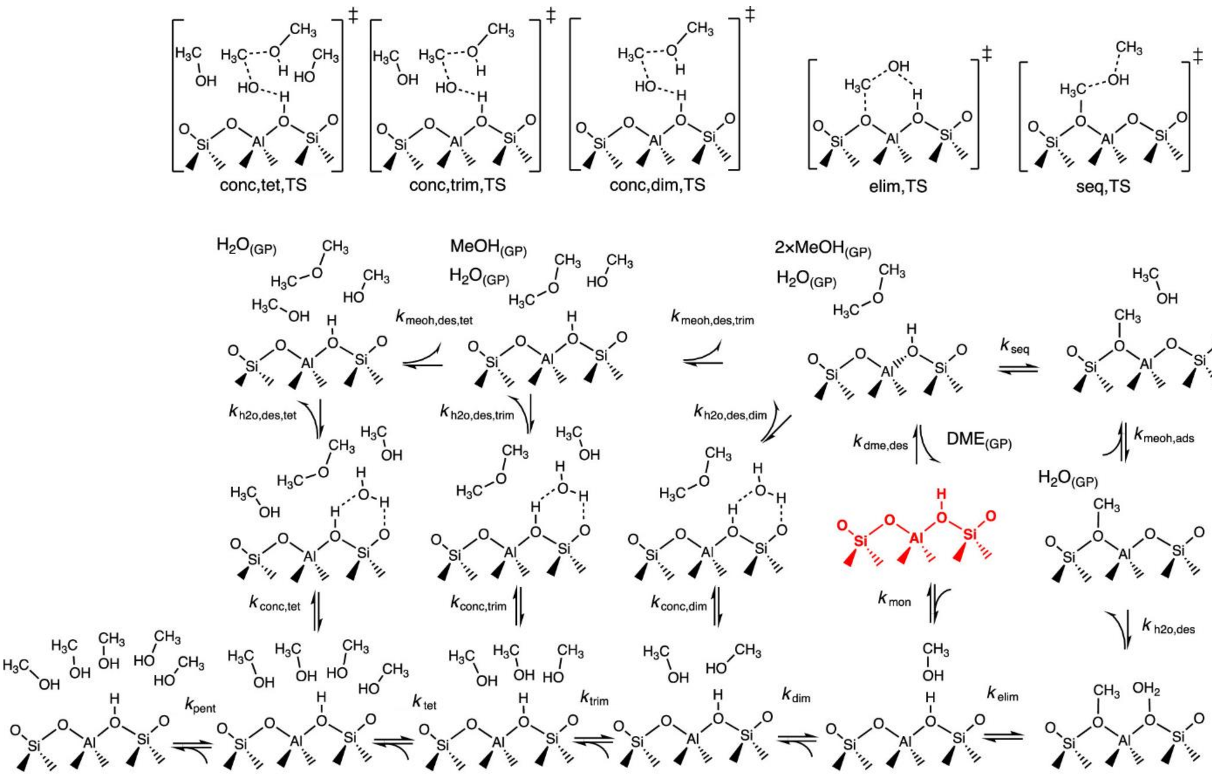

The reaction mechanism begins with a single methanol molecule adsorbing. There are two options for the adsorbed methanol monomer – it can either undergo elimination to form a bound methoxy species, or another methanol molecule can adsorb to form a coordinated methanol dimer. Should elimination occur, the mechanism progresses through water desorption, the adsorption of a second methanol molecule, and the direct formation of dimethyl ether from the bound methoxy species interacting with the adsorbed methanol molecule, ending in desorption of the bound dimethyl ether species. Alternatively, should a methanol dimer form on the site, then additional methanol molecules can adsorb to form trimers, tetramers, and pentamer species. Methanol dimers, trimers, and tetramers all have individual pathways to form bound dimethyl ether and water while leaving behind a representative amount of methanol species, whereas methanol pentamers are considered to be inhibiting species.

4.4.2. Microkinetic Modeling

The microkinetic model was parameterized using potential energy landscapes evaluated for all twelve unique T-sites within orthorhombic MFI. DFT data was collected for the formation of methanol clusters, the desorption of dimethyl ether, the desorption of water from an otherwise unoccupied site, the desorption of methanol from an otherwise unoccupied site, and the forward reaction of methanol clusters through tetramers forming bound dimethyl ether.

For reactions with DFT data unavailable, the overall enthalpy of reaction was set to match that of the overall reaction of methanol dehydration for thermodynamic consistency. Then, for the dimer and trimer cases, values for the enthalpy of unoccupied desorption of methanol and water were scaled by a factor of 0.55, whereas the entropy values were scaled by a factor of 0.95. For the more crowded tetramer case, enthalpies were scaled by a factor of 0.45 and entropies were scaled by a factor of 0.9025. As data for the sequential pathway was unavailable, values from the chabazite case were used.[20]

Rate coefficients were assumed to be of Arrhenius form, with an explicit pre-exponential factor and activation energy for each elementary step over each T-site evaluated individually. Adsorption events were assumed to be unactivated, and the activation energy of desorption events was taken as the enthalpy of adsorption. This led to the parameter set shown in Table S.1.

As described in Section 4.3., these values were adjusted using the experimental data as objective points within the bounds of ±6 kJ/mol for activation energies, disallowing negative activation energies, and

±1 order of magnitude for pre-exponential factors. Specifically, the pre-exponential factors of dimer, trimer, and tetramer formation were increased by 1 order of magnitude, the activation energies of their reverse reactions were increased by 6 kJ/mol, the pre-exponential factors of their reverse reactions were reduced to one quarter of their untuned values, and the pre-exponential factor of reverse pentamer formation was increased by 1 order of magnitude. These adjusted parameters are shown in Table B2 of the Appendix.

Despite the experimental techniques applied to attempt to fully resolve the distribution of T-sites within MFI, as described in the Introduction, the distribution of T-sites remains an unknown value.[139] Assuming an equal distribution of all T-sites leads to the microkinetic modeling output shown in Figure 4.1.

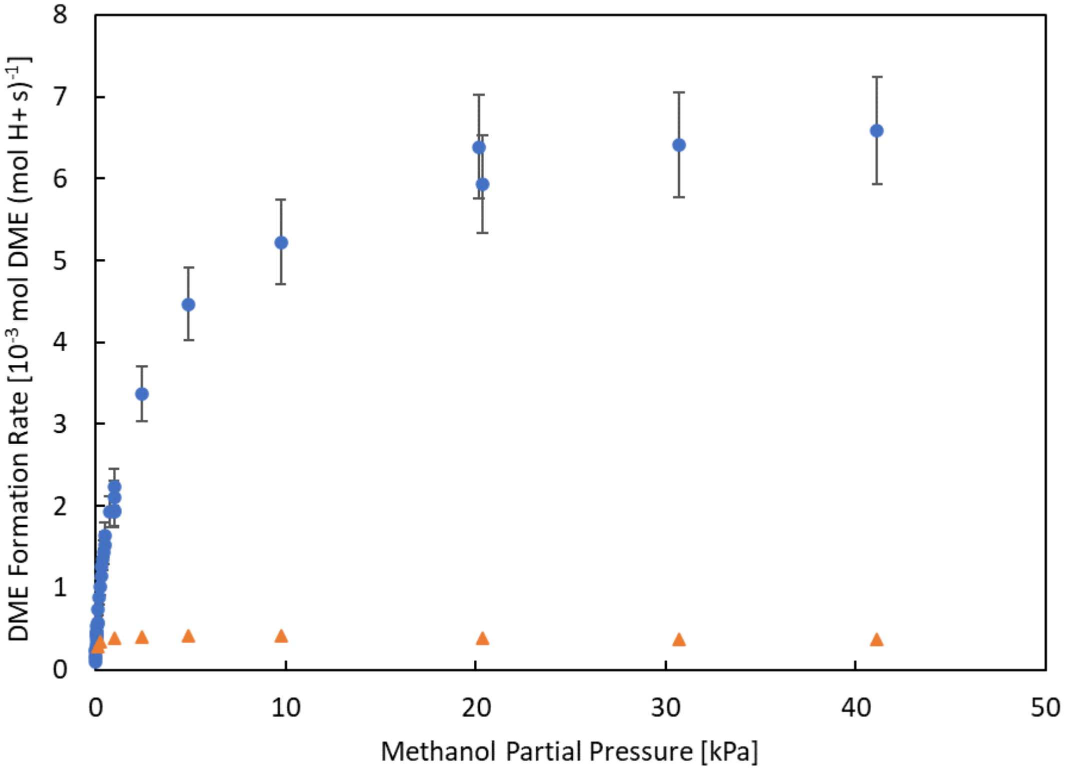

Figure 4.1: Microkinetic model output (orange ▲) of DME formation rates versus methanol partial pressure assuming a uniform distribution of T-sites, plotted against experimental data (blue ●).

Alternatively, a Boltzmann distribution of sites can be assumed by using the following equation:

$$\frac{n_x}{\sum_{i=1}^{12} n_i} \approx \frac{\exp\left(-\frac{E_x}{RT}\right)}{\sum_{i=1}^{12} \exp\left(-\frac{E_i}{RT}\right)} \tag{4.4}$$

Where T is the average temperature of synthesis conditions, assumed as 473 K, and E_x is a relevant formation energy for a site of type TX, taken here to be the relative aluminum exchange energies with a relative permittivity of 80.[139] This results in the site distribution shown in Table 4.1.

Table 4.1: Relative Boltzmann T-site Distribution

Site	**Relative Al Exchange Energies (kJ/mol)**[a,139]	**Fraction within Distribution**
T1	16	$1.36\cdot10^{-2}$
T2	13	$2.92\cdot10^{-2}$
T3	11	$4.85\cdot10^{-2}$
T4	18	$8.18\cdot10^{-3}$
T5	22	$2.96\cdot10^{-3}$
T6	28	$6.43\cdot10^{-4}$
T7	23	$2.29\cdot10^{-3}$
T8	14	$2.26\cdot10^{-2}$
T9	19	$6.34\cdot10^{-3}$
T10	18	$8.18\cdot10^{-3}$
T11	10	$6.25\cdot10^{-2}$
T12	0	$7.95\cdot10^{-1}$

[a]Energies evaluated at a relative permittivity of 80 with VASPsol.[139]

Using this distribution of T-sites rather than a uniform distribution results in the microkinetic modeling output shown in Figure 4.2, displaying excellent agreement across all pressure ranges.

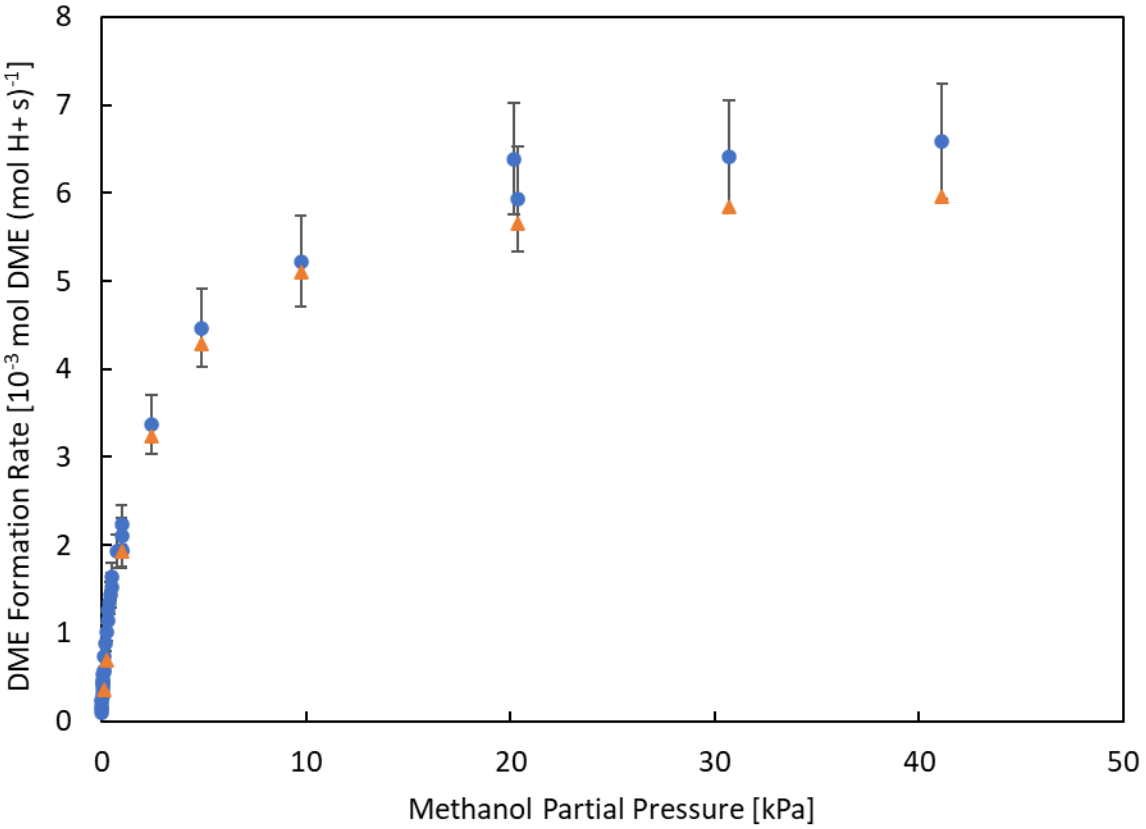

Figure 4.2: Microkinetic model output (orange ▲) of DME formation rates versus methanol partial pressure assuming a Boltzmann distribution of T-sites based on relative aluminum exchange energies, plotted against experimental data (blue ●).

4.4.3. Reaction Flux Analysis

Reaction fluxes for each pressure condition were evaluated by taking a snapshot at the simulated reactor outlet. The fractional contribution of each T-site to DME production, evaluated through overall DME desorption, is shown in Figure 3.3.

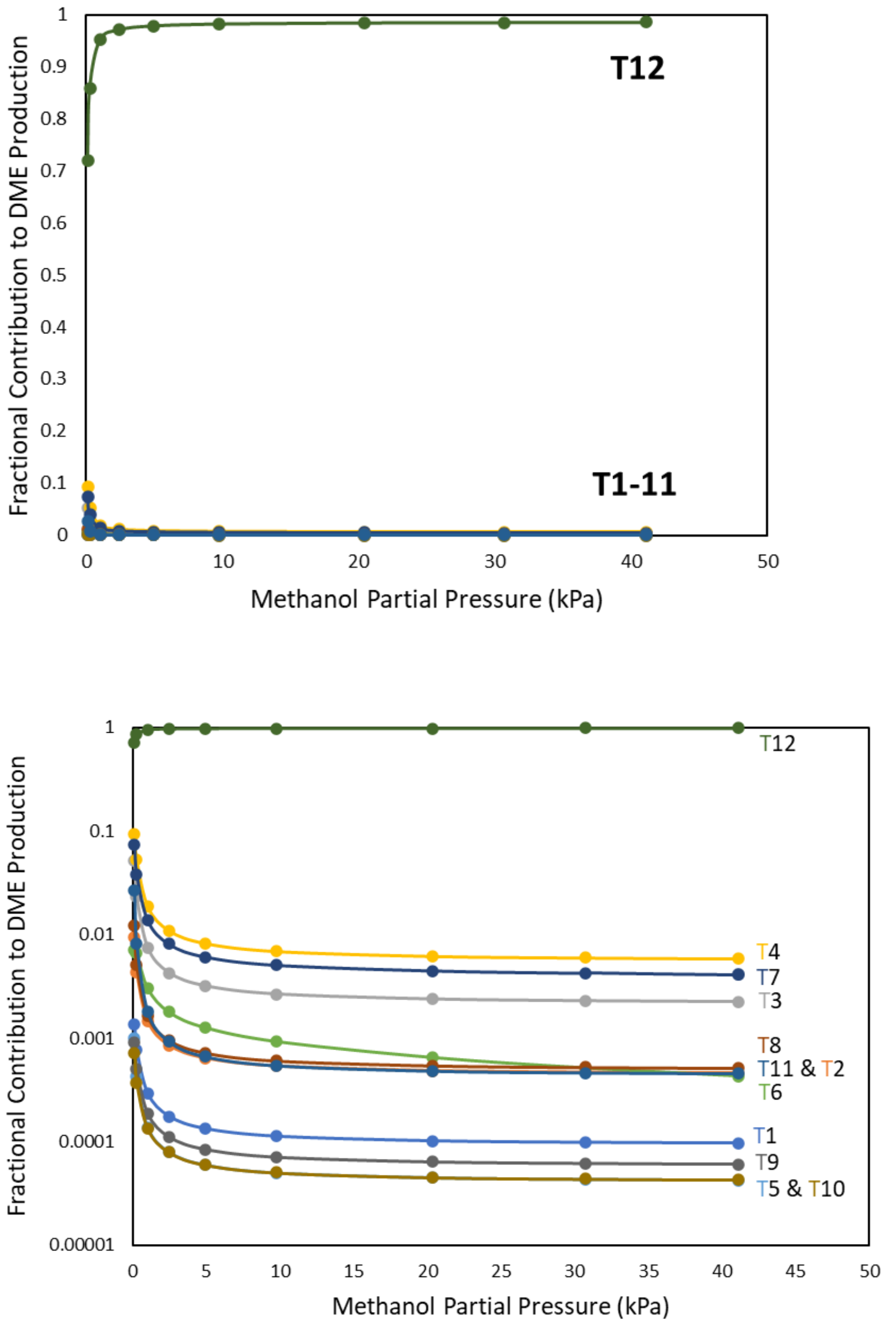

Figure 4.3: Linear and log-scale plots of the fractional contribution of each T-site to overall DME production.

As can be seen, T12 is the dominant factor of DME production at all relevant pressures with the Boltzmann site distribution. To deconvolute the effect of site weighting from fractional contribution to DME production, net fluxes normalized by site weightings are shown in Figure 4.4.

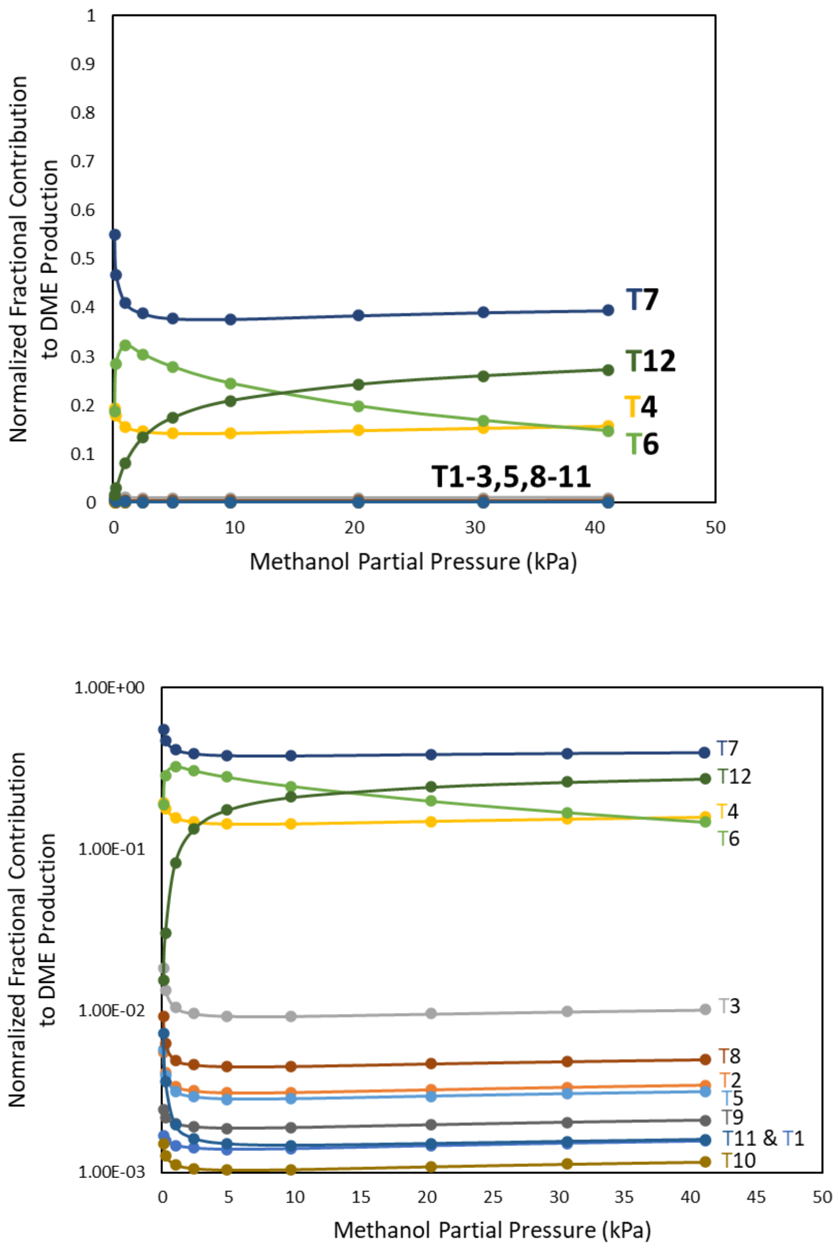

Figure 4.4: Linear and log-scale plots of the fractional contribution of each T-site to overall DME production, normalized by the weighting of each T-site in the relative Boltzmann distribution.

Interestingly, despite T12 dominating DME production for the modeled site distribution, T7 is seen to have the highest normalized fractional contribution to DME production. In order, the contributions of sites T7, T12, T4, and T6 are significantly higher than those of other T-sites within orthorhombic MFI for methanol dehydration to DME. The fractional net flux through each of the dimer, trimer, and tetramer pathways of T12 are shown in Figure 4.5 to further investigate the major pathways. The sequential pathway through the elimination of a methanol monomer into a bound methoxy species was not seen to carry any significant flux for any of the T-sites at the modeled pressure conditions, in contrast to the case of methanol dehydration on chabazite.[20]

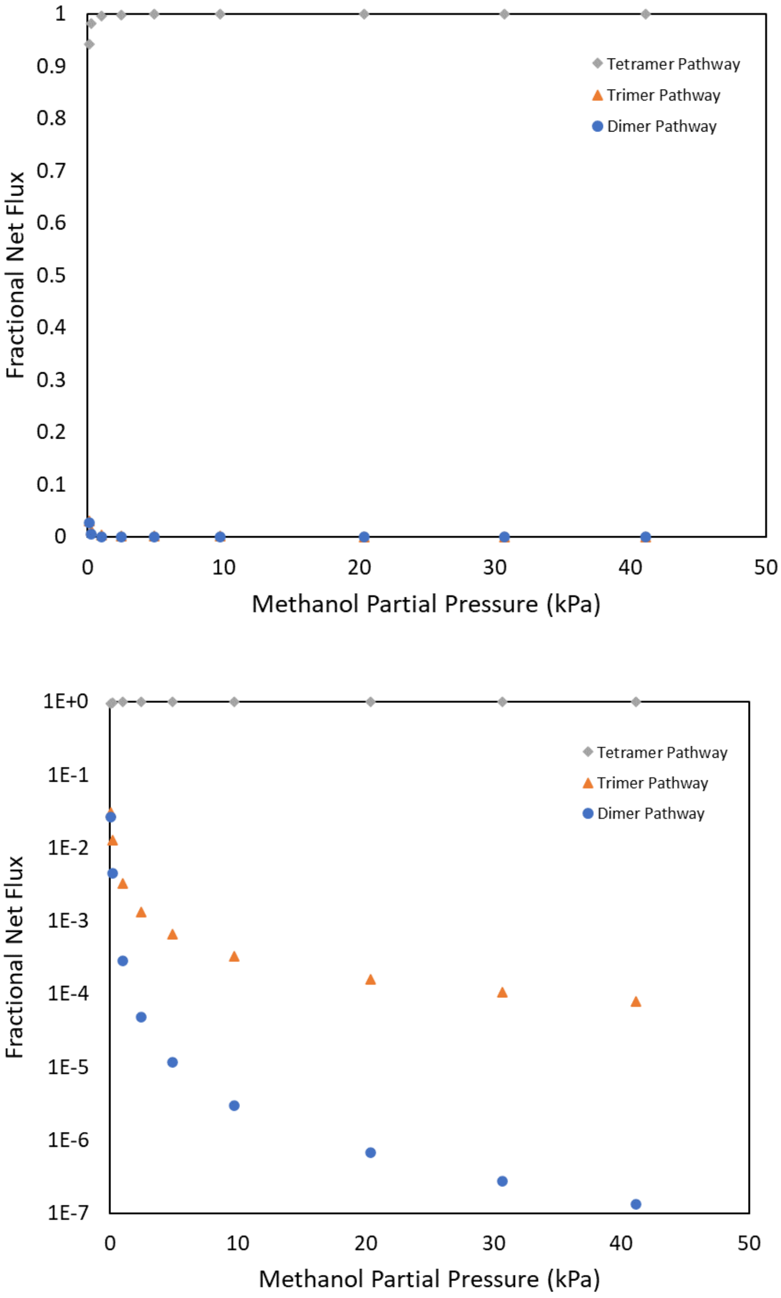

Figure 4.5: Linear and log-scale plots of the fractional net flux through the dimer, trimer, and tetramer pathways of T12.

In sharp contrast to the case of methanol dehydration on chabazite,[20] there is a lack of inhibition in the tetramer regime. In fact, the tetramer pathway dominates all pressure conditions evaluated, increasing in dominance as pressure rises. There is the possibility that if pentamers were mechanistically allowed to carry flux rather than being considered inhibiting species, the T-site distribution would not require as much weighting towards T12 and the assumption of a Boltzmann distribution of sites could be relaxed.

The strength of the tetramer pathway seen over T12 gives insight into the reason for the normalized dominance of T7, T12, T4, and T6 – these sites have significantly lower activation barriers for the transition state of the tetramer route compared to the other T-sites. For the cases of T7, T12, and T6, this could be due to their positions at channel intersections, allowing for the stabilization of larger intermediates due to the void space around these T-sites. T4 is not accessible from a channel intersection, though it shares a ring with T12 and T7. The activation barriers are plotted in Figure 4.6, in order of highest normalized contribution to DME production at the highest pressure condition. The activation energies for T7, T12, T4, and T6 are between 120 and 125 kJ/mol, in contrast to the other sites with barriers between 130 and 145 kJ/mol. T6 is seen to have a lower activation barrier than either T12 or T4; the reason it lags behind the other three will be explained with surface speciation analysis. Full reaction coordinates for the dimer, trimer, and tetramer pathways over each T-site are presented in Figures B1, B2, and B3 of the appendix.

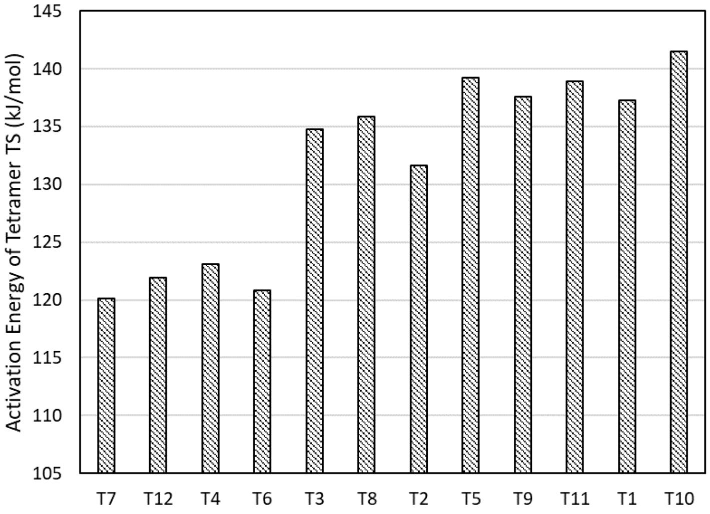

Figure 4.6: Activation energy for the tetramer pathway, plotted in order of the highest normalized contribution to DME production at the highest pressure condition modeled.

4.4.4. Surface Speciation Analysis

A comparison of the major surface species between all 12 T-sites is shown in Figure 4.7. The methanol dimer is only a relevant species on less than half of the T-sites, namely T4, T6, T8, T10, and T11, and only at the lowest pressure conditions considered. Inhibiting pentamers are only seen in meaningful quantity at high pressures on T7 and especially T6, explaining the decreasing trend of DME production with pressure on T6 sites despite the low activation barrier for the tetramer pathway over T6. In general, tetramers dominate the medium and high-pressure conditions on every T-site. There is a notable exception – namely, T12 displays a balance between methanol trimers and tetramers at 2.44 kPa, despite lacking significant trimer flux, and does not see the near 100% coverage of tetramers at 41.13 kPa seen on other T-sites. This weaker preference towards tetramer formation explains the different behavior for DME formation rate versus pressure seen for T12 in Figure 4.4 when compared to the other T-sites of MFI.

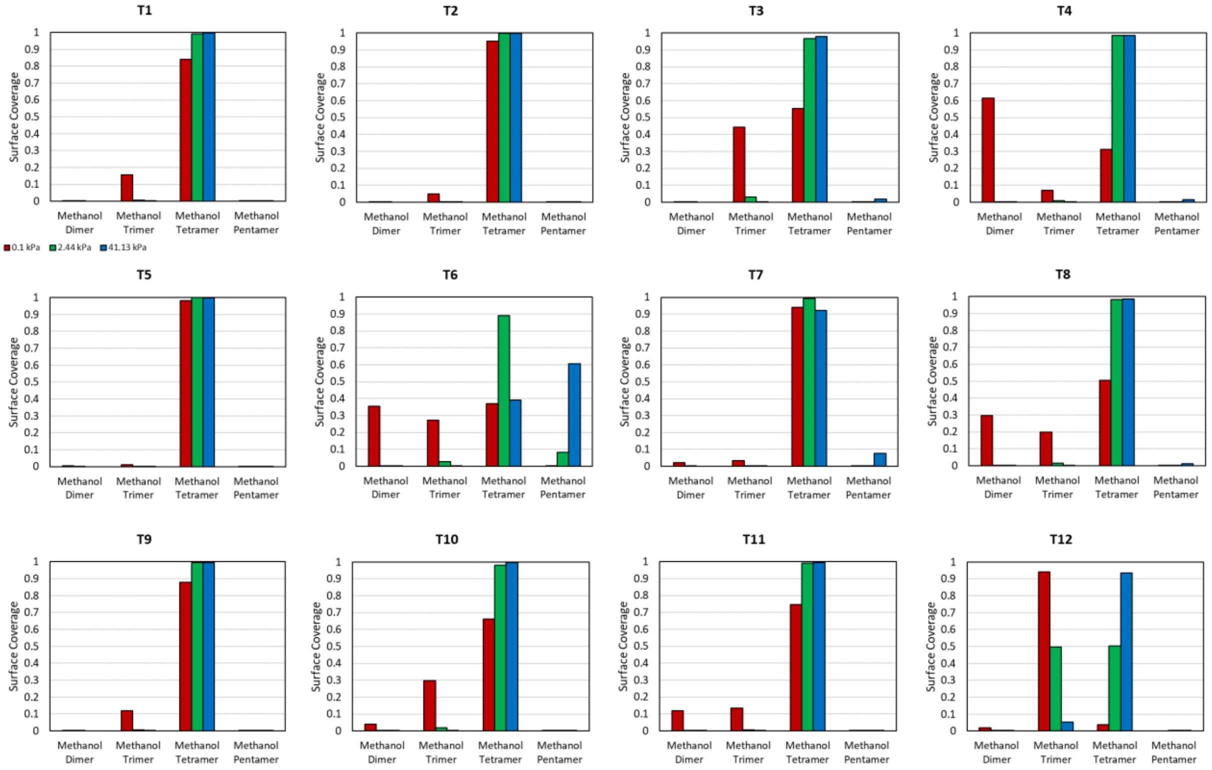

Figure 4.7: The surface coverage of major species for all T-sites evaluated at different methanol partial pressures. Red, left bar: 0.1 kPa. Green, middle bar: 2.44 kPa. Blue, right bar: 41.13 kPa.

4.4.5. Degree of Rate Control Analysis

Degree of rate control analysis[76] was applied to the formation of DME to understand to what degree every reaction on every T-site controls the production of DME at each pressure. The following equation was used:

$$X_i = \frac{k_i}{r}\left(\frac{\partial r}{\partial k_i}\right)_{k_{j\neq i},K_i} = \left(\frac{\partial \ln(r)}{\partial \ln(k_i)}\right)_{k_{j\neq i},K_i} = \left(\frac{\partial \ln(r)}{\partial\left(\frac{-\Delta G_i^{TS}}{RT}\right)}\right)_{k_{j\neq i},K_i} \tag{4.5}$$

Where X_i is the sensitivity coefficient of elementary step i, k_i is the rate constant of that elementary step, r is the net rate of formation of the product of interest, taken here to be DME, K_i is the equilibrium constant for reversible elementary steps, and ΔG_i^{TS} is the Gibbs free energy of activation of the transition state of reaction i. The results of this analysis are shown in Figure 4.8.

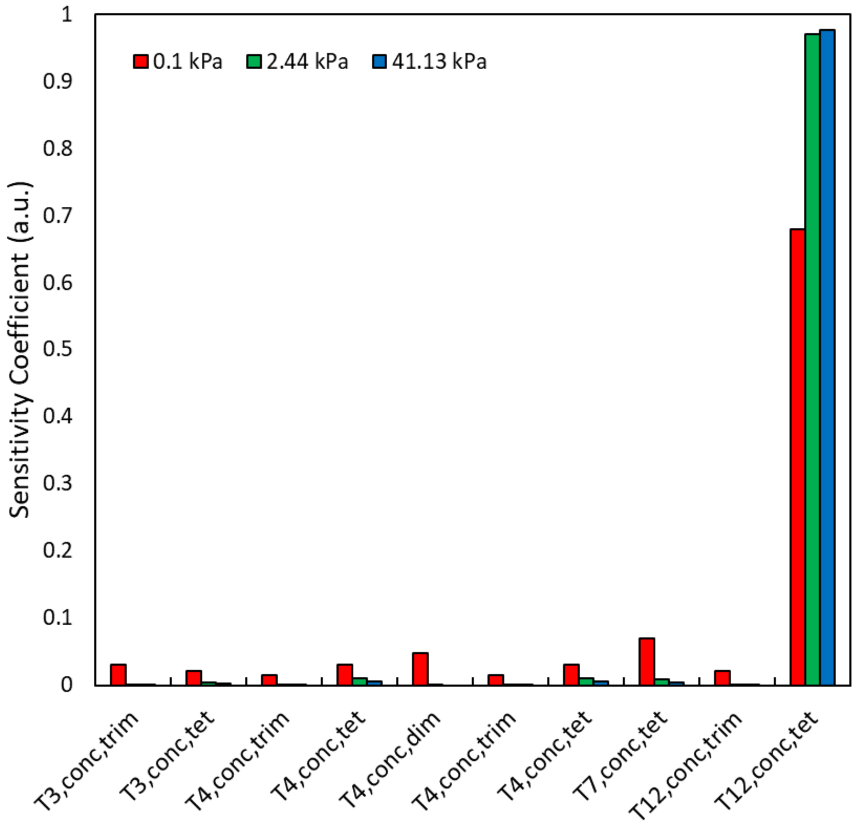

Figure 4.8: Parameters that displayed significant degree of rate control for the formation of DME evaluated at different methanol partial pressures. Red, left bar: 0.1 kPa. Green, middle bar: 2.44 kPa. Blue, right bar: 41.13 kPa.

As expected, the most controlling step for DME formation for every pressure regime considered is the formation of bound DME from the methanol tetramer on T12. This control increases with pressure, with trimer and tetramer DME formation displaying relevance at low pressure conditions for T3, T4, and T7, and dimer DME formation additionally displaying relevance on T4, matching with its unusually high speciation at these conditions on T4. T4 and T7 display control over DME formation despite their low weighting in the site distribution, aligning with their relevance identified in flux analysis.

4.5. Conclusions

A DFT-parameterized microkinetic model of methanol dehydration to DME over all 12 independent T-sites in the orthorhombic form of MFI is presented. Using flux analysis, surface speciation analysis, and degree of rate control analysis, the primary drivers of DME production are identified to be through methanol tetramers, with T-sites that have lower activation barriers for the tetramer pathway generally providing higher weight-normalized contribution to DME flux. In particular, T4, T6, T7, and T12 were seen to be the dominant T-sites for the promotion of methanol dehydration. Future work may relax the site distribution assumptions present in this model by modeling potential mechanistic pathways through methanol pentamers, hexamers, and so on. The technique presented in this work expands the framework developed for evaluating paired sites within zeolites to now capture location effects as well, encompassing the two major factors for predictively modeling the impact of industrially relevant catalytic properties on the process scale from atomic scale knowledge, providing a holistic platform to enable the rational design of next-generation catalytic materials.

Chapter 5: Conclusions and Recommendations for Future Research

5.1. Summary

This dissertation presents a modeling framework to evaluate chemistry core to fuel conversion, both thermally and in complex catalytic systems. In Chapter 2, a DFT-parameterized microkinetic model was developed to capture the effects of acid side proximity in chabazite on methanol dehydration rates. Flux analysis and surface speciation analysis were used to identify two primary drivers of methanol dehydration chemistry. At low pressures, the dominant driver was a sequential pathway through a bound methoxy intermediate. As pressure increased, methanol trimer clusters were seen to be the critical intermediate, most strongly promoted by a next-nearest neighbor paired acid site configuration.

Chapter 3 introduced a more complex reaction network, focusing on the thermal oligomerization of ethylene. A DFT-parameterized microkinetic model was developed for this system using a truncated reaction network in order to investigate both how the reaction system initiates and how odd-numbered carbon species are produced. The dominant initiation mode was identified through flux analysis to be the direct formation of a 1,4-butyl diradical by two ethylene molecules that undergoes hydrogen abstraction with ethylene to form a 1-butyl radical and a vinyl radical. As conversion increased, a switch in the primary initiation mode was seen, with an increase in the concentration of 1-butene causing significant formation of a resonance-stabilized butene diradical. Within the truncated reaction network modeled, the odd-numbered carbon species were identified to arise from β-scission of C_8 mid-radicals, which were formed via intramolecular hydrogen shift reactions.

Chapter 4 applied the microkinetic modeling scheme to a more complex zeolite topology than chabazite, looking again at methanol dehydration but with a focus on MFI, a zeolite structure containing 12 crystallographically unique T-sites. Analysis of flux, surface speciation, and degree of rate control identified the primary drivers of methanol dehydration on MFI to be methanol tetramers, in contrast to the key intermediate of methanol trimers on CHA identified in Chapter 2. T-sites with lower activation barriers for the tetramer pathway were seen to dominate contribution to DME flux, specifically T4, T6, T7, and T12.

Altogether, the work presented in this dissertation demonstrates a predictive microkinetic modeling technique applicable to complex catalysts, capturing effects of T-site pairing and location, with the capability to encapsulate complex reaction networks, such as the oligomerization of ethylene. This technique provides predictive detail capable of modeling industrially relevant catalytic effects from atomic scale energy information from density functional theory.

5.2. Recommendations for Future Research

The reaction mechanism presented in Chapter 3, Microkinetic Modeling of the Homogeneous Thermal Oligomerization of Ethylene to Liquid-Fuel Range Hydrocarbons, is truncated at C_9 species, and only focuses on linear species. While this was motivated by the product distributions observed in the experimental data, the mismatch between the experimental yields and model results for C_7 species indicates that future work should expand on this mechanism through the use of automated network generation, covering more possible radical species and expanding to higher molecular weights. In addition, with a fully reversible reaction network, more in-depth sensitivity analysis techniques can be utilized. In particular, the degree of rate control analysis approach applied in Chapter 2 and Chapter 4 could be applied to this system to potentially capture more precise sensitivity insights.

For the work presented in Chapter 4, density functional theory calculations were only available for some of the reactions in the network, requiring the use of approximations to evaluate kinetic parameters for crowded desorption events and reverse reaction steps, and ultimately requiring an assumption of what T-site distribution characterized the working catalyst. Density functional theory calculations should be performed to tighten the parameter set and allow for the site distribution assumption to be relaxed or investigated further if it proves necessary under a tighter parameter set. Additionally, as methanol tetramers were not seen to be inhibiting on MFI, the mechanism in the microkinetic model and requisite density functional theory calculations should be expanded through methanol pentamers and potentially methanol hexamers based on the available void space within the channel intersections of MFI.

Beyond mechanistic modifications to the work presented in this dissertation, the developed framework has shown value in independently evaluating acid site proximity effects in zeolites, acid site location effects in zeolites, and oligomerization chemistry. To achieve the end-goal of developing a highly selective catalyst for oligomerization of molecules derived from natural gas, these independent effects should be combined to create a model of ethylene and/or propylene oligomerization within a zeolite in the presence of both acid site proximity and acid site location effects. Before engaging in this endeavor, one potential direct next project would be evaluating the simple test case of methanol dehydration in a system with both pairing and location effects, namely by investigating pairing effects within MFI, to address any issues around the large number of potential T-site pair permutations possible in the system.

References

References:

(1) Malakoff, D. The gas surge. *Science* **2014**, *344* (6191), 1464-1467. DOI: 10.1126/science.344.6191.1464.

(2) Munasib, A.; Rickman, D. S. Regional economic impacts of the shale gas and tight oil boom: A synthetic control analysis. *Regional Science and Urban Economics* **2015**, *50*, 1-17.

(3) Trembath, A.; Jenkins, J.; Nordhaus, T.; Shellenberger, M. Where the shale gas revolution came from. *The Breakthrough Institute* **2012**, *23*.

(4) Jacoby, H. D.; O'Sullivan, F. M.; Paltsev, S. The influence of shale gas on US energy and environmental policy. *Economics of Energy & Environmental Policy* **2012**, *1* (1), 37-52.

(5) Wang, Z.; Krupnick, A. A retrospective review of shale gas development in the United States: What led to the boom? *Economics of Energy & Environmental Policy* **2015**, *4* (1), 5-18.

(6) Sieminski, A. Outlook for US shale oil and gas. *USEI Administration (ed) Argus Americas Crude Summit, Houston* **2014**.

(7) U.S. Energy Information Administration. *U.S. Shale Production*. U.S. Energy Information Administration, 2022. https://www.eia.gov/dnav/ng/hist/res_epg0_r5302_nus_bcfa.htm (accessed April 18, 2023).

(8) Burnham, A.; Han, J.; Clark, C. E.; Wang, M.; Dunn, J. B.; Palou-Rivera, I. Life-cycle greenhouse gas emissions of shale gas, natural gas, coal, and petroleum. *Environmental science & technology* **2012**, *46* (2), 619-627.

(9) Weber, C. L.; Clavin, C. Life cycle carbon footprint of shale gas: Review of evidence and implications. *Environmental science & technology* **2012**, *46* (11), 5688-5695.

(10) Jaramillo, P.; Griffin, W. M.; Matthews, H. S. Comparative life-cycle air emissions of coal, domestic natural gas, LNG, and SNG for electricity generation. *Environmental science & technology* **2007**, *41* (17), 6290-6296.

(11) Brown, S. P.; Yücel, M. K. Shale Gas and Tight Oil Boom: US States' Economic Gains and Vulnerabilities. **2013**.

(12) McFarland, E. Unconventional chemistry for unconventional natural gas. *Science* **2012**, *338* (6105), 340-342.

(13) Ghandi, A.; Yeh, S.; Brandt, A. R.; Vafi, K.; Cai, H.; Wang, M. Q.; Scanlon, B. R.; Reedy, R. C. Energy intensity and greenhouse gas emissions from crude oil production in the eagle ford region: input data and analysis methods. *Argonne: Argonne National Laboratory* **2015**.

(14) Davoudi, M.; Rahimpour, M.; Jokar, S.; Nikbakht, F.; Abbasfard, H. The major sources of gas flaring and air contamination in the natural gas processing plants: A case study. *Journal of Natural Gas Science and Engineering* **2013**, *13*, 7-19.

(15) Gao, T.; Lin, W.; Gu, A. Improved processes of light hydrocarbon separation from LNG with its cryogenic energy utilized. *Energy conversion and management* **2011**, *52* (6), 2401-2404.

(16) Wood, D. A.; Nwaoha, C.; Towler, B. F. Gas-to-liquids (GTL): A review of an industry offering several routes for monetizing natural gas. *Journal of Natural Gas Science and Engineering* **2012**, *9*, 196-208.

(17) Caulton, D. R.; Shepson, P. B.; Cambaliza, M. O.; McCabe, D.; Baum, E.; Stirm, B. H. Methane destruction efficiency of natural gas flares associated with shale formation wells. *Environmental science & technology* **2014**, *48* (16), 9548-9554.

(18) Goellner, J. F. Expanding the shale gas infrastructure. *Gas* **2012**, *2* (C3), C4.

(19) U.S. Energy Information Administration. Early Release: Annotated Summary of Two Cases. *Annual Energy Outlook* **2016**.

(20) Marsden, G.; Kostetskyy, P.; Sekiya, R.-S.; Hoffman, A.; Lee, S.; Gounder, R.; Hibbitts, D.; Broadbelt, L. J. Quantifying Effects of Active Site Proximity on Rates of Methanol Dehydration to Dimethyl Ether over Chabazite Zeolites through Microkinetic Modeling. *ACS Materials Au* **2022**, *2* (2), 163-175. DOI: 10.1021/acsmaterialsau.1c00057.

(21) Haag, W. O.; Lago, R. M.; Weisz, P. B. The active site of acidic aluminosilicate catalysts. *Nature* **1984**, *309* (5969), 589-591, Article. DOI: 10.1038/309589a0.

(22) Dusselier, M.; Davis, M. E. Small-Pore Zeolites: Synthesis and Catalysis. *Chemical Reviews* **2018**, *118* (11), 5265-5329, Review. DOI: 10.1021/acs.chemrev.7b00738.

(23) Shamzhy, M.; Opanasenko, M.; Concepcion, P.; Martinez, A. New trends in tailoring active sites in zeolite-based catalysts. *Chemical Society Reviews* **2019**, *48* (4), 1095-1149. DOI: 10.1039/c8cs00887f.

(24) Corma, A. Inorganic Solid Acids and Their Use in Acid-Catalyzed Hydrocarbon Reactions. *Chemical Reviews* **1995**, *95* (3), 559-614. DOI: 10.1021/cr00035a006.

(25) Bates, J. S.; Bukowski, B. C.; Greeley, J.; Gounder, R. Structure and solvation of confined water and water–ethanol clusters within microporous Brønsted acids and their effects on ethanol dehydration catalysis. *Chemical Science* **2020**, *11* (27), 7102-7122. DOI: 10.1039/d0sc02589e.

(26) Berkson, Z. J.; Hsieh, M. F.; Smeets, S.; Gajan, D.; Lund, A.; Lesage, A.; Xie, D.; Zones, S. I.; McCusker, L. B.; Baerlocher, C.; et al. Preferential Siting of Aluminum Heteroatoms in the Zeolite Catalyst Al-SSZ-70. *Angewandte Chemie-International Edition* **2019**, *58* (19), 6255-6259, Article. DOI: 10.1002/anie.201813533.

(27) Dedecek, J.; Balgova, V.; Pashkova, V.; Klein, P.; Wichterlova, B. Synthesis of ZSM-5 Zeolites with Defined Distribution of Al Atoms in the Framework and Multinuclear MAS NMR Analysis of the Control of Al Distribution. *Chemistry of Materials* **2012**, *24* (16), 3231-3239, Article. DOI: 10.1021/cm301629a.

(28) Dedecek, J.; Sobalik, Z.; Wichterlova, B. Siting and Distribution of Framework Aluminium Atoms in Silicon-Rich Zeolites and Impact on Catalysis. *Catalysis Reviews-Science and Engineering* **2012**, *54* (2), 135-223, Review. DOI: 10.1080/01614940.2012.632662.

(29) Devos, J.; Bols, M. L.; Plessers, D.; Van Goethem, C.; Seo, J. W.; Hwang, S. J.; Sels, B. F.; Dusselier, M. Synthesis-Structure-Activity Relations in Fe-CHA for C-H Activation: Control of Al Distribution by Interzeolite Conversion. *Chemistry of Materials* **2020**, *32* (1), 273-285, Article. DOI: 10.1021/acs.chemmater.9b03738.

(30) Di Iorio, J. R.; Gounder, R. Controlling the Isolation and Pairing of Aluminum in Chabazite Zeolites Using Mixtures of Organic and Inorganic Structure-Directing Agents. *Chemistry of Materials* **2016**, *28* (7), 2236-2247, Article. DOI: 10.1021/acs.chemmater.6b00181.

(31) Di Iorio, J. R.; Nimlos, C. T.; Gounder, R. Introducing Catalytic Diversity into Single-Site Chabazite Zeolites of Fixed Composition via Synthetic Control of Active Site Proximity. *ACS Catal.* **2017**, *7* (10), 6663-6674.

(32) Li, C. G.; Vidal-Moya, A.; Miguel, P. J.; Dedecek, J.; Boronat, M.; Corma, A. Selective Introduction of Acid Sites in Different Confined Positions in ZSM-5 and Its Catalytic Implications. *ACS Catalysis* **2018**, *8* (8), 7688-7697, Article. DOI: 10.1021/acscatal.8b02112.

(33) Mlekodaj, K.; Dedecek, J.; Pashkova, V.; Tabor, E.; Klein, P.; Urbanova, M.; Karcz, R.; Sazama, P.; Whittleton, S. R.; Thomas, H. M.; et al. Al Organization in the SSZ-13 Zeolite. Al Distribution and Extraframework Sites of Divalent Cations. *Journal of Physical Chemistry C* **2019**, *123* (13), 7968-7987, Article. DOI: 10.1021/acs.jpcc.8b07343.

(34) Wang, S.; He, Y.; Jiao, W. Y.; Wang, J. G.; Fan, W. B. Recent experimental and theoretical studies on Al siting/acid site distribution in zeolite framework. *Current Opinion in Chemical Engineering* **2019**, *23*, 146-154, Review. DOI: 10.1016/j.coche.2019.04.002.

(35) Di Iorio, J. R.; Li, S.; Jones, C. B.; Nimlos, C. T.; Wang, Y.; Kunkes, E.; Vattipalli, V.; Prasad, S.; Moini, A.; Schneider, W. F.; et al. Cooperative and Competitive Occlusion of Organic and Inorganic Structure-Directing Agents within Chabazite Zeolites Influences Their Aluminum Arrangement. *Journal of the American Chemical Society* **2020**, *142* (10), 4807-4819. DOI: 10.1021/jacs.9b13817.

(36) Devos, J.; Bols, M. L.; Plessers, D.; Goethem, C. V.; Seo, J. W.; Hwang, S.-J.; Sels, B. F.; Dusselier, M. Synthesis–Structure–Activity Relations in Fe-CHA for C–H Activation: Control of Al Distribution by Interzeolite Conversion. *Chemistry of Materials* **2020**, *32* (1), 273-285. DOI: 10.1021/acs.chemmater.9b03738.

(37) Liang, Y.; Jacobson, A. J.; Rimer, J. D. Strontium Ions Function as Both an Accelerant and Structure-Directing Agent of Chabazite Crystallization. *ACS Materials Letters* **2021**, *3* (2), 187-192. DOI: 10.1021/acsmaterialslett.0c00460.

(38) Loewenstein, W. The distribution of aluminum in the tetrahedra of silicates and aluminates. *American Mineralogist* **1954**, *39* (1-2), 92-96.

(39) Gounder, R.; Jones, A. J.; Carr, R. T.; Iglesia, E. Solvation and acid strength effects on catalysis by faujasite zeolites. *Journal of Catalysis* **2012**, *286*, 214-223. DOI: 10.1016/j.jcat.2011.11.002.

(40) Di Iorio, J. R.; Hoffman, A. J.; Nimlos, C. T.; Nystrom, S.; Hibbitts, D.; Gounder, R. Mechanistic origins of the high-pressure inhibition of methanol dehydration rates in small-pore acidic zeolites. *J Catal* **2019**, *380*, 161-177.

(41) Vernuccio, S.; Bickel, E. E.; Gounder, R.; Broadbelt, L. J. Microkinetic Model of Propylene Oligomerization on Bronsted Acidic Zeolites at Low Conversion. *ACS Catalysis* **2019**, *9* (10), 8996-9008. DOI: 10.1021/acscatal.9b02066.

(42) Hoffman, A. J.; Bates, J. S.; Di Iorio, J. R.; Nystrom, S. V.; Nimlos, C. T.; Gounder, R.; Hibbitts, D. Rigid Arrangements of Ionic Charge in Zeolite Frameworks Conferred by Specific Aluminum Distributions Preferentially Stabilize Alkanol Dehydration Transition States. *Angewandte Chemie-International Edition* **2020**, *59* (42), 18686-18694. DOI: 10.1002/anie.202007790.

(43) Smith, A. T.; Plessow, P. N.; Studt, F. Trends in the Reactivity of Proximate Aluminum Sites in H-SSZ-13. *The Journal of Physical Chemistry C* **2021**, *125* (30), 16508-16515. DOI: 10.1021/acs.jpcc.1c03509.

(44) Nastase, S. A. F.; Cnudde, P.; Vanduyfhuys, L.; De Wispelaere, K.; Van Speybroeck, V.; Catlow, C. R. A.; Logsdail, A. J. Mechanistic Insight into the Framework Methylation of H-ZSM-5 for Varying Methanol Loadings and Si/Al Ratios Using First-Principles Molecular Dynamics Simulations. *ACS Catalysis* **2020**, *10* (15), 8904-8915. DOI: 10.1021/acscatal.0c01454.

(45) Baerlocher, C.; McCusker, L. B. *Database of Zeolite Structures (accessed August 2020).* http://www.iza-structure.org/databases/

(46) Bräuer, P.; Ng, P. L.; Situmorang, O.; Hitchcock, I.; D'Agostino, C. Effect of Al content on number and location of hydroxyl acid species in zeolites: a DRIFTS quantitative protocol without the need for molar extinction coefficients. *RSC Advances* **2017**, *7* (83), 52604-52613. DOI: 10.1039/c7ra10699h.

(47) Nystrom, S.; Hoffman, A.; Hibbitts, D. Tuning Bronsted Acid Strength by Altering Site Proximity in CHA Framework Zeolites. *ACS Catalysis* **2018**, *8* (9), 7842-7860, Article. DOI: 10.1021/acscatal.8b02049.

(48) Carr, R. T.; Neurock, M.; Iglesia, E. Catalytic consequences of acid strength in the conversion of methanol to dimethyl ether. *Journal of Catalysis* **2011**, *278* (1), 78-93, Article. DOI: 10.1016/j.jcat.2010.11.017.

(49) Jones, A. J.; Zones, S. I.; Iglesia, E. Implications of Transition State Confinement within Small Voids for Acid Catalysis. *Journal of Physical Chemistry C* **2014**, *118* (31), 17787-17800. DOI: 10.1021/jp5050095.

(50) Bates, J. S.; Bukowski, B. C.; Greeley, J.; Gounder, R. Structure and solvation of confined water and water-ethanol clusters within microporous Bronsted acids and their effects on ethanol dehydration catalysis. *Chemical Science* **2020**, *11* (27), 7102-7122. DOI: 10.1039/d0sc02589e.

(51) Kresse, G.; Furthmuller, J. Efficiency of ab-initio total energy calculations for metals and semiconductors using a plane-wave basis set. *Computational Materials Science* **1996**, *6* (1), 15-50. DOI: 10.1016/0927-0256(96)00008-0.

(52) Kresse, G.; Furthmuller, J. Efficient iterative schemes for ab initio total-energy calculations using a plane-wave basis set. *Physical Review B* **1996**, *54* (16), 11169-11186. DOI: 10.1103/PhysRevB.54.11169.

(53) Kravchenko, P.; Plaisance, C.; Hibbitts, D. A New Computational Interface for Catalysis. *ChemRxiv* **2019**.

(54) Kresse, G.; Joubert, D. From ultrasoft pseudopotentials to the projector augmented-wave method. *Physical Review B* **1999**, *59* (3), 1758-1775. DOI: 10.1103/PhysRevB.59.1758.

(55) Blochl, P. E. Projector augmented-wave method. *Physical Review B* **1994**, *50* (24), 17953-17979. DOI: 10.1103/PhysRevB.50.17953.

(56) Grimme, S.; Ehrlich, S.; Goerigk, L. Effect of the Damping Function in Dispersion Corrected Density Functional Theory. *Journal of Computational Chemistry* **2011**, *32* (7), 1456-1465. DOI: 10.1002/jcc.21759.

(57) Grimme, S.; Antony, J.; Ehrlich, S.; Krieg, H. A consistent and accurate ab initio parametrization of density functional dispersion correction (DFT-D) for the 94 elements H-Pu. *Journal of Chemical Physics* **2010**, *132* (15). DOI: 10.1063/1.3382344.

(58) Hoffman, A.; Deluca, M.; Hibbitts, D. Restructuring of MFI Framework Zeolite Models and Their Associated Artifacts in Density Functional Theory Calculations. *The Journal of Physical Chemistry C* **2019**, *123* (11), 6572-6585. DOI: 10.1021/acs.jpcc.8b12230.

(59) Deluca, M.; Kravchenko, P.; Hoffman, A.; Hibbitts, D. Mechanism and Kinetics of Methylating C6–C12 Methylbenzenes with Methanol and Dimethyl Ether in H-MFI Zeolites. *ACS Catalysis* **2019**, *9* (7), 6444-6460. DOI: 10.1021/acscatal.9b00650.

(60) Grifoni, E.; Piccini, G.; Lercher, J. A.; Glezakou, V.-A.; Rousseau, R.; Parrinello, M. Confinement effects and acid strength in zeolites. *Nature Communications* **2021**, *12* (1). DOI: 10.1038/s41467-021-22936-0.

(61) Wang, M.; Jaegers, N. R.; Lee, M.-S.; Wan, C.; Hu, J. Z.; Shi, H.; Mei, D.; Burton, S. D.; Camaioni, D. M.; Gutiérrez, O. Y.; et al. Genesis and Stability of Hydronium Ions in Zeolite Channels. *Journal of the American Chemical Society* **2019**, *141* (8), 3444-3455. DOI: 10.1021/jacs.8b07969.

(62) Alexopoulos, K.; Lee, M.-S.; Liu, Y.; Zhi, Y.; Liu, Y.; Reyniers, M.-F.; Marin, G. B.; Glezakou, V.-A.; Rousseau, R.; Lercher, J. A. Anharmonicity and Confinement in Zeolites: Structure, Spectroscopy, and Adsorption Free Energy of Ethanol in H-ZSM-5. *The Journal of Physical Chemistry C* **2016**, *120* (13), 7172-7182. DOI: 10.1021/acs.jpcc.6b00923.

(63) Bukowski, B. C.; Bates, J. S.; Gounder, R.; Greeley, J. Defect-Mediated Ordering of Condensed Water Structures in Microporous Zeolites. *Angewandte Chemie International Edition* **2019**, *58* (46), 16422-16426. DOI: 10.1002/anie.201908151.

(64) Bukowski, B. C.; Bates, J. S.; Gounder, R.; Greeley, J. First principles, microkinetic, and experimental analysis of Lewis acid site speciation during ethanol dehydration on Sn-Beta zeolites. *Journal of Catalysis* **2018**, *365*, 261-276. DOI: 10.1016/j.jcat.2018.07.012.

(65) McQuarrie, D. A. *Statistical mechanics*; University Science Books, **2000**.

(66) Ghorbanpour, A.; Rimer, J. D.; Grabow, L. C. Computational Assessment of the Dominant Factors Governing the Mechanism of Methanol Dehydration over H-ZSM-5 with Heterogeneous Aluminum Distribution. *ACS Catalysis* **2016**, *6* (4), 2287-2298. DOI: 10.1021/acscatal.5b02367.

(67) Mei, D.; Lercher, J. A. Mechanistic insights into aqueous phase propanol dehydration in H-ZSM-5 zeolite. *AIChE Journal* **2017**, *63* (1), 172-184. DOI: 10.1002/aic.15517.

(68) Jones, A. J.; Iglesia, E. Kinetic, Spectroscopic, and Theoretical Assessment of Associative and Dissociative Methanol Dehydration Routes in Zeolites. *Angewandte Chemie-International Edition* **2014**, *53* (45), 12177-12181, Article. DOI: 10.1002/anie.201406823.

(69) Mirth, G.; Lercher, J. A.; Anderson, M. W.; Klinowski, J. Adsorption complexes of methanol on zeolite ZSM-5. *Journal of the Chemical Society-Faraday Transactions* **1990**, *86* (17), 3039-3044, Article. DOI: 10.1039/ft9908603039.

(70) Vjunov, A.; Wang, M.; Govind, N.; Huthwelker, T.; Shi, H.; Mei, D.; Fulton, J. L.; Lercher, J. A. Tracking the Chemical Transformations at the Brønsted Acid Site upon Water-Induced Deprotonation in a Zeolite Pore. *Chemistry of Materials* **2017**, *29* (21), 9030-9042. DOI: 10.1021/acs.chemmater.7b02133.

(71) Eckstein, S.; Hintermeier, P. H.; Zhao, R.; Baráth, E.; Shi, H.; Liu, Y.; Lercher, J. A. Influence of Hydronium Ions in Zeolites on Sorption. *Angewandte Chemie International Edition* **2019**, *58* (11), 3450-3455. DOI: 10.1002/anie.201812184.

(72) Zhang, J.; Zhou, R. J.; Chang, Q. Y.; Sui, Z. J.; Zhou, X. G.; Chen, D.; Zhu, Y. A. Tailoring catalytic properties of V2O3 to propane dehydrogenation through single-atom doping: A DFT study. *Catalysis Today* **2021**, *368*, 46-57. DOI: 10.1016/j.cattod.2020.02.023.

(73) Motagamwala, A. H.; Dumesic, J. A. Microkinetic Modeling: A Tool for Rational Catalyst Design. *Chemical Reviews* **2021**, *121* (2), 1049-1076. DOI: 10.1021/acs.chemrev.0c00394.

(74) Baz, A.; Holewinski, A. Predicting macro-kinetic observables in electrocatalysis using the generalized degree of rate control. *Journal of Catalysis* **2021**, *397*, 233-244. DOI: 10.1016/j.jcat.2021.03.014.

(75) Mao, Z. T.; Campbell, C. T. Kinetic Isotope Effects: Interpretation and Prediction Using Degrees of Rate Control. *ACS Catalysis* **2020**, *10* (7), 4181-4192. DOI: 10.1021/acscatal.9b05637.

(76) Campbell, C. T. The Degree of Rate Control: A Powerful Tool for Catalysis Research. *ACS Catalysis* **2017**, *7* (4), 2770-2779. DOI: 10.1021/acscatal.7b00115.

(77) Bell, A. T.; Alger, M. M.; Flytzani-Stephanopoulos, M.; Gunnoe, T. B.; Lercher, J. A.; Stevens, J.; Alper, J.; Tran, C. *The Changing Landscape of Hydrocarbon Feedstocks for Chemical Production: Implications for Catalysis: Proceedings of a Workshop*; National Academies of Sciences, Engineering, and Medicine, Washington, DC, **2016**. DOI: 10.2172/1344369.

(78) Gvakharia, A.; Kort, E. A.; Brandt, A.; Peischl, J.; Ryerson, T. B.; Schwarz, J. P.; Smith, M. L.; Sweeney, C. Methane, Black Carbon, and Ethane Emissions from Natural Gas Flares in the Bakken Shale, North Dakota. *Environmental Science & Technology* **2017**, *51* (9), 5317-5325. DOI: 10.1021/acs.est.6b05183.

(79) Höglund-Isaksson, L. Bottom-up simulations of methane and ethane emissions from global oil and gas systems 1980 to 2012. *Environmental Research Letters* **2017**, *12* (2), 024007. DOI: 10.1088/1748-9326/aa583e.

(80) Ridha, T.; Li, Y.; Gençer, E.; Siirola, J. J.; Miller, J. T.; Ribeiro, F. H.; Agrawal, R. Valorization of Shale Gas Condensate to Liquid Hydrocarbons through Catalytic Dehydrogenation and Oligomerization. *Processes* **2018**, *6* (9), 139.

(81) Olivier-Bourbigou, H.; Breuil, P. A. R.; Magna, L.; Michel, T.; Espada Pastor, M. F.; Delcroix, D. Nickel Catalyzed Olefin Oligomerization and Dimerization. *Chemical Reviews* **2020**, *120* (15), 7919-7983. DOI: 10.1021/acs.chemrev.0c00076.

(82) Finiels, A.; Fajula, F.; Hulea, V. Nickel-based solid catalysts for ethylene oligomerization–a review. *Catalysis Science & Technology* **2014**, *4* (8), 2412-2426.

(83) Chang, C. D. The New Zealand Gas-to-Gasoline plant: An engineering tour de force. *Catalysis today* **1992**, *13* (1), 103-111.

(84) Quann, R. J.; Green, L. A.; Tabak, S. A.; Krambeck, F. J. Chemistry of olefin oligomerization over ZSM-5 catalyst. *Industrial & engineering chemistry research* **1988**, *27* (4), 565-570.

(85) Garwood, W. Conversion of C2-C10 olefins to higher olefins over synthetic zeolite ZSM-5. *ACS Symposium Series* **1983,** *218*. DOI: 10.1021/bk-1983-0218.ch023.

(86) Freitas, E.; Gum, C. R. Shell's higher olefins process. *Chem. Eng. Prog.* **1979**, *75*, 73-76.

(87) Lutz, E. F. Shell higher olefins process. *Journal of Chemical Education* **1986**, *63* (3), 202. DOI: 10.1021/ed063p202.

(88) Galadima, A.; Muraza, O. Revisiting the oxidative coupling of methane to ethylene in the golden period of shale gas: A review. *Journal of Industrial and Engineering Chemistry* **2016**, *37*, 1-13. DOI: https://doi.org/10.1016/j.jiec.2016.03.027.

(89) Conrad, M. A.; Shaw, A.; Marsden, G.; Broadbelt, L. J.; Miller, J. T. Insights into the Chemistry of the Homogeneous Thermal Oligomerization of Ethylene to Liquid-Fuel-Range Hydrocarbons. *Industrial & Engineering Chemistry Research* **2023**, *62* (5), 2202-2216. DOI: 10.1021/acs.iecr.2c02172.

(90) Hurd, C. D. Pyrolysis of unsaturated hydrocarbons. *Industrial & Engineering Chemistry* **1934**, *26* (1), 50-55.

(91) Boyd, M.; Wu, T.; Back, M. Kinetics of the thermal reactions of ethylene. Part I. *Canadian Journal of Chemistry* **1968**, *46* (14), 2415-2426.

(92) Dahlgren, G., Jr.; Douglas, J. E. Kinetics of the Thermal Reactions of Ethylene. *Journal of the American Chemical Society* **1958**, *80* (19), 5108-5110. DOI: 10.1021/ja01552a028.

(93) Boyd, M.; Back, M. Kinetics of the thermal reactions of ethylene. Part II. Ethylene–ethane mixtures. *Canadian Journal of Chemistry* **1968**, *46* (14), 2427-2433.

(94) Halstead, M.; Quinn, C. Pyrolysis of ethylene. *Transactions of the Faraday Society* **1968**, *64*, 103-118.

(95) Simon, M.; Back, M. Kinetics of the thermal reactions of ethylene. *Canadian Journal of Chemistry* **1969**, *47* (2), 251-255.

(96) Storch, H. Kinetics of Ethylene Polymerization. II1. *Journal of the American Chemical Society* **1935**, *57* (12), 2598-2601.

(97) Burnham, H. D.; Pease, R. N. Studies in Gaseous Hydrogenation and Polymerization Reactions1. *Journal of the American Chemical Society* **1942**, *64* (6), 1404-1410.

(98) Buback, M. The high pressure polymerization of pure ethylene. *Die Makromolekulare Chemie: Macromolecular Chemistry and Physics* **1980**, *181* (2), 373-382.

(99) Dewar, M. J.; Kirschner, S. Dimerization of ethylene to cyclobutane. *Journal of the American Chemical Society* **1974**, *96* (16), 5246-5247.

(100) Tsang, W.; Walker, J. A.; Manion, J. A. The decomposition of normal hexyl radicals. *Proceedings of the Combustion Institute* **2007**, *31* (1), 141-148.

(101) Lewis, J.; Martin, J.; Anderson, L. Gamma-activation of synthesis--polymerization of ethylene. *Chem. Eng. Prog.* **1954**, *50.*

(102) Scelta, D.; Ceppatelli, M.; Bini, R. Pressure induced polymerization of fluid ethylene. *The Journal of Chemical Physics* **2016**, *145* (16), 164504.

(103) Vinu, R.; Broadbelt, L. J. Unraveling Reaction Pathways and Specifying Reaction Kinetics for Complex Systems. *Annual Review of Chemical and Biomolecular Engineering* **2012**, *3* (1), 29-54. DOI: 10.1146/annurev-chembioeng-062011-081108.

(104) Evans, M. G.; Polanyi, M. Inertia and driving force of chemical reactions. *Transactions of the Faraday Society* **1938**, *34* (0), 11-24. DOI: 10.1039/TF9383400011.

(105) Benson, S. W.; Cruickshank, F.; Golden, D.; Haugen, G. R.; O'neal, H.; Rodgers, A.; Shaw, R.; Walsh, R. Additivity rules for the estimation of thermochemical properties. *Chemical Reviews* **1969**, *69* (3), 279-324.

(106) Caracotsios, M.; Stewart, W. E.; Petzold, L. DDASAC, Double-Precision Differential or Algebraic Sensitivity Analysis. Nuclear Energy Agency of the OECD (NEA), 1997.

(107) *Gaussian 16 Rev. C.01*; Wallingford, CT, 2016.

(108) Zhao, Y.; Truhlar, D. G. The M06 suite of density functionals for main group thermochemistry, thermochemical kinetics, noncovalent interactions, excited states, and transition elements: two new functionals and systematic testing of four M06-class functionals and 12 other functionals. *Theoretical Chemistry Accounts* **2007**, *120* (1-3), 215-241. DOI: 10.1007/s00214-007-0310-x.

(109) Weigend, F.; Ahlrichs, R. Balanced basis sets of split valence, triple zeta valence and quadruple zeta valence quality for H to Rn: Design and assessment of accuracy. *Phys Chem Chem Phys* **2005**, *7* (18), 3297-3305. DOI: 10.1039/b508541a.

(110) Grimme, S. Supramolecular binding thermodynamics by dispersion-corrected density functional theory. *Chemistry* **2012**, *18* (32), 9955-9964. DOI: 10.1002/chem.201200497.

(111) Luchini, G.; Alegre-Requena, J. V.; Funes-Ardoiz, I.; Paton, R. S. GoodVibes: automated thermochemistry for heterogeneous computational chemistry data. *F1000Research* **2020**, *9*. DOI: 10.12688/f1000research.22758.1.

(112) Li, Y.-P.; Gomes, J.; Mallikarjun Sharada, S.; Bell, A. T.; Head-Gordon, M. Improved Force-Field Parameters for QM/MM Simulations of the Energies of Adsorption for Molecules in Zeolites and a Free Rotor Correction to the Rigid Rotor Harmonic Oscillator Model for Adsorption Enthalpies. *The Journal of Physical Chemistry C* **2015**, *119* (4), 1840-1850. DOI: 10.1021/jp509921r.

(113) Yu, H. Z., J.; Truhlar, D.G. Unpublished data. 2015.

(114) Levine, S. E.; Broadbelt, L. J. Detailed mechanistic modeling of high-density polyethylene pyrolysis: Low molecular weight product evolution. *Polymer Degradation and Stability* **2009**, *94* (5), 810-822. DOI: https://doi.org/10.1016/j.polymdegradstab.2009.01.031.

(115) Pfaendtner, J.; Broadbelt, L. J. Mechanistic Modeling of Lubricant Degradation. 1. Structure−Reactivity Relationships for Free-Radical Oxidation. *Industrial & Engineering Chemistry Research* **2008**, *47* (9), 2886-2896. DOI: 10.1021/ie0714807.

(116) Guo, X.; Guo, L.; Zeng, Y.; Kosol, R.; Gao, X.; Yoneyama, Y.; Yang, G.; Tsubaki, N. Catalytic oligomerization of isobutyl alcohol to jet fuels over dealuminated zeolite Beta. *Catalysis Today* **2021**, *368*, 196-203. DOI: https://doi.org/10.1016/j.cattod.2020.04.047.

(117) Kester, P. M.; Crum, J. T.; Li, S.; Schneider, W. F.; Gounder, R. Effects of Brønsted acid site proximity in chabazite zeolites on OH infrared spectra and protolytic propane cracking kinetics. *Journal of Catalysis* **2021**, *395*, 210-226. DOI: https://doi.org/10.1016/j.jcat.2020.12.038.

(118) Song, C.; Chu, Y.; Wang, M.; Shi, H.; Zhao, L.; Guo, X.; Yang, W.; Shen, J.; Xue, N.; Peng, L.; et al. Cooperativity of adjacent Brønsted acid sites in MFI zeolite channel leads to enhanced polarization and cracking of alkanes. *Journal of Catalysis* **2017**, *349*, 163-174. DOI: https://doi.org/10.1016/j.jcat.2016.12.024.

(119) Mlinar, A. N.; Zimmerman, P. M.; Celik, F. E.; Head-Gordon, M.; Bell, A. T. Effects of Brønsted-acid site proximity on the oligomerization of propene in H-MFI. *Journal of Catalysis* **2012**, *288*, 65-73. DOI: https://doi.org/10.1016/j.jcat.2012.01.002.

(120) Xu, B.; Sievers, C.; Hong, S. B.; Prins, R.; van Bokhoven, J. A. Catalytic activity of Brønsted acid sites in zeolites: Intrinsic activity, rate-limiting step, and influence of the local structure of the acid sites. *Journal of Catalysis* **2006**, *244* (2), 163-168. DOI: https://doi.org/10.1016/j.jcat.2006.08.022.

(121) Niwa, M.; Suzuki, K.; Morishita, N.; Sastre, G.; Okumura, K.; Katada, N. Dependence of cracking activity on the Brønsted acidity of Y zeolite: DFT study and experimental confirmation. *Catalysis Science & Technology* **2013**, *3* (8), 1919-1927, 10.1039/C3CY00195D. DOI: 10.1039/C3CY00195D.

(122) Sanchez-Castillo, M. A.; Madon, R. J.; Dumesic, J. A. Role of Rare Earth Cations in Y Zeolite for Hydrocarbon Cracking. *The Journal of Physical Chemistry B* **2005**, *109* (6), 2164-2175. DOI: 10.1021/jp0489875.

(123) Vernuccio, S.; Bickel, E. E.; Gounder, R.; Broadbelt, L. J. Microkinetic Model of Propylene Oligomerization on Brønsted Acidic Zeolites at Low Conversion. *ACS Catalysis* **2019**, *9* (10), 8996-9008. DOI: 10.1021/acscatal.9b02066.

(124) Van der Mynsbrugge, J.; Janda, A.; Mallikarjun Sharada, S.; Lin, L.-C.; Van Speybroeck, V.; Head-Gordon, M.; Bell, A. T. Theoretical Analysis of the Influence of Pore Geometry on Monomolecular Cracking and Dehydrogenation of n-Butane in Brønsted Acidic Zeolites. *ACS Catalysis* **2017**, *7* (4), 2685-2697. DOI: 10.1021/acscatal.6b03646.

(125) Lin, L.-C. Computational Study of Alkane Adsorption in Brønsted Acid Zeolites for More Efficient Alkane Cracking. *Langmuir* **2022**, *38* (25), 7665-7677. DOI: 10.1021/acs.langmuir.2c00923.

(126) Janda, A.; Vlaisavljevich, B.; Lin, L.-C.; Mallikarjun Sharada, S.; Smit, B.; Head-Gordon, M.; Bell, A. T. Adsorption Thermodynamics and Intrinsic Activation Parameters for Monomolecular Cracking of n-Alkanes on Brønsted Acid Sites in Zeolites. *The Journal of Physical Chemistry C* **2015**, *119* (19), 10427-10438. DOI: 10.1021/acs.jpcc.5b01715.

(127) Corma, A.; Planelles, J.; Sánchez-Marín, J.; Tomás, F. The role of different types of acid site in the cracking of alkanes on zeolite catalysts. *Journal of Catalysis* **1985**, *93* (1), 30-37. DOI: https://doi.org/10.1016/0021-9517(85)90148-4.

(128) Degnan, T. F.; Chitnis, G. K.; Schipper, P. H. History of ZSM-5 fluid catalytic cracking additive development at Mobil. *Microporous and Mesoporous Materials* **2000**, *35-36*, 245-252. DOI: https://doi.org/10.1016/S1387-1811(99)00225-5.

(129) van Koningsveld, H.; Jansen, J. C.; van Bekkum, H. The orthorhombic/monoclinic transition in single crystals of zeolite ZSM-5. *Zeolites* **1987**, *7* (6), 564-568. DOI: https://doi.org/10.1016/0144-2449(87)90099-6.

(130) Ghorbanpour, A.; Rimer, J. D.; Grabow, L. C. Periodic, vdW-corrected density functional theory investigation of the effect of Al siting in H-ZSM-5 on chemisorption properties and site-specific acidity. *Catalysis Communications* **2014**, *52*, 98-102. DOI: https://doi.org/10.1016/j.catcom.2014.04.005.

(131) Knott, B. C.; Nimlos, C. T.; Robichaud, D. J.; Nimlos, M. R.; Kim, S.; Gounder, R. Consideration of the Aluminum Distribution in Zeolites in Theoretical and Experimental Catalysis Research. *ACS Catalysis* **2018**, *8* (2), 770-784. DOI: 10.1021/acscatal.7b03676.

(132) Sklenak, S.; Dědeček, J.; Li, C.; Wichterlová, B.; Gábová, V.; Sierka, M.; Sauer, J. Aluminum Siting in Silicon-Rich Zeolite Frameworks: A Combined High-Resolution 27Al NMR Spectroscopy and Quantum Mechanics/Molecular Mechanics Study of ZSM-5. *Angewandte Chemie International Edition* **2007**, *46* (38), 7286-7289.

(133) Vjunov, A.; Fulton, J. L.; Huthwelker, T.; Pin, S.; Mei, D.; Schenter, G. K.; Govind, N.; Camaioni, D. M.; Hu, J. Z.; Lercher, J. A. Quantitatively Probing the Al Distribution in Zeolites. *Journal of the American Chemical Society* **2014**, *136* (23), 8296-8306. DOI: 10.1021/ja501361v.

(134) van Bokhoven, J. A.; Lee, T.-L.; Drakopoulos, M.; Lamberti, C.; Thieß, S.; Zegenhagen, J. Determining the aluminium occupancy on the active T-sites in zeolites using X-ray standing waves. *Nature Materials* **2008**, *7* (7), 551-555. DOI: 10.1038/nmat2220.

(135) Bohinc, R.; Hoszowska, J.; Dousse, J. C.; Błachucki, W.; Zeeshan, F.; Kayser, Y.; Nachtegaal, M.; Pinar, A. B.; van Bokhoven, J. A. Distribution of aluminum over different T-sites in ferrierite zeolites studied with aluminum valence to core X-ray emission spectroscopy. *Physical Chemistry Chemical Physics* **2017**, *19* (43), 29271-29277, 10.1039/C7CP05001A.

(136) Perea, D. E.; Arslan, I.; Liu, J.; Ristanović, Z.; Kovarik, L.; Arey, B. W.; Lercher, J. A.; Bare, S. R.; Weckhuysen, B. M. Determining the location and nearest neighbours of aluminium in zeolites with atom probe tomography. *Nature Communications* **2015**, *6* (1), 7589. DOI: 10.1038/ncomms8589.

(137) Yokoi, T.; Mochizuki, H.; Namba, S.; Kondo, J. N.; Tatsumi, T. Control of the Al Distribution in the Framework of ZSM-5 Zeolite and Its Evaluation by Solid-State NMR Technique and Catalytic Properties. *The Journal of Physical Chemistry C* **2015**, *119* (27), 15303-15315. DOI: 10.1021/acs.jpcc.5b03289.

(138) Jones, A. J.; Carr, R. T.; Zones, S. I.; Iglesia, E. Acid strength and solvation in catalysis by MFI zeolites and effects of the identity, concentration and location of framework heteroatoms. *Journal of Catalysis* **2014**, *312*, 58-68.

(139) Nimlos, C. T.; Hoffman, A. J.; Hur, Y. G.; Lee, B. J.; Di Iorio, J. R.; Hibbitts, D. D.; Gounder, R. Experimental and Theoretical Assessments of Aluminum Proximity in MFI Zeolites and Its Alteration by Organic and Inorganic Structure-Directing Agents. *Chemistry of Materials* **2020**, *32* (21), 9277-9298. DOI: 10.1021/acs.chemmater.0c03154.

(140) Scanion, J. T.; Willis, D. E. Calculation of Flame Ionization Detector Relative Response Factors Using the Effective Carbon Number Concept. *J Chromatogr Sci* **1985**, *23* (8), 333-340.

(141) Cheng, W. K.; Summers, T.; Collings, N. The fast-response flame ionization detector. *Prog Energ Combust* **1998**, *24* (2), 89-124.

(142) Kester, P. M.; Miller, J. T.; Gounder, R. Ammonia Titration Methods To Quantify Bronsted Acid Sites in Zeolites Substituted with Aluminum and Boron Heteroatoms. *Ind Eng Chem Res* **2018**, *57* (19), 6673-6683.

(143) Hur, Y. G.; Kester, P. M.; Nimlos, C. T.; Cho, Y.; Miller, J. T.; Gounder, R. Influence of Tetrapropylammonium and Ethylenediamine Structure-Directing Agents on the Framework Al Distribution in B-Al-MFI Zeolites. *Ind Eng Chem Res* **2019**, *58* (27), 11849-11860.

(144) Jones, A. J.; Iglesia, E. Kinetic, Spectroscopic, and Theoretical Assessment of Associative and Dissociative Methanol Dehydration Routes in Zeolites. *Angewandte Chemie International Edition* **2014**, *53* (45), 12177-12181.

(145) McQuarrie, D. A. Statistical mechanics. **2000**. From http://worldcat.org /z-wcorg/.

Appendices

Appendix A: Supporting Information for Quantifying Effects of Active Site Proximity on Rates of Methanol Dehydration to Dimethyl Ether over CHA Zeolites through Microkinetic Modeling

Section A.1. Microkinetic Model Parameter Inputs and Simulation Outputs

Table A1: DFT-evaluated parameters for isolated sites, next-nearest neighbor (NNN) paired acid sites, and next-next-nearest neighbor (NNNN) paired acid sites in the 6-MR of CHA. Rate constants are presented evaluated at a temperature of 415 K. [a] Pre-exponential factors and rate constants for parameters with this note are in units of s^{-1}. [b] Pre-exponential factors and rate constants for parameters with this note are in units of Pa s^{-1}.

Parameter	A_{iso} (s^{-1}/Pa s^{-1})	$E_{a,iso}$ (kJ/mol)	$k_{iso}(T)$ (s^{-1}/Pa s^{-1})	$A_{pair,NNN}$ (s^{-1}/Pa s^{-1})	$E_{a,pair,NNN}$ (kJ/mol)	$k_{pair,NNN}(T)$ (s^{-1}/Pa s^{-1})	$A_{pair,NNNN}$ (s^{-1}/Pa s^{-1})	$E_{a,pair,NNNN}$ (kJ/mol)	$k_{pair,NNNN}(T)$ (s^{-1}/Pa s^{-1})
k_{mon}^{b}	$3.92 \cdot 10^{2}$	0	$3.92 \cdot 10^{2}$	$4.50 \cdot 10^{2}$	0	$4.50 \cdot 10^{2}$	$3.99 \cdot 10^{2}$	0	$3.99 \cdot 10^{2}$
k_{-mon}^{a}	$3.13 \cdot 10^{16}$	121.2	$1.75 \cdot 10^{1}$	$2.85 \cdot 10^{16}$	115.4	$8.49 \cdot 10^{1}$	$3.09 \cdot 10^{16}$	119.2	$3.08 \cdot 10^{1}$
k_{dim}^{b}	$6.38 \cdot 10^{2}$	0	$6.38 \cdot 10^{2}$	$3.61 \cdot 10^{2}$	0	$3.61 \cdot 10^{2}$	$1.12 \cdot 10^{3}$	0.0	$1.12 \cdot 10^{3}$
k_{-dim}^{a}	$2.26 \cdot 10^{16}$	81.4	$1.28 \cdot 10^{6}$	$3.30 \cdot 10^{16}$	80.1	$2.71 \cdot 10^{6}$	$1.55 \cdot 10^{16}$	91.2	$5.17 \cdot 10^{4}$
$k_{conc,dim}^{a}$	$8.64 \cdot 10^{12}$	137.0	$4.99 \cdot 10^{-5}$	$8.64 \cdot 10^{12}$	127.0	$9.01 \cdot 10^{-4}$	$8.64 \cdot 10^{12}$	134.6	$9.95 \cdot 10^{-5}$
$k_{-conc,dim}^{a}$	$8.64 \cdot 10^{12}$	113.5	$4.51 \cdot 10^{-2}$	$8.64 \cdot 10^{12}$	140.4	$1.83 \cdot 10^{-5}$	$8.64 \cdot 10^{12}$	130.0	$3.72 \cdot 10^{-4}$
$k_{h2o,des,dim}^{a}$	$2.38 \cdot 10^{15}$	30.6	$3.32 \cdot 10^{11}$	$5.21 \cdot 10^{15}$	66.0	$2.59 \cdot 10^{7}$	$8.28 \cdot 10^{15}$	70.0	$1.28 \cdot 10^{7}$
$k_{-h2o,des,dim}^{b}$	$1.87 \cdot 10^{4}$	0	$1.87 \cdot 10^{4}$	$5.77 \cdot 10^{3}$	0	$5.77 \cdot 10^{3}$	$2.88 \cdot 10^{3}$	0	$2.88 \cdot 10^{3}$
$k_{dme,des}^{a}$	$1.80 \cdot 10^{16}$	112.3	$1.32 \cdot 10^{2}$	$1.58 \cdot 10^{16}$	110.0	$2.26 \cdot 10^{2}$	$2.48 \cdot 10^{16}$	116.5	$5.38 \cdot 10^{1}$
$k_{-dme,des}^{b}$	$8.95 \cdot 10^{2}$	0	$8.95 \cdot 10^{2}$	$1.09 \cdot 10^{3}$	0	$1.09 \cdot 10^{3}$	$5.54 \cdot 10^{2}$	0	$5.54 \cdot 10^{2}$
k_{elim}^{a}	$8.64 \cdot 10^{12}$	129.5	$4.28 \cdot 10^{-4}$	$8.64 \cdot 10^{12}$	128.8	$5.30 \cdot 10^{-4}$	$8.64 \cdot 10^{12}$	131.8	$2.22 \cdot 10^{-4}$
k_{-elim}^{a}	$8.64 \cdot 10^{12}$	76.8	$1.84 \cdot 10^{3}$	$8.64 \cdot 10^{12}$	100.5	$1.93 \cdot 10^{0}$	$8.64 \cdot 10^{12}$	84.0	$2.34 \cdot 10^{2}$
$k_{h2o,des}^{a}$	$7.26 \cdot 10^{14}$	28.3	$1.97 \cdot 10^{11}$	$7.93 \cdot 10^{15}$	64.7	$5.74 \cdot 10^{7}$	$8.82 \cdot 10^{15}$	49.2	$5.65 \cdot 10^{9}$
$k_{-h2o,des}^{b}$	$1.11 \cdot 10^{5}$	0	$1.11 \cdot 10^{5}$	$3.07 \cdot 10^{3}$	0	$3.07 \cdot 10^{3}$	$2.62 \cdot 10^{3}$	0	$2.62 \cdot 10^{3}$
$k_{meoh,ads}^{b}$	$1.20 \cdot 10^{4}$	0	$1.20 \cdot 10^{4}$	$4.72 \cdot 10^{2}$	0	$4.72 \cdot 10^{2}$	$4.13 \cdot 10^{2}$	0	$4.13 \cdot 10^{2}$
$k_{-meoh,ads}^{a}$	$3.19 \cdot 10^{15}$	41.1	$2.13 \cdot 10^{10}$	$2.76 \cdot 10^{16}$	82.7	$1.08 \cdot 10^{6}$	$3.02 \cdot 10^{16}$	70.5	$4.08 \cdot 10^{7}$
k_{seq}^{a}	$8.64 \cdot 10^{12}$	77.5	$1.52 \cdot 10^{3}$	$8.64 \cdot 10^{12}$	94.9	$9.78 \cdot 10^{0}$	$8.64 \cdot 10^{12}$	76.6	$1.96 \cdot 10^{3}$
k_{-seq}^{a}	$8.64 \cdot 10^{12}$	138.1	$3.59 \cdot 10^{-5}$	$8.64 \cdot 10^{12}$	127.7	$7.37 \cdot 10^{-4}$	$8.64 \cdot 10^{12}$	125.0	$1.58 \cdot 10^{-3}$
k_{trim}^{b}	$1.37 \cdot 10^{3}$	0	$1.37 \cdot 10^{3}$	$1.66 \cdot 10^{3}$	0	$1.66 \cdot 10^{3}$	$5.89 \cdot 10^{2}$	0	$5.89 \cdot 10^{2}$
k_{-trim}^{a}	$1.18 \cdot 10^{16}$	75.0	$4.27 \cdot 10^{6}$	$1.20 \cdot 10^{16}$	74.5	$4.97 \cdot 10^{6}$	$2.38 \cdot 10^{16}$	89.2	$1.42 \cdot 10^{5}$
$k_{conc,trim}^{a}$	$8.64 \cdot 10^{12}$	120.5	$5.38 \cdot 10^{-3}$	$8.64 \cdot 10^{12}$	111.0	$9.22 \cdot 10^{-2}$	$8.64 \cdot 10^{12}$	140.9	$1.59 \cdot 10^{-5}$
$k_{-conc,trim}^{a}$	$8.64 \cdot 10^{12}$	76.8	$1.87 \cdot 10^{3}$	$8.64 \cdot 10^{12}$	99.2	$2.81 \cdot 10^{0}$	$8.64 \cdot 10^{12}$	110.6	$1.04 \cdot 10^{-1}$
$k_{h2o,des,trim}^{a}$	$4.49 \cdot 10^{15}$	12.7	$1.12 \cdot 10^{14}$	$8.59 \cdot 10^{15}$	40.8	$6.35 \cdot 10^{10}$	$8.59 \cdot 10^{15}$	40.8	$6.35 \cdot 10^{10}$
$k_{-h2o,des,trim}^{b}$	$7.21 \cdot 10^{3}$	0	$7.21 \cdot 10^{3}$	$2.72 \cdot 10^{3}$	0	$2.72 \cdot 10^{3}$	$2.72 \cdot 10^{3}$	0	$2.72 \cdot 10^{3}$
$k_{meoh,des,trim}^{a}$	$1.34 \cdot 10^{16}$	78.6	$1.72 \cdot 10^{6}$	$1.34 \cdot 10^{16}$	78.6	$1.72 \cdot 10^{6}$	$1.59 \cdot 10^{16}$	78.6	$2.03 \cdot 10^{6}$

$k_{-meoh,des,trim}$[b]	$1.39 \cdot 10^{3}$	0	$1.39 \cdot 10^{3}$	$1.39 \cdot 10^{3}$	0	$1.39 \cdot 10^{3}$	$1.08 \cdot 10^{3}$	0	$1.08 \cdot 10^{3}$
k_{tet}[b]	$1.22 \cdot 10^{3}$	0	$1.22 \cdot 10^{3}$	$5.72 \cdot 10^{2}$	0	$5.72 \cdot 10^{2}$	$4.87 \cdot 10^{2}$	0	$4.87 \cdot 10^{2}$
k_{-tet}[a]	$1.47 \cdot 10^{16}$	71.0	$1.70 \cdot 10^{7}$	$2.43 \cdot 10^{16}$	60	$6.81 \cdot 10^{8}$	$2.70 \cdot 10^{16}$	60.2	$7.21 \cdot 10^{8}$
$k_{conc,tet}$[a]	$8.64 \cdot 10^{12}$	146.0	$3.68 \cdot 10^{-6}$	$8.64 \cdot 10^{12}$	131.5	$2.46 \cdot 10^{-4}$	$8.64 \cdot 10^{12}$	122.8	$3.00 \cdot 10^{-3}$
$k_{-conc,tet}$[a]	$8.64 \cdot 10^{12}$	78.5	$1.14 \cdot 10^{3}$	$8.64 \cdot 10^{12}$	100.9	$1.72 \cdot 10^{0}$	$8.64 \cdot 10^{12}$	77.3	$1.61 \cdot 10^{3}$
$k_{h2o,des,tet}$[a]	$7.56 \cdot 10^{15}$	27.9	$2.30 \cdot 10^{12}$	$1.45 \cdot 10^{16}$	56.0	$1.31 \cdot 10^{9}$	$1.45 \cdot 10^{16}$	56.0	$1.31 \cdot 10^{9}$
$k_{-h2o,des,tet}$[b]	$3.30 \cdot 10^{3}$	0	$3.30 \cdot 10^{3}$	$1.24 \cdot 10^{3}$	0	$1.24 \cdot 10^{3}$	$1.24 \cdot 10^{3}$	0	$1.24 \cdot 10^{3}$
$k_{meoh,des,tet}$[a]	$1.37 \cdot 10^{16}$	35.8	$4.23 \cdot 10^{11}$	$1.37 \cdot 10^{16}$	35.8	$4.23 \cdot 10^{11}$	$1.37 \cdot 10^{16}$	35.8	$4.23 \cdot 10^{11}$
$k_{-meoh,des,tet}$[b]	$1.36 \cdot 10^{3}$	0	$1.36 \cdot 10^{3}$	$1.36 \cdot 10^{3}$	0	$1.36 \cdot 10^{3}$	$1.36 \cdot 10^{3}$	0	$1.36 \cdot 10^{3}$
k_{pent}[b]	$1.05 \cdot 10^{3}$	0	$1.05 \cdot 10^{3}$	$5.72 \cdot 10^{2}$	0	$5.72 \cdot 10^{2}$	$4.87 \cdot 10^{2}$	0.0	$4.87 \cdot 10^{2}$
k_{-pent}[a]	$1.62 \cdot 10^{16}$	71.0	$1.87 \cdot 10^{7}$	$2.43 \cdot 10^{16}$	60.0	$6.81 \cdot 10^{8}$	$2.70 \cdot 10^{16}$	60.2	$7.21 \cdot 10^{8}$

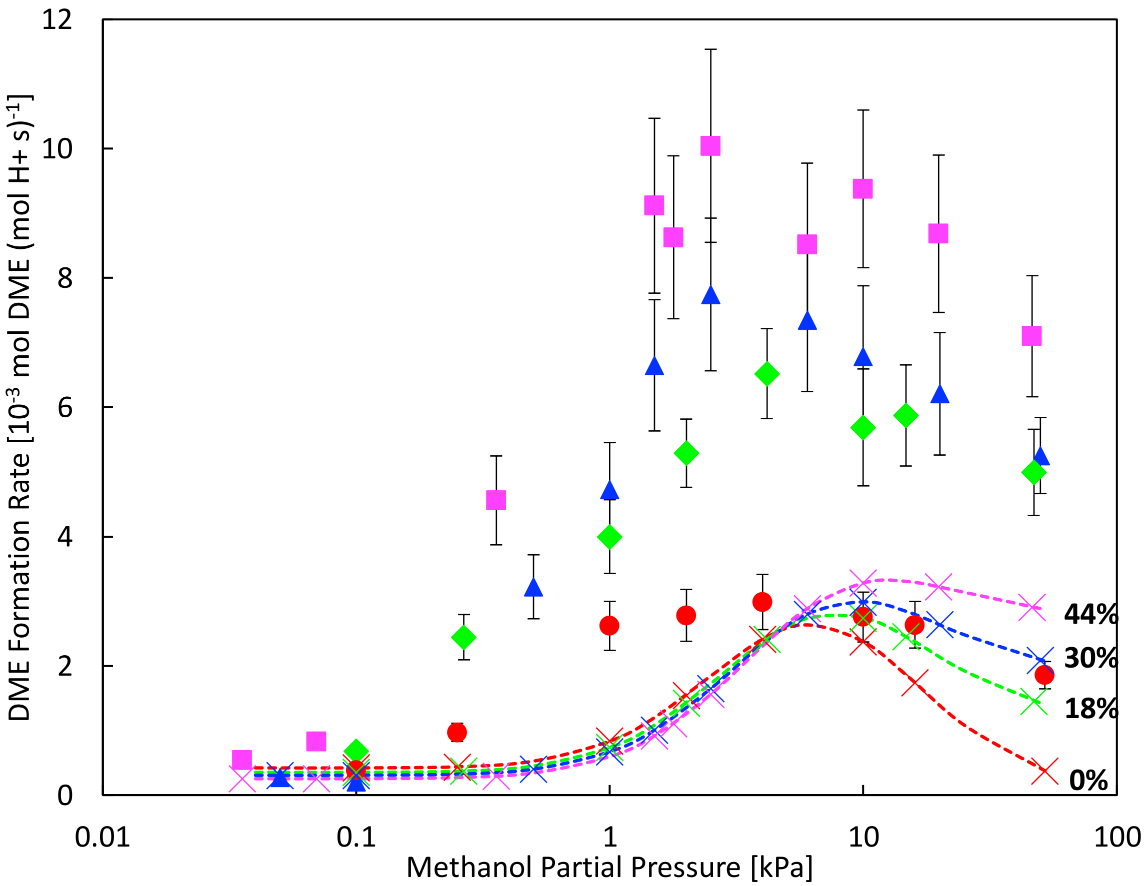

Figure A1: Comparison of model output and experimental values for the full range of MeOH partial pressures for untuned NNN DFT values, assuming a distribution of 7.4% NNN sites and 92.6% inactive NNNN sites, for 0% total paired acid sites (red, ●), 18% paired acid sites (green, ♦), 30% paired acid sites (blue, ▲), and 44% paired acid sites (pink, ■). Markers with error bars are the experimental data from Di Iorio, et al. [31] adjusted as described in Section S.2. The crosses identify the output of individual microkinetic model runs at the given paired acid site percentages at methanol partial pressures matching each experimental data point. The dashed lines connecting microkinetic model outputs are presented to guide the eye.

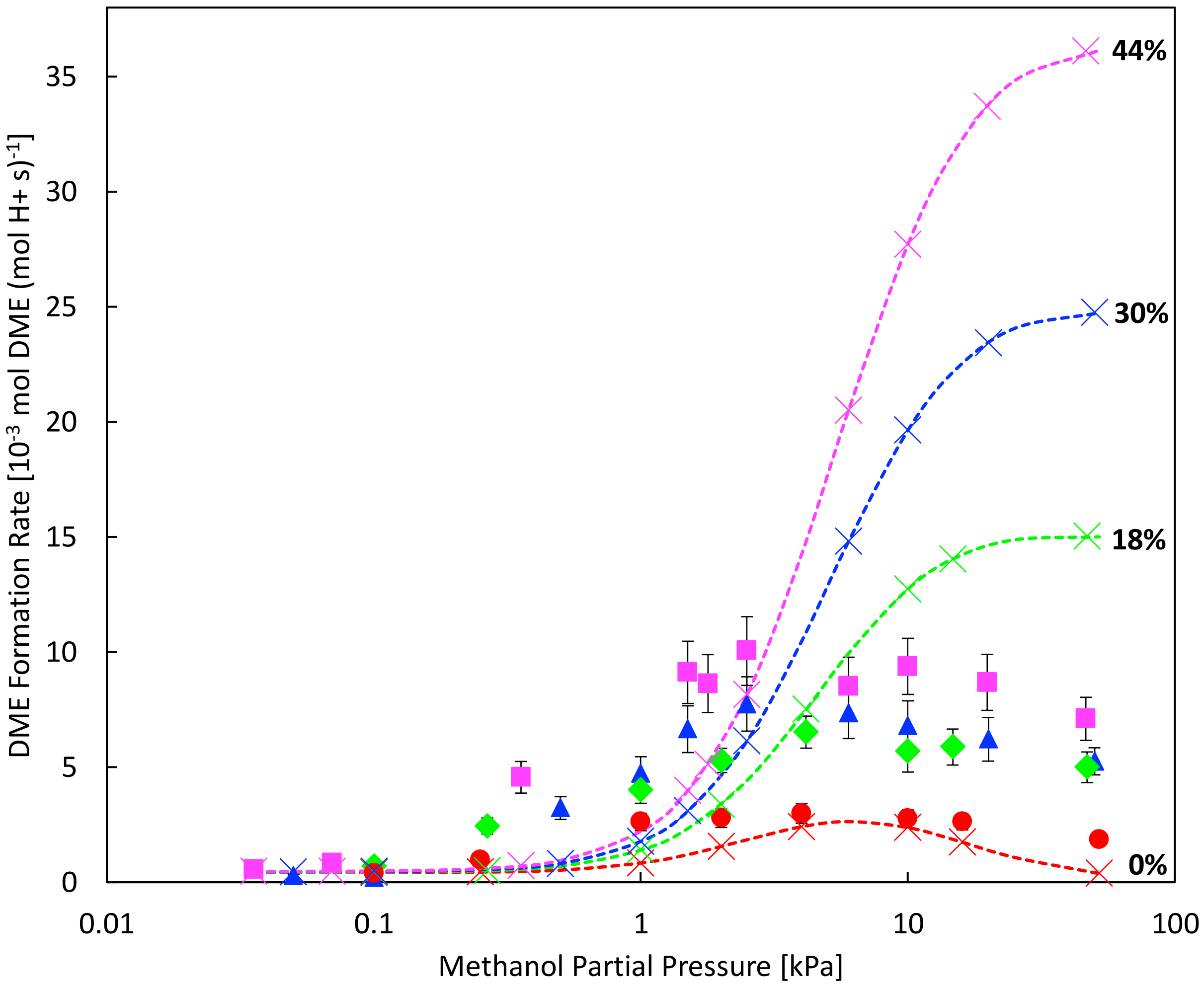

Figure A2: Comparison of model output and experimental values for the full range of MeOH partial pressures for untuned NNN DFT values, assuming a distribution of 100% NNN sites, for 0% total paired acid sites (red, ●), 18% paired acid sites (green, ♦), 30% paired acid sites (blue, ▲), and 44% paired acid sites (pink, ■). Markers with error bars are the experimental data from Di Iorio, et al. [31] adjusted as described in Section S.2. The crosses identify the output of individual microkinetic model runs at the given paired acid site percentages at methanol partial pressures matching each experimental data point. The dashed lines connecting microkinetic model outputs are presented to guide the eye.

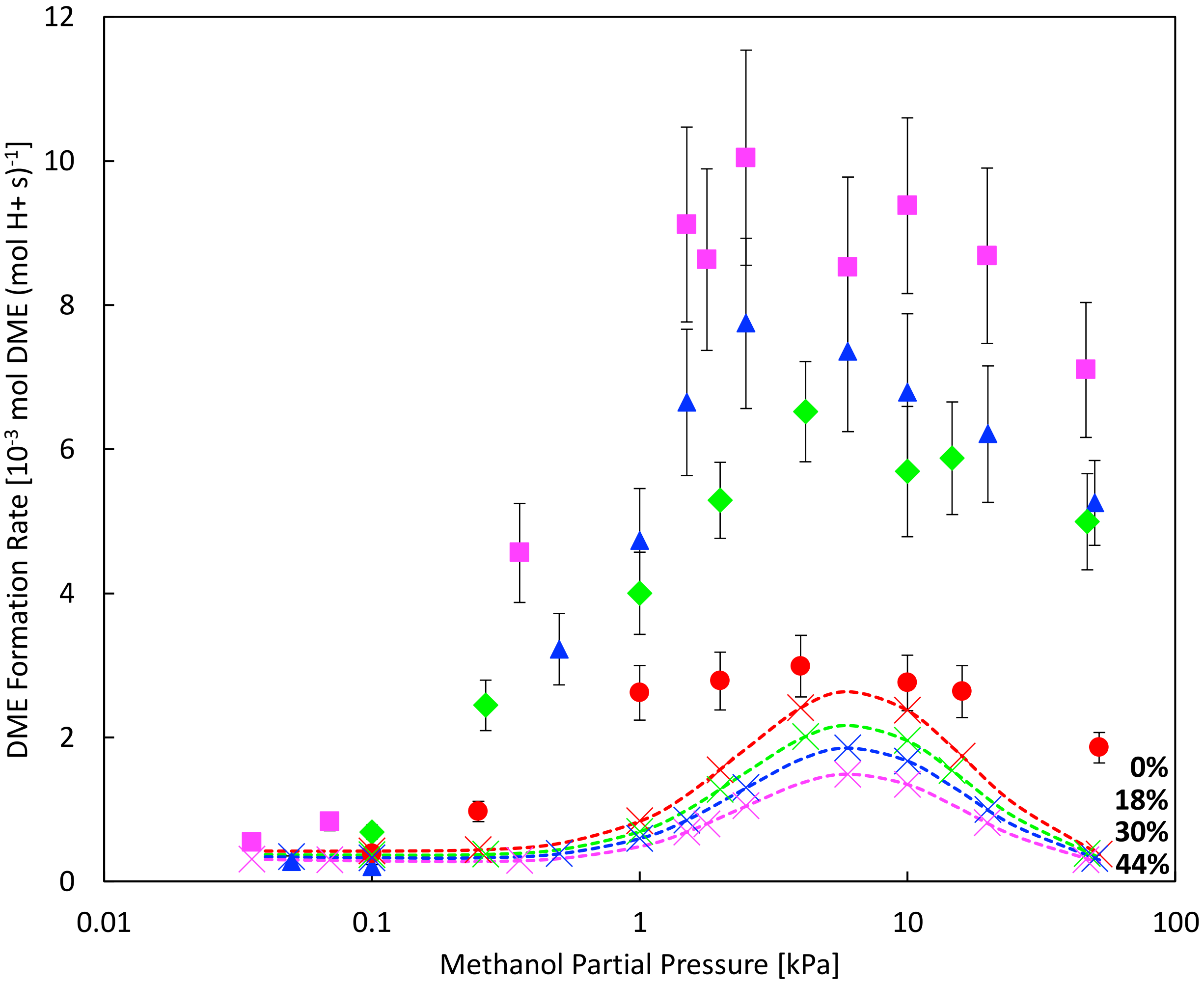

Figure A3: Comparison of model output and experimental values for the full range of MeOH partial pressures for untuned NNNN DFT values, assuming a distribution of 100% NNNN sites, for 0% total paired acid sites (red, ●), 18% paired acid sites (green, ♦), 30% paired acid sites (blue, ▲), and 44% paired acid sites (pink, ■). Markers with error bars are the experimental data from Di Iorio, et al. [31] adjusted as described in Section S.2. The crosses identify the output of individual microkinetic model runs at the given paired acid site percentages at methanol partial pressures matching each experimental data point. The dashed lines connecting microkinetic model outputs are presented to guide the eye.

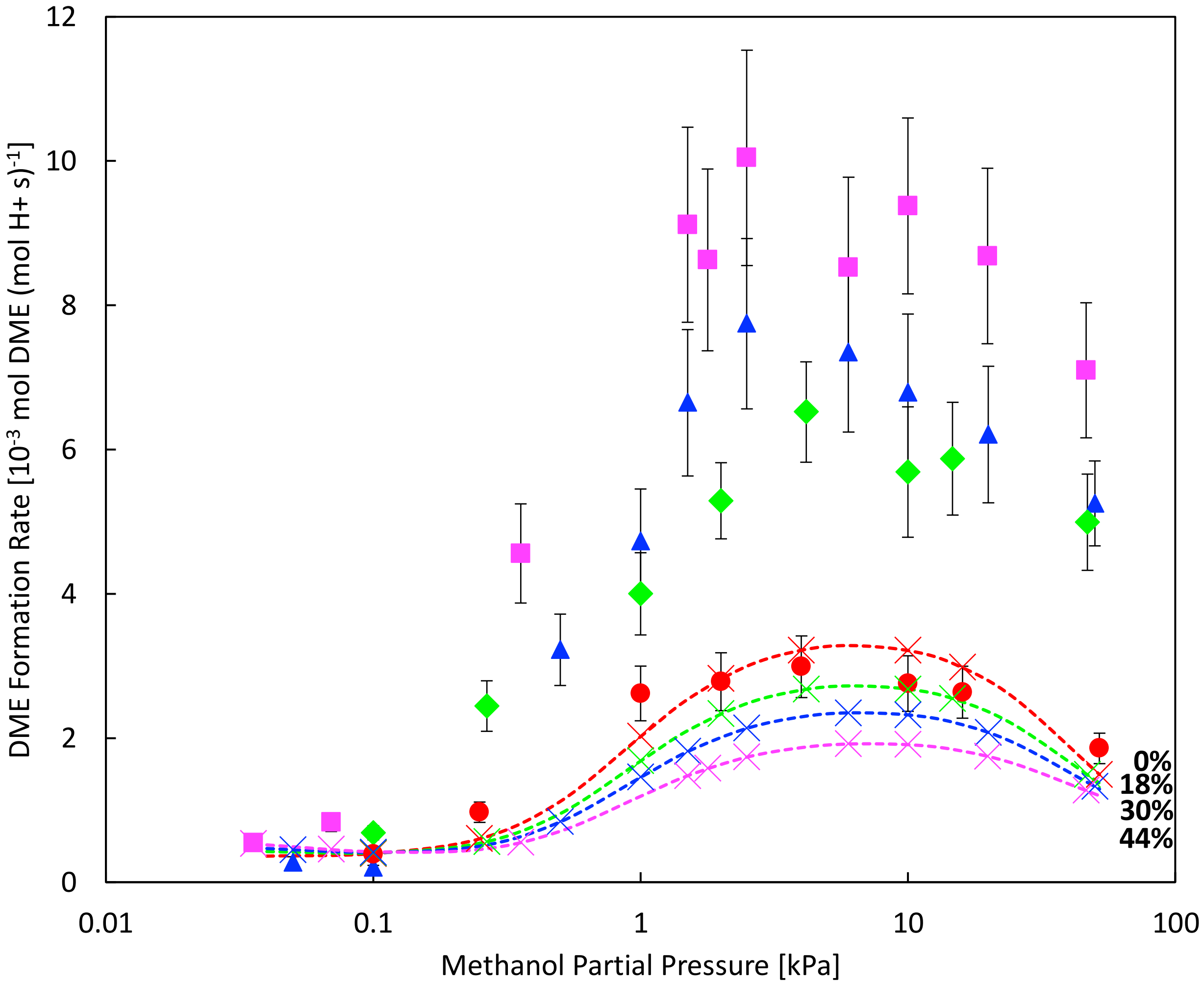

Figure A4: Comparison of model output and experimental values for the full range of MeOH partial pressures for maximally tuned NNNN DFT values, assuming a distribution of 100% NNNN sites, for 0% total paired acid sites (red, ●), 18% paired acid sites (green, ♦), 30% paired acid sites (blue, ▲), and 44% paired acid sites (pink, ■). Markers with error bars are the experimental data from Di Iorio, et al. [31] adjusted as described in Section S.2. The crosses identify the output of individual microkinetic model runs at the given paired acid site percentages at methanol partial pressures matching each experimental data point. The dashed lines connecting microkinetic model outputs are presented to guide the eye.

Table A2: DRC Sensitivity Coefficients for 0% paired acid site percentage. Values that round to 0.00 are red or dark orange depending on their original value, transitioning to yellow from 0.01 to 0.15, and eventually becoming green for values up to 1.00.

MeOH Partial Pressure (kPa)	iso,conc,dim	iso,elim	iso,seq	iso,conc,trim
0.04	0.00	0.96	0.01	0.02
0.1	0.00	0.87	0.01	0.12
0.25	0.01	0.53	0.00	0.46
0.5	0.01	0.22	0.00	0.77
1	0.00	0.07	0.00	0.93
1.5	0.00	0.03	0.00	0.97
2.5	0.00	0.01	0.00	0.99
4	0.00	0.00	0.00	0.99
6	0.00	0.00	0.00	1.00
10	0.00	0.00	0.00	1.00
15	0.00	0.00	0.00	1.00
25	0.00	0.00	0.00	1.00
50	0.00	0.00	0.00	1.00

Table A3: DRC Sensitivity Coefficients for 18% paired acid site percentage.

MeOH Partial Pressure (kPa)	iso,elim	iso,seq	iso,conc,trim	pair,dme,des	pair,elim	pair,conc,trim
0.04	0.86	0.01	0.02	0.00	0.09	0.01
0.1	0.76	0.00	0.11	0.00	0.08	0.04
0.25	0.42	0.00	0.37	0.00	0.05	0.14
0.5	0.16	0.00	0.56	0.00	0.02	0.25
1	0.04	0.00	0.57	0.00	0.01	0.37
1.5	0.02	0.00	0.54	0.00	0.00	0.44
2.5	0.01	0.00	0.49	0.00	0.00	0.50
4	0.00	0.00	0.47	0.00	0.00	0.53
6	0.00	0.00	0.45	0.00	0.00	0.54
10	0.00	0.00	0.44	0.01	0.00	0.56
15	0.00	0.00	0.42	0.01	0.00	0.57
25	0.00	0.00	0.40	0.01	0.00	0.58
50	0.00	0.00	0.37	0.02	0.00	0.61

Table A4: DRC Sensitivity Coefficients for 30% paired acid site percentage.

MeOH Partial Pressure (kPa)	iso,elim	iso,seq	iso,conc,trim	pair,dme,des	pair,elim	pair,conc,trim
0.04	0.79	0.01	0.02	0.00	0.16	0.01
0.1	0.68	0.00	0.10	0.00	0.15	0.06
0.25	0.36	0.00	0.31	0.00	0.09	0.23
0.5	0.12	0.00	0.44	0.00	0.04	0.39
1	0.03	0.00	0.42	0.00	0.01	0.53
1.5	0.01	0.00	0.38	0.00	0.01	0.60
2.5	0.00	0.00	0.34	0.00	0.00	0.66
4	0.00	0.00	0.31	0.00	0.00	0.68
6	0.00	0.00	0.30	0.00	0.00	0.70
10	0.00	0.00	0.28	0.01	0.00	0.71
15	0.00	0.00	0.27	0.01	0.00	0.72
25	0.00	0.00	0.26	0.02	0.00	0.73
50	0.00	0.00	0.23	0.03	0.00	0.74

Table A5: DRC Sensitivity Coefficients for 44% paired acid site percentage.

MeOH Partial Pressure (kPa)	iso,elim	iso,seq	iso,conc,trim	pair,dme,des	pair,elim	pair,conc,trim
0.04	0.69	0.01	0.02	0.00	0.26	0.02
0.1	0.58	0.00	0.08	0.00	0.23	0.10
0.25	0.28	0.00	0.25	0.00	0.12	0.33
0.5	0.09	0.00	0.32	0.00	0.05	0.53
1	0.02	0.00	0.29	0.00	0.02	0.67
1.5	0.01	0.00	0.25	0.00	0.01	0.73
2.5	0.00	0.00	0.22	0.00	0.00	0.77
4	0.00	0.00	0.20	0.00	0.00	0.80
6	0.00	0.00	0.19	0.01	0.00	0.81
10	0.00	0.00	0.18	0.01	0.00	0.81
15	0.00	0.00	0.17	0.01	0.00	0.82
25	0.00	0.00	0.16	0.02	0.00	0.82
50	0.00	0.00	0.14	0.03	0.00	0.83

Section A.2. Benchmarking Methanol Dehydration Turnover Rates and Kinetic Parameters using Commercial MFI Samples

Methanol dehydration turnover rates (per H^+) on two commercially sourced MFI samples (MFI(43,C) (CBV8014, Si/Al = 43, Zeolyst) and MFI(31,C) (CBV3024E, Si/Al = 31, Zeolyst) were previously measured at 433 K[31] and compared these values with turnover rates reported by Jones et al. at 433 K[138] in order to benchmark rate measurements. In a prior report[31], it was observed that dimethyl ether (DME) formation rates (per H^+) at 433 K were ~4x higher than those reported by Jones et al.[138], and these rates were calculated based on absolute response factors in the flame ionization detector (FID) in the gas chromatograph (GC) determined from direct injections of methane, methanol and DME standards into the heated GC inlet[31] (Table A6; “Prior work”). The FID was recently re-calibrated using methanol and DME response factors (relative to methane) determined by co-feeding methane along with methanol and DME standards at various concentrations via heated transfer lines into the GC sample valve (Table A6; “This work”), which resulted in relative RF values similar to those documented in the literature based on effective carbon number predictions (Table A6, “Literature”) [140, 141].

Table A6: Response factors (RF)[a] of DME and methanol (relative to methane) in the FID.

	Prior work[b]	**This work**	**Literature[140]**	**Literature[141]**
Dimethyl ether	0.88	1.20	1[3]	-
Methanol	2.49	0.95	0.5[3]	0.5, 0.75[4]

[a] RF = (area / mole fraction)$_{\text{component}}$ / (area / mole fraction)$_{\text{methane}}$

[b] Response factor used in [31, 40, 142, 143].

[3] Response factor calculated based on the contribution of different functional groups to the effective carbon number (ECN) of a compound reported in Table I of [140].

[4] Response factor listed in Appendix A of [141]. There are two response factors for methanol listed in this literature report.

With these new relative response factors, DME formation rates (per H^+) were re-measured at 433 K and 0–20 kPa CH_3OH on MFI(43,C) to be within ~1.8x of the rates measured at 433 K on MFI(43,C) by

Jones et al.[144] (Fig. A5). Rate data were measured between 393–456 K and fitted to a Langmuirian rate expression derived from the associative mechanism (Eq. A.1)[68] to estimate first-order and zero-order (in CH_3OH pressure) rate constants as a function of temperature.

$$\frac{r_{DME}}{[L]} = \frac{k_{first} P_{CH_3OH}}{1 + \frac{k_{first}}{k_{zero}} P_{CH_3OH}} \tag{A.1}$$

The Eyring equation was then used to estimate apparent activation enthalpies and entropies (Fig. A6), which are listed in Table S7 along with values reported by Di Iorio et al.[31] and Jones et al.[144] (Table A7). Activation enthalpies were identical, within experimental error, across all three reports. The differences in FID response factors between this work and Di Iorio et al.[31] led to more negative activation entropies estimated in this work (Table A7), and to activation Gibbs free energies that were within error of the values reported by Jones et al.[68]. These data indicate that methanol dehydration rates (433 K, per H^+) measured with the new FID response factors were adequately benchmarked to this prior literature report.[68] Thus, from re-analysis of the previous data and repeated measurements of these data, the experimental methanol dehydration rate and rate constant values reported in prior work[31, 40, 142, 143] should be divided by a factor of 3.6x before comparing to predictions of rates and rate constants from theoretical models.

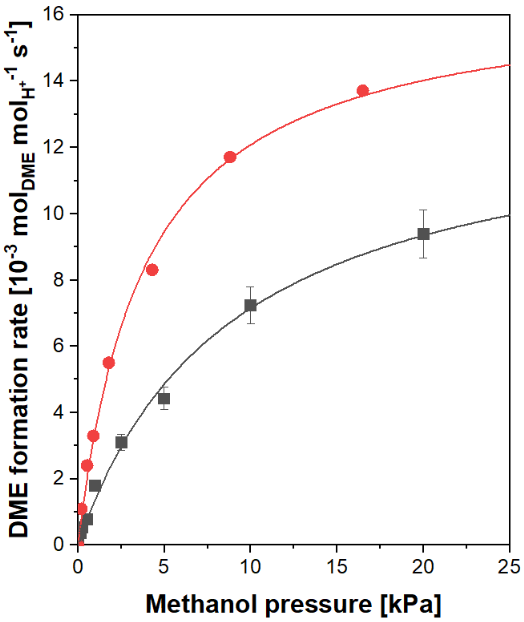

Figure A5: Methanol dehydration rates (per H^+) on MFI(43,C) measured at 433 K (black, ■) and rates reported by Jones et al. [144] (red, ●). Solid lines are regressions of the data to Eq. (A.1).

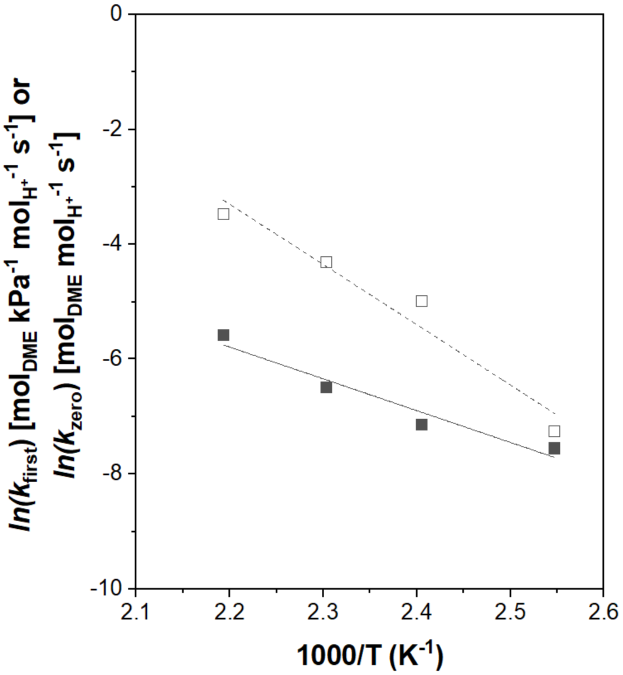

Figure A6: First-order (closed) and zero-order (open) methanol dehydration rate constants (per H^+) on MFI(43,C) measured as a function of temperature (393–456 K). Solid lines are regressions of the data to the Eyring equation.

Table A7: Activation parameters for first-order and zero-order kinetic regimes, with apparent Gibbs free energies at 433 K on MFI(43,C) measured in prior work[31], this work, and reported by Jones et al.[144].

	Di Iorio et al.[31]	**This work**	**Jones et al.[144]**
ΔH_{first} (kJ mol^{-1})	48 ± 5	46 ± 7	42 ±2
ΔH_{zero} (kJ mol^{-1})	93 ± 5	87 ± 14	90 ±2
ΔS_{first} (J mol^{-1} K^{-1})	-149 ± 8	-195 ± 33	-160 ±10
ΔS_{zero} (J mol^{-1} K^{-1})	-58 ± 7	-84 ± 16	-75 ±2
ΔG_{first} (kJ mol^{-1})	112 ± 10	130 ± 16	111 ±9
ΔG_{zero} (kJ mol^{-1})	119 ± 10	123 ± 15	123 ±3

Section A.3. Statistical Mechanics Formulas Used to Calculate *H, G,* and *S* values

Enthalpies (H), Gibb’s free energies (G), and entropies (S) are computed from DFT-derived vibrational frequencies using statistical mechanics as a sum of their constitutive vibrational, translational, and rotational parts with the corresponding zero-point vibrational energy (ZPVE) and electronic energy at 415 K:

$$H = E_0 + ZPVE + H_{vib} + H_{trans} + H_{rot} \tag{A.2}$$

$$G = E_0 + ZPVE + G_{vib} + G_{trans} + G_{rot} \tag{A.3}$$

Only adsorbates, protons, and AlO_4 tetrahedra were permitted to move during frequency calculations in zeolites and all motions of adsorbates were modeled as vibrations (i.e., translations and rotations were considered frustrated). The vibrational components—ZPVE, H_{vib}, and G_{vib}—were calculated as

$$ZPVE = \sum_i \left(\frac{1}{2} h\nu_i\right) \tag{A.4}$$

$$H_{vib} = \sum_i \frac{h\nu_i e^{-\frac{h\nu_i}{kT}}}{1-e^{-\frac{h\nu_i}{kt}}} \tag{A.5}$$

$$G_{vib} = \sum_i \left(-kT\ln\left(\frac{1}{1-e^{-\frac{h\nu_i}{kT}}}\right)\right) \tag{A.6}$$

Translational and rotational components were calculated for gas-phase species only, using similar formalisms:

$$H_{trans} = \frac{5}{2} kT \tag{A.7}$$

$$H_{rot,linear} = kT \tag{A.8}$$

$$H_{rot,nonlinear} = \frac{3}{2} kT \tag{A.9}$$

$$G_{trans} = -kT\ln\left(\left(\frac{2\pi mkT}{h^2}\right)^{\frac{3}{2}} V\right) \tag{A.10}$$

$$G_{rot} = -kT\ln\left(\frac{\pi^{\frac{1}{2}}}{\sigma}\left(\frac{T^3}{\theta_x\theta_y\theta_z}\right)^{\frac{1}{2}}\right) \tag{A.11}$$

$$\theta_i = \frac{h^2}{8\pi k I_i} \tag{A.12}$$

where I_i is the moment of inertia about the i axis (where $i = x, y, z$) and σ is the symmetry number of the species.[145]

Section A.4. DFT-calculated Methanol Cluster Structures

Table A8: The number of configurations tested for each respective cluster size on NNN and NNNN site pairs in this work.

Cluster size	**Number of configurations**	
	NNN site-pair	**NNNN site-pair**
2 CH_3OH	637	242
3 CH_3OH	443	242
4 CH_3OH	219	145
5 CH_3OH	328	286
6 CH_3OH	431	656
7 CH_3OH	398	1302
8 CH_3OH	483	1147
9 CH_3OH	482	1315
10 CH_3OH	486	378
11 CH_3OH	483	458
12 CH_3OH	642	435

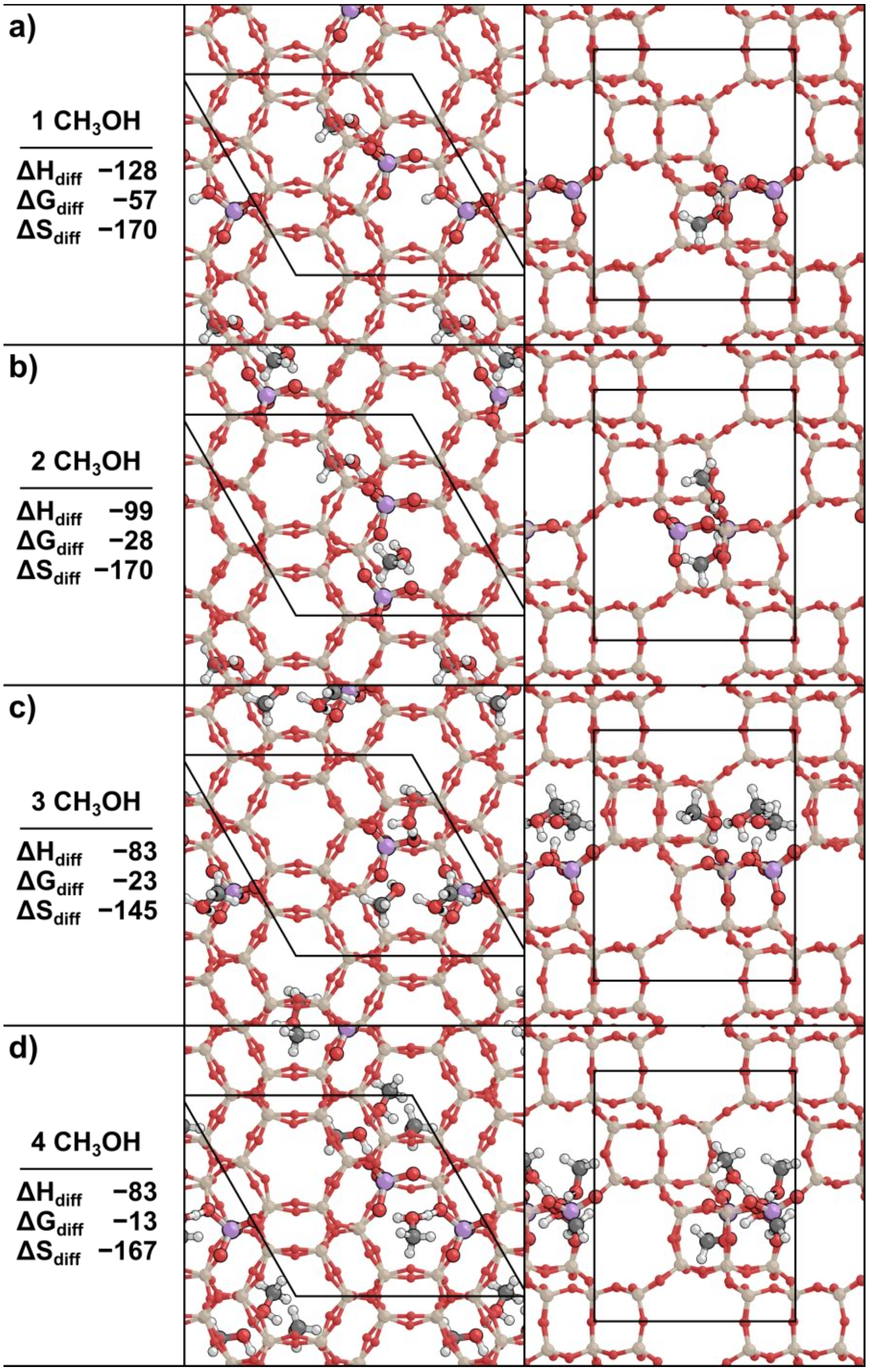

Figure A7: The most stable structure on the NNN site pair shown down the *c*-axis (left) and *b*-axis (right) of the CHA unit cell with (a) one ($\theta = 0.5$), (b) two ($\theta = 1.0$), (c) three ($\theta = 1.5$), and (d) four ($\theta = 2.0$) total methanol molecules adsorbed. Differential binding enthalpies (ΔH_{diff}) and free energies (ΔG_{diff}) are shown in kJ mol^{-1} and differential binding entropies (ΔS_{diff}) are shown in J mol^{-1} K^{-1}.

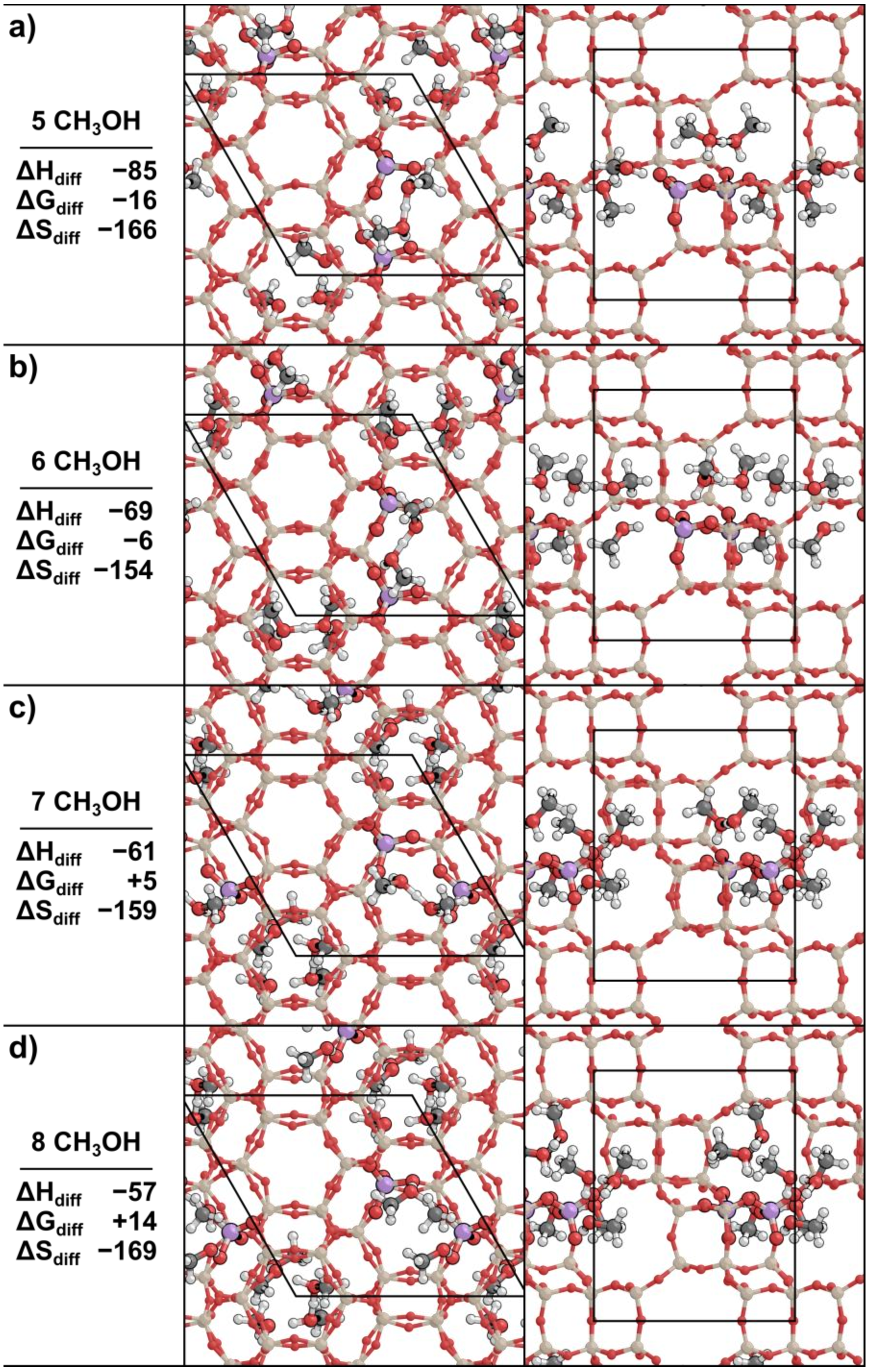

Figure A8: The most stable structure on the NNN site pair shown down the *c*-axis (left) and *b*-axis (right) of the CHA unit cell with (a) five (θ = 2.5), (b) six (θ = 3.0), (c) seven (θ = 3.5), and (d) eight (θ = 4.0) total methanol molecules adsorbed. Differential binding enthalpies (ΔH_{diff}) and free energies (ΔG_{diff}) are shown in kJ mol^{-1} and differential binding entropies (ΔS_{diff}) are shown in J mol^{-1} K^{-1}.

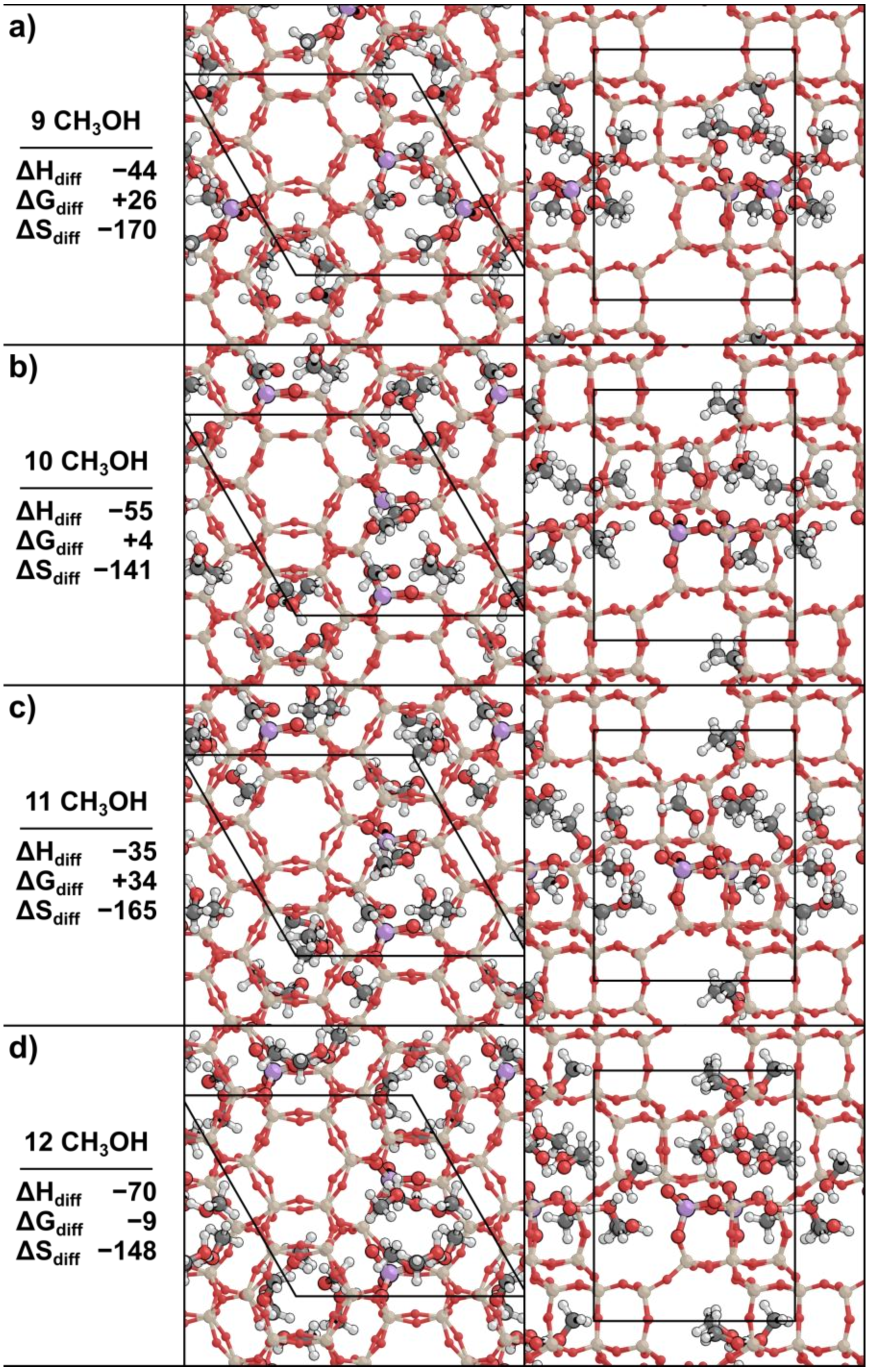

Figure A9: The most stable structure on the NNN site pair shown down the *c*-axis (left) and *b*-axis (right) of the CHA unit cell with (a) nine (θ = 4.5), (b) ten (θ = 5.0), (c) eleven (θ = 5.5), and (d) twelve (θ = 6.0) total methanol molecules adsorbed. Differential binding enthalpies (ΔH_{diff}) and free energies (ΔG_{diff}) are shown in kJ mol^{-1} and differential binding entropies (ΔS_{diff}) are shown in J mol^{-1} K^{-1}.

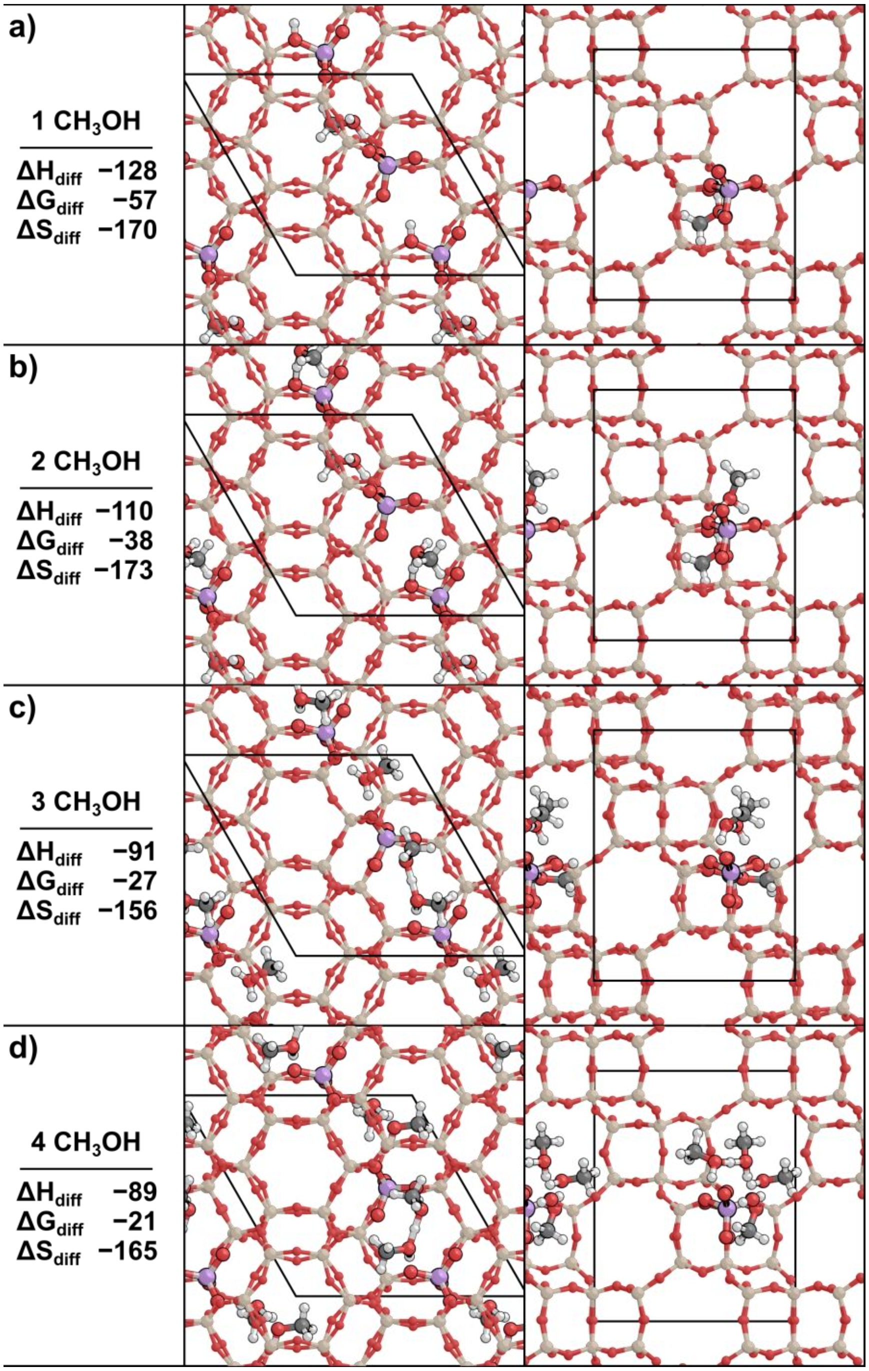

Figure A10: The most stable structure on the NNNN site pair shown down the *c*-axis (left) and *b*-axis (right) of the CHA unit cell with (a) one (θ = 0.5), (b) two (θ = 1.0), (c) three (θ = 1.5), and (d) four (θ = 2.0) total methanol molecules adsorbed. Differential binding enthalpies (ΔH_{diff}) and free energies (ΔG_{diff}) are shown in kJ mol^{-1} and differential binding entropies (ΔS_{diff}) are shown in J mol^{-1} K^{-1}.

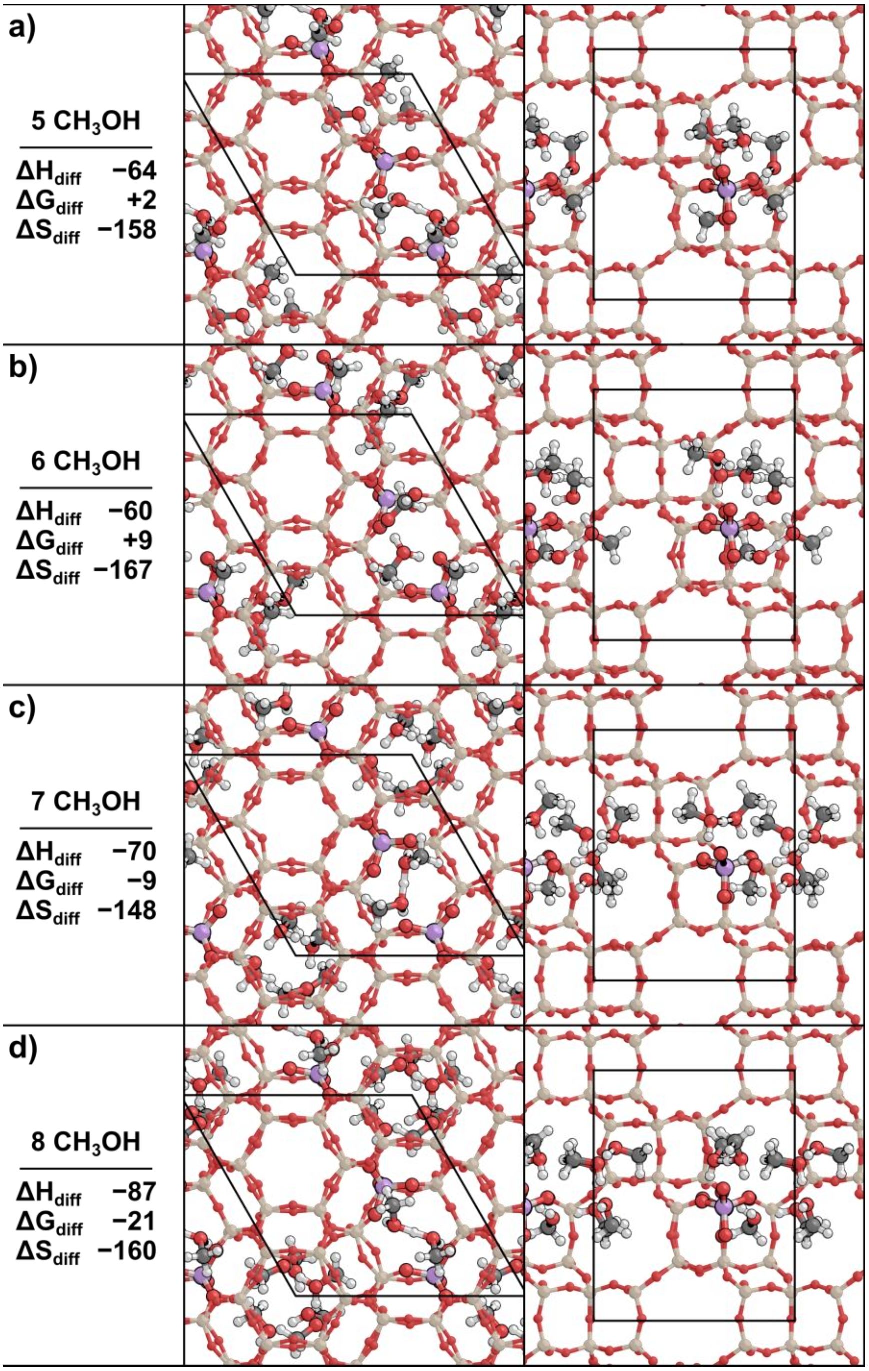

Figure A11: The most stable structure on the NNNN site pair shown down the *c*-axis (left) and *b*-axis (right) of the CHA unit cell with (a) five ($\theta = 2.5$), (b) six ($\theta = 3.0$), (c) seven ($\theta = 3.5$), and (d) eight ($\theta = 4.0$) total methanol molecules adsorbed. Differential binding enthalpies (ΔH_{diff}) and free energies (ΔG_{diff}) are shown in kJ mol^{-1} and differential binding entropies (ΔS_{diff}) are shown in J mol^{-1} K^{-1}.

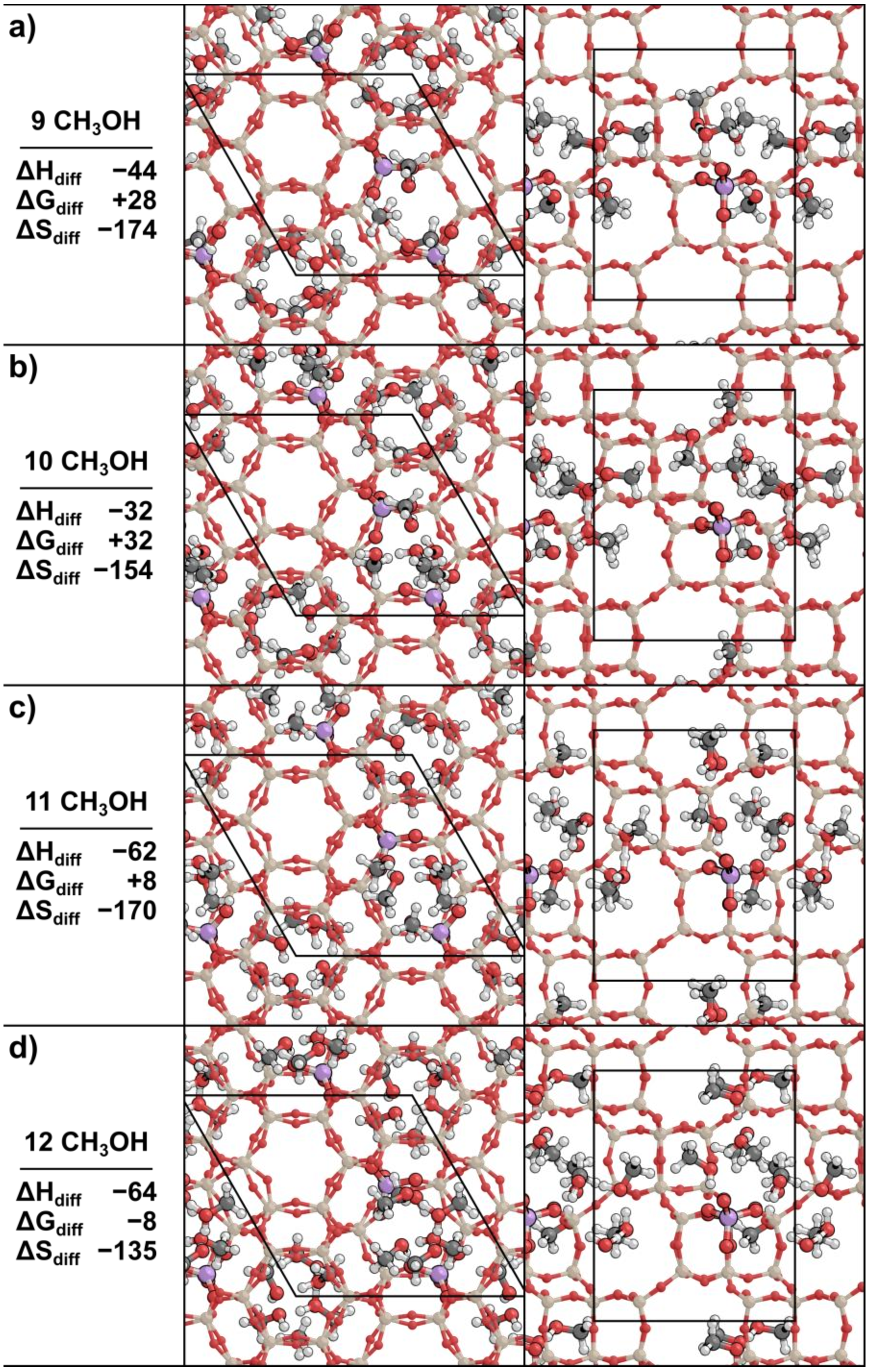

Figure A12: The most stable structure on the NNNN site pair shown down the *c*-axis (left) and *b*-axis (right) of the CHA unit cell with (a) nine (θ = 4.5), (b) ten (θ = 5.0), (c) eleven (θ = 5.5), and (d) twelve (θ = 6.0) total methanol molecules adsorbed. Differential binding enthalpies (ΔH_{diff}) and free energies (ΔG_{diff}) are shown in kJ mol^{-1} and differential binding entropies (ΔS_{diff}) are shown in J mol^{-1} K^{-1}.

Appendix B: Supporting Information for Evaluating the Impact of T-Site Location in the Conversion of Methanol to Dimethyl Ether within MFI Zeolites through Microkinetic Modeling

Section B.1. Reaction Coordinate Diagrams

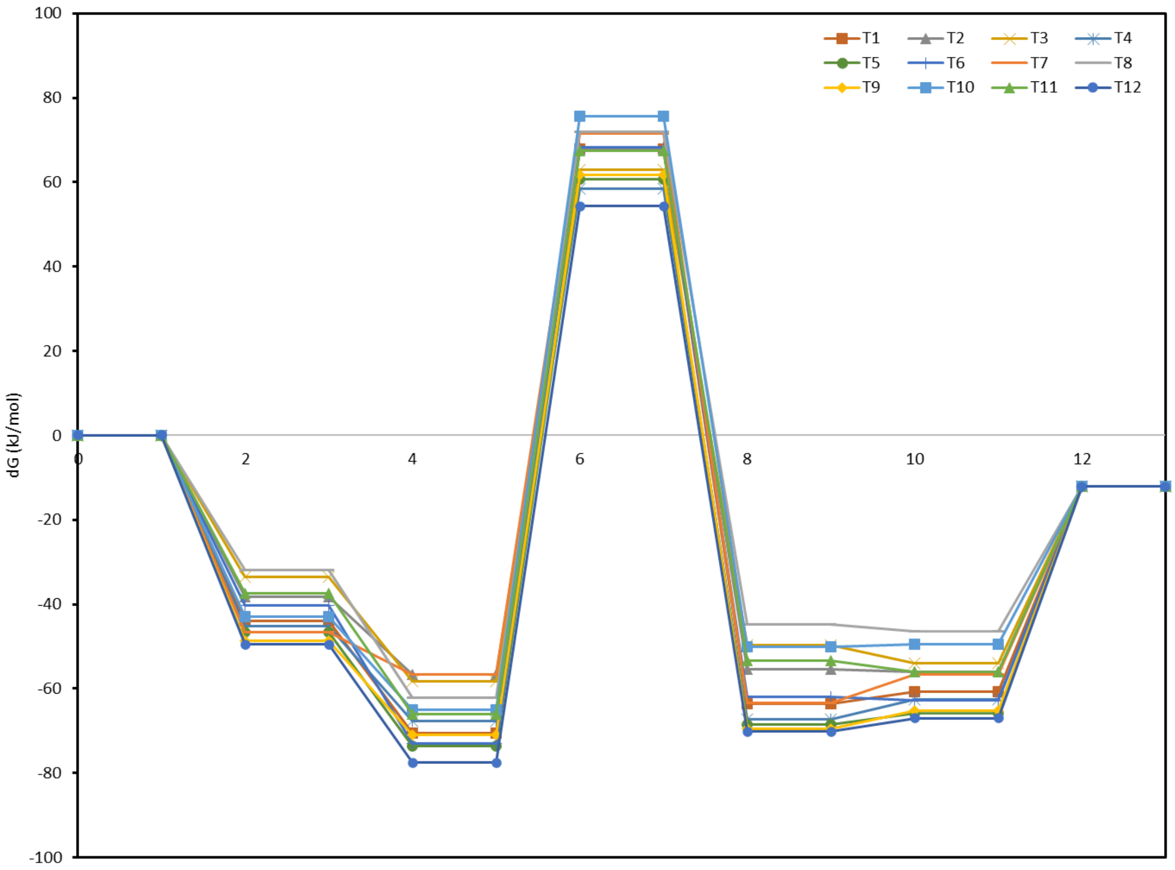

Figure B1. Reaction coordinate diagram for methanol dehydration to DME on MFI through the dimer pathway.

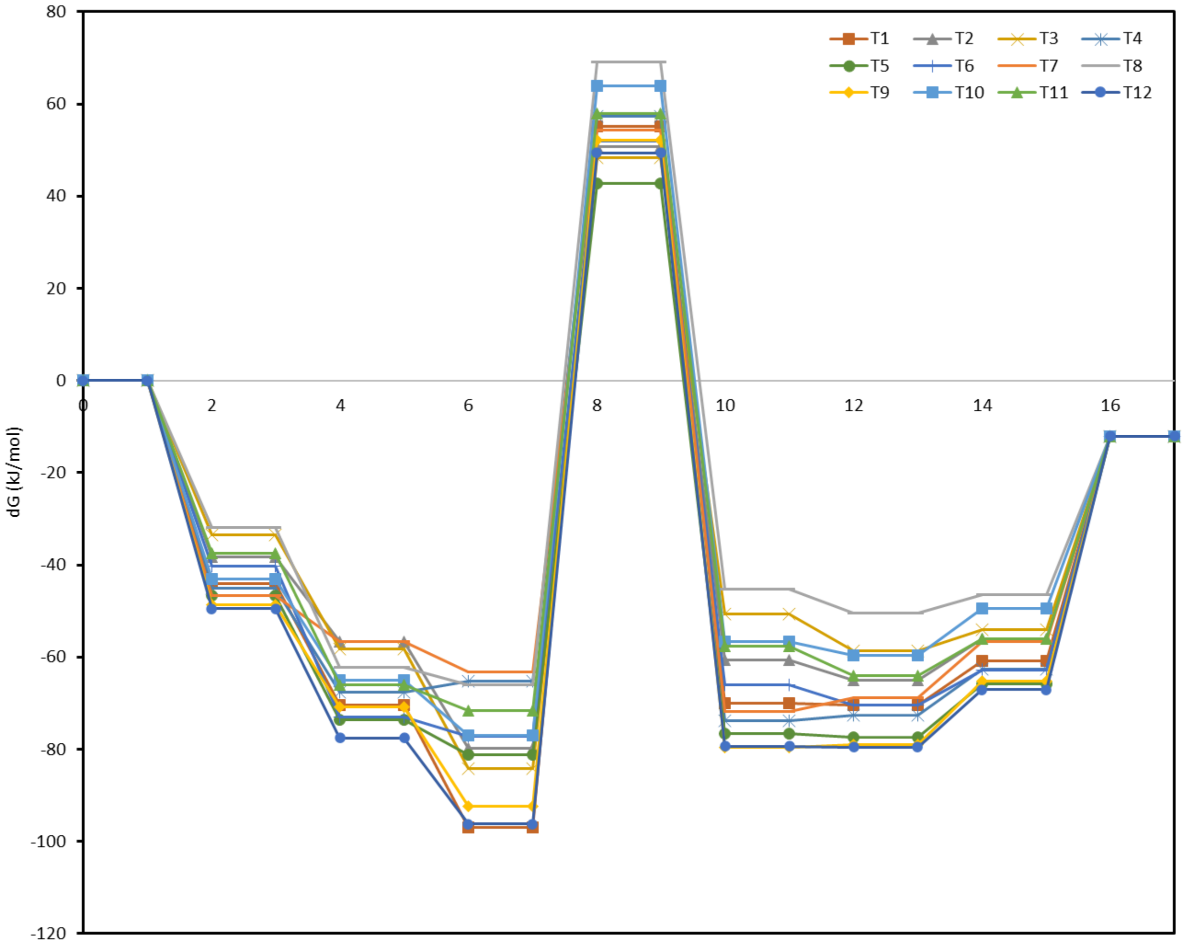

Figure B2. Reaction coordinate diagram for methanol dehydration to DME on MFI through the trimer pathway.

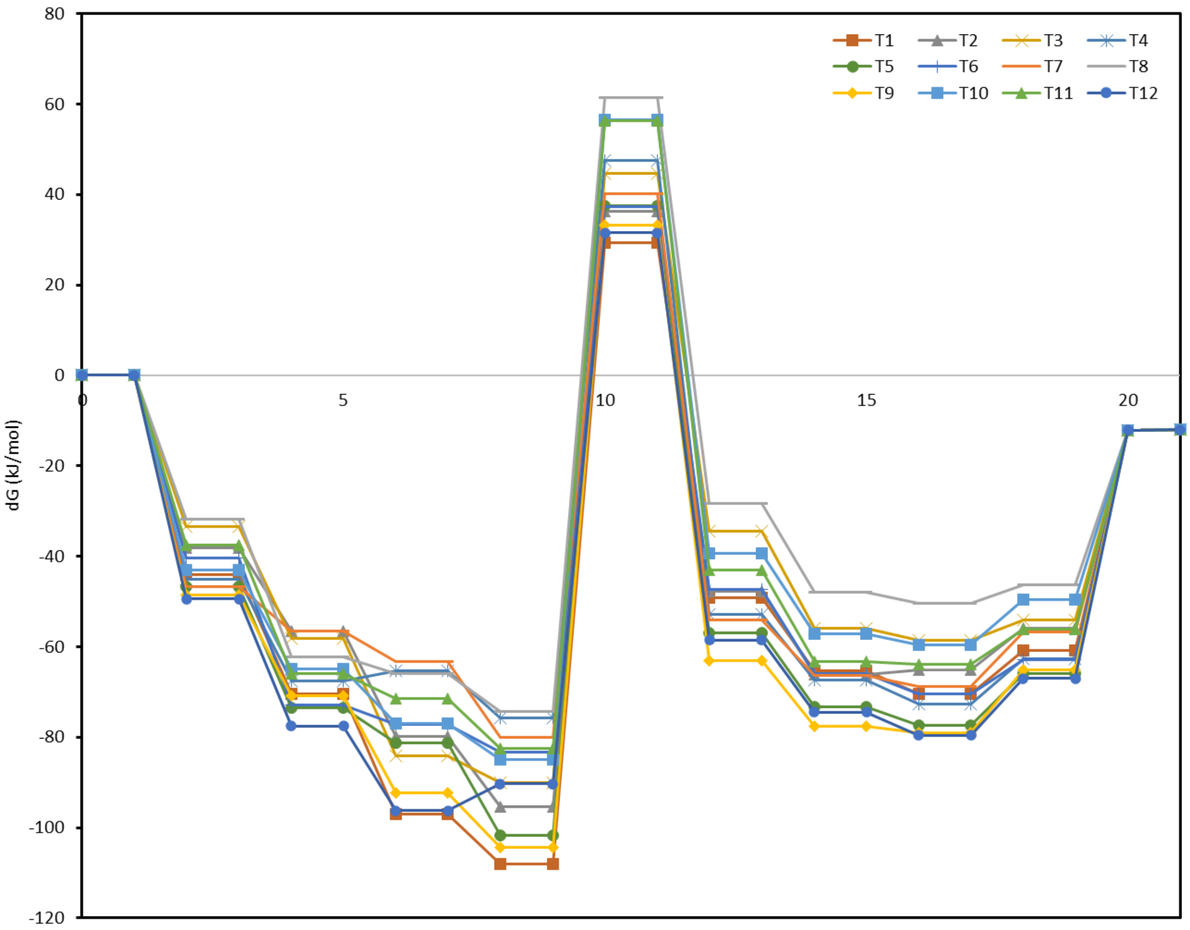

Figure B3. Reaction coordinate diagram for methanol dehydration to DME on MFI through the tetramer pathway.

Section B.2. Model Parameters

Table B1. Untuned model parameters. Pre-exponential factors are of units s^{-1} for unimolecular reactions and Pa^{-1} s^{-1} for bimolecular reactions. Activation energies are of units kJ/mol.

Parameter	**T1**	**T2**	**T3**	**T4**	**T5**	**T6**	**T7**	**T8**	**T9**	**T10**	**T11**	**T12**
A_mon_f	4.96E+02	1.76E+03	8.22E+02	4.64E+02	6.00E+02	5.71E+02	8.48E+02	8.33E+02	1.03E+03	8.53E+02	1.20E+03	4.96E+02
Ea_mon_f	0.00E+00	0.00E+00	0.00E+00	0.00E+00	0.00E+00	0.00E+00	0.00E+00	0.00E+00	0.00E+00	0.00E+00	0.00E+00	0.00E+00
A_mon_r	2.67E+16	1.15E+16	1.91E+16	2.79E+16	2.35E+16	2.43E+16	1.87E+16	1.89E+16	1.64E+16	1.86E+16	1.48E+16	2.67E+16
Ea_mon_r	1.13E+02	1.00E+02	1.00E+02	1.15E+02	1.15E+02	1.09E+02	1.13E+02	9.82E+01	1.14E+02	1.09E+02	1.02E+02	1.19E+02
A_dim_f	9.48E+02	5.76E+02	6.73E+02	1.59E+03	9.40E+02	1.20E+03	1.00E+03	7.88E+02	7.51E+02	1.15E+03	3.93E+02	7.62E+02
Ea_dim_f	0.00E+00	0.00E+00	0.00E+00	0.00E+00	0.00E+00	0.00E+00	0.00E+00	0.00E+00	0.00E+00	0.00E+00	0.00E+00	0.00E+00
A_dim_r	1.74E+16	2.42E+16	2.18E+16	1.23E+16	1.75E+16	1.48E+16	1.67E+16	1.96E+16	2.03E+16	1.53E+16	3.12E+16	2.01E+16
Ea_dim_r	9.21E+01	8.68E+01	9.23E+01	8.52E+01	9.26E+01	9.69E+01	7.52E+01	9.71E+01	8.92E+01	8.65E+01	9.91E+01	9.50E+01
A_conc,dim_f	2.06E+13	2.07E+13	1.43E+13	2.48E+13	1.92E+13	1.22E+13	1.84E+13	2.20E+13	1.64E+13	1.64E+13	1.13E+13	1.88E+13
Ea_conc,dim_f	1.38E+02	1.25E+02	1.21E+02	1.26E+02	1.34E+02	1.41E+02	1.28E+02	1.34E+02	1.33E+02	1.41E+02	1.33E+02	1.32E+02
A_conc,dim_r	8.44E+13	2.28E+10	3.39E+13	1.02E+14	7.30E+13	9.02E+13	1.25E+14	1.07E+14	8.64E+13	7.40E+13	8.23E+13	1.01E+14
Ea_conc,dim_r	1.32E+02	1.23E+02	9.90E+01	1.26E+02	1.29E+02	1.30E+02	1.35E+02	1.17E+02	1.31E+02	1.26E+02	1.21E+02	1.24E+02
A_h2o,des,dim_f	2.12E+15	1.55E+15	1.51E+15	1.71E+15	2.08E+15	1.52E+15	1.17E+15	1.70E+15	1.40E+15	1.87E+15	1.49E+15	2.34E+15
Ea_h2o,des,dim_f	5.04E+01	4.42E+01	4.02E+01	5.02E+01	4.99E+01	4.37E+01	4.90E+01	4.40E+01	4.82E+01	4.69E+01	4.18E+01	5.14E+01
A_h2o,des,dim_r	2.22E+04	3.57E+04	3.71E+04	3.06E+04	2.28E+04	3.65E+04	5.45E+04	3.08E+04	4.16E+04	2.69E+04	3.78E+04	1.91E+04
Ea_h2o,des,dim_r	0.00E+00	0.00E+00	0.00E+00	0.00E+00	0.00E+00	0.00E+00	0.00E+00	0.00E+00	0.00E+00	0.00E+00	0.00E+00	0.00E+00
A_dme,des_f	1.79E+16	6.24E+15	8.04E+15	1.63E+16	1.73E+16	1.07E+16	1.32E+16	1.49E+16	1.51E+16	1.13E+16	1.43E+16	1.42E+16
Ea_dme,des_f	1.14E+02	1.05E+02	1.01E+02	1.16E+02	1.19E+02	1.12E+02	1.08E+02	9.86E+01	1.17E+02	9.93E+01	1.08E+02	1.19E+02
A_dme,des_r	9.08E+02	4.40E+03	3.00E+03	1.04E+03	9.51E+02	1.96E+03	1.43E+03	1.19E+03	1.17E+03	1.80E+03	1.27E+03	1.29E+03
Ea_dme,des_r	0.00E+00	0.00E+00	0.00E+00	0.00E+00	0.00E+00	0.00E+00	0.00E+00	0.00E+00	0.00E+00	0.00E+00	0.00E+00	0.00E+00
A_trim_f	1.34E+03	1.14E+03	1.80E+03	1.11E+03	6.83E+02	1.04E+03	1.96E+03	1.03E+03	1.32E+03	1.58E+03	1.30E+03	1.65E+03
Ea_trim_f	0.00E+00	0.00E+00	0.00E+00	0.00E+00	0.00E+00	0.00E+00	0.00E+00	0.00E+00	0.00E+00	0.00E+00	0.00E+00	0.00E+00
A_trim_r	1.38E+16	1.54E+16	1.13E+16	1.56E+16	2.16E+16	1.64E+16	1.07E+16	1.64E+16	1.39E+16	1.23E+16	1.41E+16	1.20E+16
Ea_trim_r	9.01E+01	8.78E+01	8.79E+01	6.23E+01	7.51E+01	6.93E+01	6.81E+01	6.89E+01	8.52E+01	7.48E+01	6.94E+01	8.10E+01
A_elim_f	8.64E+12	8.64E+12	8.64E+12	8.64E+12	8.64E+12	8.64E+12	8.64E+12	8.64E+12	8.64E+12	8.64E+12	8.64E+12	8.64E+12
Ea_elim_f	1.30E+02	1.30E+02	1.30E+02	1.30E+02	1.30E+02	1.30E+02	1.30E+02	1.30E+02	1.30E+02	1.30E+02	1.30E+02	1.30E+02
A_elim_r	8.64E+12	8.64E+12	8.64E+12	8.64E+12	8.64E+12	8.64E+12	8.64E+12	8.64E+12	8.64E+12	8.64E+12	8.64E+12	8.64E+12
Ea_elim_r	7.68E+01	7.68E+01	7.68E+01	7.68E+01	7.68E+01	7.68E+01	7.68E+01	7.68E+01	7.68E+01	7.68E+01	7.68E+01	7.68E+01
A_h2o,des_f	7.26E+14	7.26E+14	7.26E+14	7.26E+14	7.26E+14	7.26E+14	7.26E+14	7.26E+14	7.26E+14	7.26E+14	7.26E+14	7.26E+14
Ea_h2o,des_f	2.83E+01	2.83E+01	2.83E+01	2.83E+01	2.83E+01	2.83E+01	2.83E+01	2.83E+01	2.83E+01	2.83E+01	2.83E+01	2.83E+01
A_h2o,des_r	1.11E+05	1.11E+05	1.11E+05	1.11E+05	1.11E+05	1.11E+05	1.11E+05	1.11E+05	1.11E+05	1.11E+05	1.11E+05	1.11E+05
Ea_h2o,des_r	0.00E+00	0.00E+00	0.00E+00	0.00E+00	0.00E+00	0.00E+00	0.00E+00	0.00E+00	0.00E+00	0.00E+00	0.00E+00	0.00E+00
A_meoh,ads_f	1.20E+04	1.20E+04	1.20E+04	1.20E+04	1.20E+04	1.20E+04	1.20E+04	1.20E+04	1.20E+04	1.20E+04	1.20E+04	1.20E+04
Ea_meoh,ads_f	0.00E+00	0.00E+00	0.00E+00	0.00E+00	0.00E+00	0.00E+00	0.00E+00	0.00E+00	0.00E+00	0.00E+00	0.00E+00	0.00E+00
A_meoh,ads_r	3.19E+15	3.19E+15	3.19E+15	3.19E+15	3.19E+15	3.19E+15	3.19E+15	3.19E+15	3.19E+15	3.19E+15	3.19E+15	3.19E+15
Ea_meoh,ads_r	4.11E+01	4.11E+01	4.11E+01	4.11E+01	4.11E+01	4.11E+01	4.11E+01	4.11E+01	4.11E+01	4.11E+01	4.11E+01	4.11E+01

A_seq_f	8.64E+12	8.64E+12	8.64E+12	8.64E+12	8.64E+12	8.64E+12	8.64E+12	8.64E+12	8.64E+12	8.64E+12	8.64E+12	8.64E+12
Ea_seq_f	7.75E+01	7.75E+01	7.75E+01	7.75E+01	7.75E+01	7.75E+01	7.75E+01	7.75E+01	7.75E+01	7.75E+01	7.75E+01	7.75E+01
A_seq_r	8.64E+12	8.64E+12	8.64E+12	8.64E+12	8.64E+12	8.64E+12	8.64E+12	8.64E+12	8.64E+12	8.64E+12	8.64E+12	8.64E+12
Ea_seq_r	1.38E+02	1.38E+02	1.38E+02	1.38E+02	1.38E+02	1.38E+02	1.38E+02	1.38E+02	1.38E+02	1.38E+02	1.38E+02	1.38E+02
A_conc,trim_f	1.28E+13	1.75E+13	2.07E+13	2.95E+13	1.28E+13	1.46E+13	1.60E+13	1.86E+13	2.10E+13	1.86E+13	1.25E+13	2.52E+13
Ea_conc,trim_f	1.52E+02	1.31E+02	1.32E+02	1.23E+02	1.24E+02	1.29E+02	1.18E+02	1.35E+02	1.45E+02	1.41E+02	1.29E+02	1.46E+02
A_conc,trim_r	1.20E+14	5.13E+14	5.74E+14	3.00E+14	1.97E+14	3.07E+14	2.56E+14	3.34E+14	3.87E+14	2.32E+14	3.54E+14	2.71E+14
Ea_conc,trim_r	1.25E+02	1.11E+02	9.90E+01	1.31E+02	1.19E+02	1.18E+02	1.26E+02	1.14E+02	1.32E+02	1.21E+02	1.16E+02	1.29E+02
A_h2o,des,trim_f	3.12E+15	2.40E+15	2.29E+15	2.54E+15	3.08E+15	2.28E+15	1.80E+15	2.57E+15	2.14E+15	2.81E+15	2.29E+15	3.42E+15
Ea_h2o,des,trim_f	5.04E+01	4.42E+01	4.02E+01	5.02E+01	4.99E+01	4.37E+01	4.90E+01	4.40E+01	4.82E+01	4.69E+01	4.18E+01	5.14E+01
A_h2o,des,trim_r	1.25E+04	1.84E+04	1.98E+04	1.69E+04	1.27E+04	1.99E+04	2.85E+04	1.66E+04	2.18E+04	1.46E+04	1.98E+04	1.08E+04
Ea_h2o,des,trim_r	0.00E+00	0.00E+00	0.00E+00	0.00E+00	0.00E+00	0.00E+00	0.00E+00	0.00E+00	0.00E+00	0.00E+00	0.00E+00	0.00E+00
A_meoh,des,trim_f	4.08E+15	1.88E+15	3.08E+15	4.27E+15	3.62E+15	3.83E+15	2.95E+15	2.96E+15	2.58E+15	2.96E+15	2.36E+15	4.12E+15
Ea_meoh,des,trim_f	6.27E+01	5.55E+01	5.53E+01	6.35E+01	6.36E+01	6.02E+01	6.25E+01	5.43E+01	6.29E+01	6.04E+01	5.63E+01	6.57E+01
A_meoh,des,trim_r	8.33E+03	2.67E+04	1.27E+04	7.76E+03	9.96E+03	9.16E+03	1.35E+04	1.34E+04	1.65E+04	1.35E+04	1.90E+04	8.19E+03
Ea_meoh,des,trim_r	0.00E+00	0.00E+00	0.00E+00	0.00E+00	0.00E+00	0.00E+00	0.00E+00	0.00E+00	0.00E+00	0.00E+00	0.00E+00	0.00E+00
A_tet_f	6.86E+02	2.30E+03	1.63E+03	1.31E+03	2.05E+03	2.15E+03	7.63E+02	2.67E+03	1.00E+03	1.87E+03	1.73E+03	7.39E+02
Ea_tet_f	0.00E+00	0.00E+00	0.00E+00	0.00E+00	0.00E+00	0.00E+00	0.00E+00	0.00E+00	0.00E+00	0.00E+00	0.00E+00	0.00E+00
A_tet_r	2.15E+16	9.63E+15	1.21E+16	1.40E+16	1.04E+16	1.01E+16	2.01E+16	8.69E+15	1.67E+16	1.10E+16	1.16E+16	2.05E+16
Ea_tet_r	7.84E+01	7.60E+01	6.84E+01	7.41E+01	8.17E+01	6.71E+01	8.35E+01	6.80E+01	7.73E+01	6.96E+01	7.32E+01	6.12E+01
A_conc,tet_f	7.43E+12	3.87E+12	2.74E+13	1.31E+13	2.68E+13	1.72E+13	1.47E+13	1.80E+13	1.34E+13	1.76E+13	1.35E+13	1.79E+13
Ea_conc,tet_f	1.37E+02	1.32E+02	1.35E+02	1.23E+02	1.39E+02	1.21E+02	1.20E+02	1.36E+02	1.38E+02	1.41E+02	1.39E+02	1.22E+02
A_conc,tet_r	1.23E+14	8.23E+14	1.02E+15	1.47E+14	3.92E+14	3.25E+14	5.33E+14	3.13E+14	5.28E+14	2.75E+14	6.22E+14	3.23E+14
Ea_conc,tet_r	7.85E+01	8.40E+01	7.92E+01	1.00E+02	9.45E+01	8.47E+01	9.43E+01	8.99E+01	9.64E+01	9.59E+01	9.95E+01	9.00E+01
A_h2o,des,tet_f	6.56E+15	4.74E+15	4.56E+15	5.33E+15	6.44E+15	4.67E+15	3.66E+15	5.28E+15	4.37E+15	5.69E+15	4.63E+15	7.13E+15
Ea_h2o,des,tet_f	4.11E+01	3.60E+01	3.28E+01	4.10E+01	4.07E+01	3.56E+01	4.00E+01	3.59E+01	3.94E+01	3.83E+01	3.41E+01	4.19E+01
A_h2o,des,tet_r	4.08E+03	6.64E+03	7.03E+03	5.57E+03	4.19E+03	6.79E+03	9.78E+03	5.65E+03	7.50E+03	5.06E+03	6.87E+03	3.60E+03
Ea_h2o,des,tet_r	0.00E+00	0.00E+00	0.00E+00	0.00E+00	0.00E+00	0.00E+00	0.00E+00	0.00E+00	0.00E+00	0.00E+00	0.00E+00	0.00E+00
A_meoh,des,tet_f	5.80E+15	2.89E+15	4.52E+15	6.05E+15	5.21E+15	5.49E+15	4.33E+15	4.35E+15	3.85E+15	4.35E+15	3.54E+15	5.86E+15
Ea_meoh,des,tet_f	5.12E+01	5.12E+01	5.12E+01	5.12E+01	5.12E+01	5.12E+01	5.12E+01	5.12E+01	5.12E+01	5.12E+01	5.12E+01	5.12E+01
A_meoh,des,tet_r	4.91E+03	1.40E+04	7.14E+03	4.61E+03	5.76E+03	5.34E+03	7.60E+03	7.55E+03	9.09E+03	7.55E+03	1.03E+04	4.83E+03
Ea_meoh,des,tet_r	0.00E+00	0.00E+00	0.00E+00	0.00E+00	0.00E+00	0.00E+00	0.00E+00	0.00E+00	0.00E+00	0.00E+00	0.00E+00	0.00E+00
A_pent_f	8.09E+02	2.12E+02	7.08E+02	1.21E+03	3.84E+02	6.64E+02	8.39E+02	5.26E+02	7.91E+02	2.43E+02	3.44E+03	2.51E+02
Ea_pent_f	0.00E+00	0.00E+00	0.00E+00	0.00E+00	0.00E+00	0.00E+00	0.00E+00	0.00E+00	0.00E+00	0.00E+00	0.00E+00	0.00E+00
A_pent_r	1.93E+16	4.72E+16	2.11E+16	1.47E+16	3.17E+16	2.20E+16	1.88E+16	2.57E+16	1.96E+16	4.30E+16	7.34E+15	4.21E+16
Ea_pent_r	5.54E+01	6.23E+01	6.44E+01	6.06E+01	6.15E+01	8.02E+01	6.88E+01	6.52E+01	5.90E+01	6.49E+01	4.96E+01	6.31E+01

Table B2. Tuning Applied to Model Parameters. All tuning is applied uniformly to all 12 T-sites. Pre-exponential factors are of units s^{-1} for unimolecular reactions and Pa^{-1} s^{-1} for bimolecular reactions. Activation energies are of units kJ/mol.

Parameter	Change	T1	T2	T3	T4	T5	T6	T7	T8	T9	T10	T11	T12
A_mon_f	*10	4.96E+03	1.76E+04	8.22E+03	4.64E+03	6.00E+03	5.71E+03	8.48E+03	8.33E+03	1.03E+04	8.53E+03	1.20E+04	4.96E+03
A_mon_r	*0.25	6.68E+15	2.87E+15	4.77E+15	6.98E+15	5.88E+15	6.08E+15	4.67E+15	4.73E+15	4.10E+15	4.66E+15	3.71E+15	6.68E+15
Ea_mon_r	+6	1.19E+02	1.06E+02	1.06E+02	1.21E+02	1.21E+02	1.15E+02	1.19E+02	1.04E+02	1.20E+02	1.15E+02	1.08E+02	1.25E+02
A_dim_f	*10	9.48E+03	5.76E+03	6.73E+03	1.59E+04	9.40E+03	1.20E+04	1.00E+04	7.88E+03	7.51E+03	1.15E+04	3.93E+03	7.62E+03
A_dim_r	*0.25	4.34E+15	6.05E+15	5.45E+15	3.08E+15	4.36E+15	3.71E+15	4.18E+15	4.91E+15	5.07E+15	3.82E+15	7.81E+15	5.02E+15
Ea_dim_r	+6	9.81E+01	9.28E+01	9.83E+01	9.12E+01	9.86E+01	1.03E+02	8.12E+01	1.03E+02	9.52E+01	9.25E+01	1.05E+02	1.01E+02
A_trim_f	*10	1.34E+04	1.14E+04	1.80E+04	1.11E+04	6.83E+03	1.04E+04	1.96E+04	1.03E+04	1.32E+04	1.58E+04	1.30E+04	1.65E+04
A_trim_r	*0.25	3.44E+15	3.85E+15	2.83E+15	3.91E+15	5.40E+15	4.09E+15	2.67E+15	4.11E+15	3.48E+15	3.08E+15	3.52E+15	3.00E+15
Ea_trim_r	+6	9.61E+01	9.38E+01	9.39E+01	6.83E+01	8.11E+01	7.53E+01	7.41E+01	7.49E+01	9.12E+01	8.08E+01	7.54E+01	8.70E+01
A_tet_f	*10	6.86E+03	2.30E+04	1.63E+04	1.31E+04	2.05E+04	2.15E+04	7.63E+03	2.67E+04	1.00E+04	1.87E+04	1.73E+04	7.39E+03
A_tet_r	*0.25	5.38E+15	2.41E+15	3.02E+15	3.50E+15	2.60E+15	2.51E+15	5.01E+15	2.17E+15	4.17E+15	2.76E+15	2.91E+15	5.12E+15
Ea_tet_r	+6	8.44E+01	8.20E+01	7.44E+01	8.01E+01	8.77E+01	7.31E+01	8.95E+01	7.40E+01	8.33E+01	7.56E+01	7.92E+01	6.72E+01
A_pent_r	*10	1.93E+17	4.72E+17	2.11E+17	1.47E+17	3.17E+17	2.20E+17	1.88E+17	2.57E+17	1.96E+17	4.30E+17	7.34E+16	4.21E+17